THE AQUEOUS ALTERATION OF CARBON-BEARING PHASES IN CR
CARBONACEOUS CHONDRITES

A DISSERTATION SUBMITTED TO THE GRADUATE DIVISION OF THE
UNIVERSITY OF HAWAIʻI AT MĀNOA IN PARTIAL FULFILLMENT OF THE
REQUIREMENTS FOR THE DEGREE OF

DOCTOR OF PHILOSOPHY

IN

GEOLOGY AND GEOPHYSICS

DECEMBER 2014

By

Patrick J. Gasda

Dissertation Committee:

G. Jeffrey Taylor, Chairperson
Eric Hellebrand
Gary Huss
Shiv Sharma
Michael Mottl

Acknowledgements

Abstract

By studying carbonaceous chondrites, we can understand the processes that occurred in the protoplanetary disk, constrain the conditions in the solar nebula, and determine the composition and evolution of organic chemicals that led up to the origin of life on Earth. The CR chondrites contain ~ 5 wt% carbon, mainly in the form of macromolecular carbon (MMC). There are examples of petrologic type 3 (primitive) and type 1 (extensively aqueously altered) CR chondrites, which makes the CRs particularly interesting for studying the stages of aqueous alteration. The MMC has been studied using in situ electron probe micro analysis (EPMA), Raman spectroscopy, and secondary ion mass spectrometry (SIMS). EPMA mapping of the carbon $K\alpha$ X-rays reveals that there are three types of carbon materials in these chondrites: high carbon phases (HCPs), matrix carbon (MC), and calcite. By Raman spectroscopy, we determine that the MC is MMC, but its spectra are unchanged by aqueous alteration. EPMA X-ray mapping suggests that the morphology of the HCPs and the spatial distribution of the MMC changes with extent of aqueous alteration. SIMS measurements have revealed that there is an isotopic difference between the HCPs and the MC in the GRO 95577 and QUE 99177 samples. HCPs have $\delta^{13}C \approx -25$ ‰ and $\delta^{15}N \approx 40$ ‰, and the MC have $\delta^{13}C \approx -35$ ‰ and $\delta^{15}N \approx 160$ ‰, relative to standard terrestrial isotope ratios. In order to produce the MC isotopic values, there must be a mix of the $+\delta^{15}N$ and $+\delta^{13}C$ soluble organic molecules and MMC (both present in the matrix). Therefore, the 'true' values for the MMC must be more enriched in ^{12}C and ^{15}N than the MC values. Results from the calcite measurements show that the production of calcite fractionates the carbon due to a combination of calcite crystallization and outgassing of CO_2 on the CR parent body.

Table of Contents

List of Tables

List of Figures

List of Symbols, Abbreviations, and Acronyms

Mathematical Symbols

δ: D-band Full Width at Half Maximum intensity in wavenumbers

$\delta^{13}C$:   the carbon-13 delta value is the $^{13}C/^{12}C$ ratio relative to the terrestrial Pee Dee Belemnite standard in permil

$\delta^{15}N$:   the nitrogen-15 delta value is the $^{15}N/^{14}N$ ratio relative to the terrestrial atmosphere standard in permil

γ: G-band Full Width at Half Maximum intensity in wavenumbers

σ_j: the uncertainties on the parameters, a_j

χ^2:   the statistical goodness-of-fit parameter

χ_0^2:   the minimum of χ^2

ω_D: D-band position in wavenumbers

ω_G: a Raman fit parameter related to G-band position by Equation 2.6

a_j: the optimum fitting parameters

$C\#$:   the number of carbon atoms in a molecule

F_L: the Lorentzian fitting function

F_{BWF}:   the Breit-Wigner-Fano (asymmetric Lorentzian) fitting function

$f(x_i)$:   a fitting function

I_1:   a Raman fit parameter related to the intensity of the D-band

I_2:   a Raman fit parameter related to the intensity of the G-band by Equation 2.5

I_D: the intensity of the D-band in arbitrary units

I_G: the intensity of the G-band in arbitrary units

N: the number of data points

P:	the number of model parameters
$P(a_j)$:	he total probability of making a set of measurements with the fitting function and a set of fit parameters
pH:	log hydrogen cation concentration in water
Q:	the Breit-Wigner-Fano function asymmetry factor
R_m:	the measured isotopic ratio used to calculate delta values
R_{std}:	the standard isotopic ratio used to calculate delta values
s_i:	standard deviation of the raw data points (y_i)
y_i:	raw data points

Ratios

H/C:	the ratio hydrogen to carbon in an organic molecule
I_D/I_G:	the D-band to G-band intensity ratio
N/C:	the ratio nitrogen to carbon in an organic molecule
O/C:	the ratio oxygen to carbon in an organic molecule
S/C:	the ratio sulfur to carbon in an organic molecule

Abbreviations

cal:	calcite
chond:	chondrule
D-band:	the Defect (or Dispersion) band, or peak, of the macromolecular carbon Raman spectrum
FeNi:	Iron-Nickel metal
G-band:	the Graphite band, or peak, of the macromolecular carbon Raman spectrum
G′-band:	a peak in the macromolecular carbon Raman spectrum related to the G-band

mag:	magnetite
Mg-silicates:	Magnesium-bearing silicate phases
ol:	olivine
plag:	plagioclase
pyx:	pyroxene
spl:	spinel

Acronyms

ANN:	Artificial Neural Network
a.u.:	Arbitrary Units
BSE:	Backscattered Electron
BWF:	Breit-Wigner-Fano
CAI:	Calcium Aluminum Inclusion
CI:	Ivuna-type carbonaceous chondrite group
CM:	Mighei-type carbonaceous chondrite group
CMA:	Calcite-Magnetite Assemblage
CO:	Ornans-type carbonaceous chondrite group
CPU:	Central Processing Unit
CR:	Renazzo-type carbonaceous chondrite group
CR1:	Petrologic type 1 CR chondrite
CR2:	Petrologic type 2 CR chondrite
CR3:	Petrologic type 3 CR chondrite
CVox:	oxidized Vigarano-type carbonaceous chondrite group

CVred: reduced Vigarano-type carbonaceous chondrite group

C-XANES: Carbon X-ray Absorption Near Edge Spectroscopy

DIC: Dissolved Organic Species

EET: Elephant Moraine

EH: High-iron Enstatite chondrite group

EL: Low-iron Enstatite chondrite group

FFAST: X-Ray Form Factor, Attenuation, and Scattering Tables

FWHM: Full Width at Half Maximum intensity

GRO: Grosvenor Mountains

HCP: High Carbon Phase

IDL: Interactive Data Language

IDP: Interplanetary Dust Particles

IFP: French Institute of Petroleum

IMF: Instrumental Mass Fractionation

IOM: Insoluble Organic Carbon

ISM: Interstellar Medium

JSC: Johnson Space Center

MAC: Mass Attenuation (or Absorption) Coefficient

MC: Matrix Carbon

MMC: Macromolecular Carbon

NASA: National Aeronautics and Space Administration

Nd:YAG: Neodymium-doped Yttrium Aluminum Garnet laser

NMR: Nuclear Magnetic Resonance spectroscopy

NMNH: National Museum of Natural History

OC: Ordinary Chondrite group

PAH: Polycyclic Aromatic Hydrocarbon

PHA: Pulse Height Analysis

QUE: Queen Alexandra Range

RGB: Red Green Blue

ROI: Region of Interest

SG: Savitzky-Golay

SGSD: Savitzky-Golay Second Derivative fitting method

SIMS: Secondary Ion Mass Spectrometry

SOC: Soluble Organic Carbon

SWiMA: Small Window Moving Average background subtraction technique

UWC: University of Wisconsin Calcite standard

WDS: Wavelength Dispersive X-ray Spectroscopy

ZAF: Z (atomic) number, Absorption, and Fluorescence corrections

Units

‰:   permil or parts per thousand

μm: micrometers or microns

μW: microwatt

at%   atomic percent

cm^{-1}:   wavenumbers

Ga: 10^9 years ago

Gyr: 10^9 year duration

KeV: kilo electron volts

Ma: 10^6 years ago

mm: millimeter

ms: millisecond

Myr: 10^6 year duration

nA: nanoampere

nm: nanometer

ns: nanosecond

pA: picoampere

ppm: parts per million

s: second

vol%: volume percent

W: Watt

wt%: weight percent

yr: year

Chapter 1

Introduction

Carbonaceous chondrites are an important key to understanding the solar nebula. Chondrites contain samples from the earliest epoch of the Solar System and also presolar material (Krot et al., 2007; 2009). Chondrites are composed of products (e.g., chondrules) from different stages of protoplanetary disk evolution. By studying carbonaceous chondrites we can understand the processes that occurred in the protoplanetary disk, constrain conditions in the solar nebula (Desch et al., 2007; Connelly et al., 2012; Pan et al., 2012), and determine the composition and evolution of organic chemicals that led up to the origin of life on Earth (Glavin et al., 2011; Callahan et al., 2012; Elsila et al., 2012).

Carbonaceous chondrites are composed of a complex assemblage of materials that changed depending on the types of alteration that the meteorite parent body experienced.[1] Since small organic molecules are destroyed by the high temperatures of thermal metamorphism (500 to 900°C) and larger organic molecules are converted into more graphitic materials (e.g., Bonal, 2007), meteorites that experienced thermal metamorphism are not relevant to this study. We are concerned with the aqueously altered class of chondrites; they were altered before the Earth accreted, and the temperatures on their parent bodies remained low, so their organic chemicals are preserved (Brearley, 2006). Primitive meteorites are also of importance because they should be direct samples of the solar nebula, and their chemical composition serves as a baseline for all the chondrites in their class.

Chondrites contain up to ~ 5 wt% carbon (Sephton, 2002). Depending on the alteration history of the meteorite, the carbon can be in the form of organic molecules (primitive and aqueously altered), carbonates (extensively aqueously altered), and carbides (primitive) (Brearley, 2006; Floss and Standerman, 2009). The organics that found in meteorites are abiotic organic compounds.[2] Up to ~ 90 % of the carbon is in the form of macromolecular carbon

---

[1] Based on their chemical composition, chondrites are split into multiple groups (CI, CM, CR, CV, etc.), wherein each group is thought to have shared a single parent body. Each family is made of up meteorites that can be classed based on its petrologic type, which describes the degree and type of alteration it experienced. Petrologic type 3 meteorites experienced the least amount of alteration. For the purposes of this paper, type 3 meteorites will be referred to as 'pristine' or 'primitive.' Petrologic types > 3 indicate that the meteorite has undergone varying degrees of thermal metamorphism. Type 7 chondrites would be rocks completely equilibrated by thermal metamorphism. Petrologic types < 3 indicate meteorites that have undergone varying degrees of aqueous alteration, with type 1 indicating the most aqueously altered.

[2] Organic molecules are compounds that contain carbon bonded covalently to other carbon atoms, hydrogen atoms, and heteroatoms (N, O, S, P, and the halogens). Natural or biotic organic compounds are present in or derived from

(MMC) material, which is sometimes described as kerogen- or graphite-like (Sephton, 2002).[3] The MMC is composed of aromatic units cross-linked with aliphatic organic chemical groups that usually contain heteroatoms (N, O, P, and S) (Cody and Alexander, 2005; Remusat et al., 2005; Peeters et al., 2011; 2012a; 2012b). MMC is ubiquitous in carbonaceous chondrites, but its chemical composition can change depending on the conditions of alteration of the meteorite parent body (Busemann et al., 2007). Its initial starting composition is not fully understood, and there is no consensus as to how or where it formed (Kerrige, 1999).

Our goal is to better constrain the processes that dictate the abiotic evolution of organic molecules in the early Solar System. Specifically, we study the fate of organic molecules in chondrites that are thought to have undergone aqueous alteration in their parent bodies (Brearley, 2006). Water mobilizes organic molecules and serves as a medium in which molecules can react; water can also be a reactant or a product in organic chemical reactions. Primary (igneous) minerals are also converted into secondary (weathered or aqueously altered) minerals by reactions with water and the soluble ions contained in the fluid (Brearley, 2006). Understanding the interactions between mineral surfaces as they undergo aqueous alteration, the fluid altering them, and organic molecules may be the key to understanding the origin of life on Earth (Hazen and Sverjensky, 2010).

In principle, it should not be hard to study the origin of life in active aqueous systems on Earth. We only need to find rocks that are very old, or ones that can serve as early Earth analogs. Life is thought to have emerged on Earth any time from the formation of the earliest ocean or major subsurface water reservoirs (possibly as early as ~ 4.4 Ga) to the end of the bombardment stage (~ 3.9 Ga) (Wilde et al., 2001: Mojzsis et al., 2001; Wacey et al., 2011). So far, no one has found whole rocks older than ~ 4 Ga, and all of the rocks from > 2 Ga are very weathered and/or metamorphosed (Wilde et al., 2001). Plate tectonics has recycled all the earliest material with the exception of the zircons that are 4.2 to 4.4 Ga (Harrison, 2009).

---

life, and abiotic organic compounds are formed without life, such as a consequence of geologic processes. Biological organic compounds can be formed abiotically and vice versa.

[3] Note that MMC is separate from the oft reported insoluble organic material (IOM), which is the organic acid-insoluble residues left over from demineralization (e.g., Alexander et al., 2014). We study the MMC in situ, meaning that we measure all of the organics, and not just the acid-insoluble fraction.

Because it is nearly impossible to study the setting for the origin of life, we must identify analog systems. To identify an analog, one must also make assumptions about what the Early Earth's surface or subsurface was like, thereby introducing a bias. In addition, every place on Earth of astrobiological significance that has some water and temperatures below ~ 130 °C contains life (Rothschild and Mancinelli, 2001; Rampelotto, 2013). Life's organic processes and products completely dominate any signature of abiotic organic activity we are concerned about (e.g., amino acid production). On the other hand, carbonaceous chondrites contain assemblages of primary and secondary minerals that are essentially undisturbed since the active phase of alteration ended. It is thought that the parent bodies of many meteorites have undergone aqueous alteration in the 0 to 300°C range (Brearley, 2006). They also contain a vast variety of organic compounds (Schmitt and Kopplin, 2010), including amino acids (Glavin et al., 2011) and nucleobases (Callahan et al., 2012), the building blocks of life. Therefore, these rocks can be plausible analogs for the early Earth aqueous alteration processes involving abiotic organic chemical synthesis.

The fate of organic molecules depends heavily on the composition and properties of the fluids that are interacting with them, such as pH, ion concentration, substrate surface chemistry, redox potential, etc. Although the major types of secondary minerals are similar among the aqueously altered meteorites CI, CM, and CR, it is known that the different meteorite groups underwent slightly different styles of aqueous alteration with different fluid composition, temperature, and pressure (Brearley, 2006). Small differences in fluid composition can introduce large differences in the organic chemistry; hence the meteorite groups likely produced different organic molecule mixtures. Also, the initial composition of the organic molecules in the parent body is needed before we can model the effects of aqueous alteration accurately. Thus, to fully understand how or even if aqueous alteration affects the MMC, we need samples of primitive chondrites that contain organic molecules and the MMC that accreted from the solar nebula and samples of aqueously altered meteorites that are in the same class. This study focuses on CR carbonaceous chondrites because samples of CRs types 3–1 exist and are suitable for this type of study (Weisberg and Prinz, 2000; Perronnet and Zolensky, 2006; Weisberg and Huber, 2007; Abreu, 2007; Abreu and Brearley, 2010).

CR carbonaceous chondrites had a parent body with a higher amount of metals and sulfides and have a smaller matrix to chondrule abundance ratio than most other carbonaceous chondrites. Chondrules in CR chondrites are mainly olivine and pyroxene; plagioclase is rare. CAIs have a low abundance in CR chondrites (Weisberg et al., 1993; 1995). Alteration of the CR parent body was almost exclusively low temperature (<50 °C) aqueous alteration (Jilly, et al., 2014). There are few examples of higher temperature alteration (Abreu, 2012; Bonal et al., 2013).

Antarctic CR chondrites were specifically chosen for this study. First, CRs were chosen because we can obtain samples of each stage of aqueous alteration in the CR meteorite class. Second, three particular meteorites were chosen because they are either the only representative meteorite of its petrologic type, and because their organics have been studied previously by other authors (e.g., Glavin et al., 2011). Third, weathering and contamination are minimal; the frozen Antarctic desert provides the best possible setting to preserve the organic materials we wish to study. Lastly, the procedure for collection and curation of Antarctic meteorites by NASA and the Smithsonian Institution also helps preserve the organic molecules; whereas meteorite falls for the CR chondrites (notably, Renazzo and Al Rias meteorites, both of which occurred in the late 1800s) were not necessarily collected or curated in the best possible manner for preserving the organic matter.

We hypothesize that the MMC has been affected by aqueous alteration on the CR parent body. The reasons for this hypothesis are, first, aqueous alteration produces unique assemblages of small soluble organic molecules, and these reaction products are highly sensitive to the conditions on the parent body and the content of the alteration fluids. Second, if the MMC contains sufficient amounts of defects or reactive sites, then it is possible that the MMC acted as a reactive substrate for the water soluble molecules, a source of reactive carbon molecules for the alteration fluid, a sink for the reactive carbon molecules, a product of the alteration process, or some combination of the above. If fluid alteration was active for a long time and occurred under oxidizing conditions, the MMC could have broken into smaller pieces, possibly through radical oxidation, and even mobilized in solution. Once in solution, we expect that the MMC would be vulnerable to reaction with other chemical species present in the alteration fluids. Hence, to prove or disprove this hypothesis, we will be looking for any correlations between the extent of

aqueous alteration and the chemical structure of the MMC determined by Raman spectroscopy (Chapter 2), the elemental composition of the matrix by electron microprobe analysis (Chapter 3), and the carbon and nitrogen isotopic composition of the matrix (Chapter 4).

1.1 Raman Fitting Techniques

The interpretations in Chapter 3 rely heavily on the proper analysis of the Raman spectrum of MMC. As a consequence of collecting MMC Raman spectra in situ, there is significant and variable fluorescence (an intense and broad Raman feature that dominates the MMC Raman signal), which makes the data analysis difficult. Moreover, tens of thousands of spectra were collected and an automated analysis process was needed to reduce the data. The summary of the developed procedure is Chapter 2, but here I briefly summarize the initial problems that motivated me to develop a new procedure.

The Raman spectrum fitting procedure used in this study is based on the fitting procedures extensively used in the literature to describe MMC and graphite-like materials (Ferrari and Robertson, 2000; Bonal et al., 2006, Busemann et al., 2007). Essentially, the D-band is fit using a Lorentz line shape, and the G-band is fitted using a skewed Lorentz line shape called Breit-Wigner-Fano (BWF) function (see Chapter 2 for more detail), though any line shape can be used, in principle. At first, I considered using the IDL (Interactive Data Language) function 'amoeba' (a downhill simplex routine that can minimize a multi-dimensional function) to minimize the chi-squared statistic, χ^2, in the following manner:

$$\chi^2 = \Sigma \left(\frac{1}{\sigma_i^2}\right) \left(data_i - (profile1 + profile2 + baseline)\right)^2 \qquad (1.1)$$

where profile1 and profile2 represent the Lorentz and BWF functions, respectively. The baseline represents the function for the baseline (a line, polynomial, or any other function), and $data_i$ is the raw data with σ_i uncertainties on each data point. This is similar to the procedure used by Busemann et al. (2007) wherein baseline is fit simultaneously with the peaks. Other workers (e.g., Bonal et al., 2006) fit the background separately and subtract it before the peaks are fit with the profiles. Chapter 2 shows how different background subtraction techniques are inherently flawed because they cannot fully take background shape into account, and errors in background fitting propagate into errors in the Raman fits. The new procedure uses a second-derivative

6

technique that does not require subtraction of a baseline, which is far more robust than procedures that fit or subtract the background fluorescence.

The fit is weighted by the uncertainty in the data, σ_i, which we originally assumed is the Poisson noise of the signal: the square root of the CCD counts after the background is subtracted from the spectrum. All of the spectra we analyzed using this method had reduced chi-squared values << 1 or >> 1. Reduced chi-squared is defined as the chi-squared divided by the number of degrees of freedom in the model. Since it is not likely that the degrees of freedom value is incorrect, reduced chi-squared values not ~1 suggests that σ_i is too large (in the case of reduced χ^2 << 1) or too small (in the case of χ^2 >> 1). This problem might stem from an unknown effect that fluorescence has on σ_i.

The real issue with the fluorescence background is our poor understanding of its source in our samples. The source is an unknown organic chemical compound or mix of chemical compounds that varies from spectrum to spectrum. This suggests that the background is a superposition of multiple peaks. A full understanding of the fluorescence phenomena in meteorite samples is likely impossible because the nature of the source is unknown and variable. If we do not understand the fluorescence, it is extremely difficult to understand how background subtraction propagates uncertainty into σ_i. Certainly, the weights on the fit function are not all the same (e.g., $\sigma_i = 1$), nor are they the square root of the total counts, because neither of these methods has produced reasonable parameter uncertainties. In Chapter 2, we implement a Monte Carlo routine to estimate errors, which avoids using χ^2 to determine parameter uncertainties and goodness-of-fit. Thus, we do not need to know σ_i to fit the spectra.

Chapter 2

Modeling the Raman Spectrum of Graphitic Material in Rock Samples with Fluorescence
Backgrounds: Accuracy of Fitting and Uncertainty Estimation

2.1 Abstract

We propose a robust technique called Savitzky-Golay Second Derivative (SGSD) fitting for modeling the in situ Raman spectrum of graphitic materials in rock samples such as carbonaceous chondrite meteorites. In contrast to non-derivative techniques, with assumed locally linear or nth-order polynomial fluorescence backgrounds, SGSD produces consistently good fits of spectra with variable background fluorescence of any slowly varying form, without fitting or subtracting the background. In combination with a Monte Carlo technique, SGSD calculates Raman parameters (such as peak width and intensity) with robust uncertainties. To explain why SGSD fitting is more accurate, we compare how different background subtraction techniques model the background fluorescence with the wide and overlapping peaks present in a real Raman spectrum of carbonaceous material. Then utility of SGSD is demonstrated with a set of real and simulated data compared to commonly used linear background techniques. Researchers may find the SGSD technique useful if their spectra contain intense background interference with unknown functional form or wide overlapping peaks, and when the uncertainty of the spectral data is not well understood.

2.2 Introduction

A variety of geologic samples, such as metamorphic rocks and carbonaceous chondrite meteorites contain graphitic materials, known specifically in the meteorite literature as Insoluble Organic Material (IOM) or macromolecular carbon (MMC), in concentrations up to ~ 5 wt%. It is useful to study these graphitic materials because their chemical structure can be linked to the host rocks' thermal and metamorphic history (Bonal et al., 2006; 2007; Quirico et al., 2003). It is convenient to study the MMC using Raman spectroscopy because the correlation of Raman spectral parameters to known physical changes in the graphite (Tuinstra and Koenig, 1970; Wopenka and Pasteris, 1993; Ferrari and Robertson, 2000) and graphene structure (Lucchese et al., 2010; Cançado et al., 2011) has been previously established. However, the MMC is kerogen-like; it is not equivalent to graphite, and it contains a variety of organic chemical groups in its structure that include the Raman-active structure that is spectrally similar to graphite (Sephton,

9

2002). Since these organic groups, and the other organic chemicals in the host rock, cannot be effectively removed from the Raman-active graphite-like portion of the sample without altering the chemical structure of the graphitic part of the MMC or losing the context petrography, the in situ Raman spectra of these samples tend to contain intense fluorescence backgrounds. Additionally, the majority of the previous studies use a model that fit the Raman spectral peaks of graphite (Ferrari and Robertson, 2000). Fitting a Raman spectrum with a model gives us important spectral parameters—peak full width at half maximum, peak position, and peak intensity—which have been correlated with chemical structure information, e.g., maturation grade or metamorphic grade of the host rock (Tuinstra and Koenig, 1970; Wopenka and Pasteris, 1993, Quirico et al., 2003; 2009), thermal history of the host rock (Beyssac et al., 2002; 2004), aqueous history of the host rock (Busemann et al., 2007), and disorder or defect density (Lucchese et al., 2010; Cançado et al., 2011).

Generally, spectra seen in in situ studies of MMC of the aqueously altered meteorites have interference from steep and variable fluorescence backgrounds. Our lab has taken tens of thousands of spectra of rock samples and much of it is plagued by intense fluorescence backgrounds. We suspect that other labs that use the same commercial equipment experience the same problems. When an intense fluorescence background is present, it is difficult to glean useful data from the spectrum, especially when the fluorescence intensity is on the order of the intensity of the peaks or greater. The Raman bands that are most important to our work lie in the 1250 to 1650 cm^{-1} region of the Raman spectrum, exactly where the fluorescence background starts to dominate the signal while using a 532 nm laser. The fluorescence background also completely dominates the second-order peaks in the MMC spectrum at around 2800–3200 cm^{-1}. Since the source of the fluorescence is an unknown, a full understanding of the fluorescence phenomena in meteorite samples may be impossible. And, while it is possible to cut down on the amount of fluorescence in these spectra by employing a confocal Raman microscope and laser bleaching methods as we and others have done, significant fluorescence is still seen in spectra. Hence, a post-processing method for removing the background, either manually or computationally, from the raw spectra is usually used.

The background fluorescence in a small spectral window containing the relevant peaks is typically subtracted from the spectrum. Backgrounds can be fit using a first-, second-, third-

10

order polynomial, or a cubic spline. This approach allows for the fitting (outside the spectral region of interest) and subtraction of the background before the peaks are fit (Bonal et al., 2006; 2007; Quirico et al., 2003; 2009; Rotundi et al., 2008; Fries et al, 2009; Gasda and Taylor, 2013; Sforna et al., 2014). Another method fits a linear background and the peaks simultaneously (Busemann et al., 2007). In some studies, spectra with rather intense or variable fluorescence baselines are completely discarded because they cannot be fit with traditional background subtraction techniques (e.g., Starkey et al., 2013), potentially biasing the data set. Each of these methods makes an assumption about the functional form of the background that we wish to avoid because the background fluorescence, in general, does not follow a simple functional form.

There are state-of-the-art techniques discussed by Schulze et al. (2005) that do not fit the background with an assumed function and could be optimized for the problem at hand. There are a number of techniques in Schulze et al. (2005) that subtract the background from overlapping peaks (known as 'congested' peaks in the paper) quite well. Those techniques include the moving average background subtraction technique (Schulze et al., 2005; 2012), which is similar to the median background subtraction technique, and we explain in the Background Subtraction Techniques Section why both are not suitable for our data sets. The other technique from Schulze et al. that could be suitable is the artificial neural networks (ANNs) method (Schulze et al., 2005). But, by the authors own admission "it is not currently known whether a single network could be trained to perform baseline estimation on spectra with varying shapes of baseline." So, although ANNs appear to perform very well, ANNs may be simply too complex to implement for our spectra especially with fluorescence backgrounds with variable shapes.

The purpose of this work is to propose a solution to the problem of fluorescence that has a slowly-varying dependence with wavenumber, rather than correcting for a first- or weak second-order background, by applying a different fitting technique. If a robust fitting method could be developed to fit the spectral bands of interest, then it could be very useful for us and other researchers in our field. We propose to use a more robust technique, Savitzky-Golay Second Derivative (SGSD) fitting, that allows for the suppression, but not subtraction, of a general background fluorescence (of unknown functional form, but slowly varying with respect to the relevant peaks) to accurately model the Raman parameters of the sample. Additionally, our SGSD fitting procedure can be used to calculate robust uncertainties on the model parameters.

We explain the differences in the results of the SGSD technique compared with a linear background subtraction technique, henceforth called the 'standard' technique. To accomplish this, we use simulated data superimposed onto a series of different background types, and also a set of real spectra. Though different researchers may employ different fitting techniques to account for a linear background, the linearity assumption is the critical aspect we are testing in this paper. It becomes clearer in the Simulations of Real Spectra section of the Results and Discussion section that the standard method is the only other suitable method to compare to our new method.

2.2.1 Goodness of Fit and Uncertainty Estimation

In any study requiring a mathematical model (an equation that fits data points with uncertainties), it is important to determine the goodness of fit of the raw data and estimate the uncertainty values of the modeled spectrum parameters. Proper uncertainty estimation is vitally important for understanding the chemical nature of the MMC in a bulk sample. If model parameter uncertainties are over- or underestimated, it may cause misinterpretation of the results. For example, underestimated uncertainties could lead one to interpret that the MMC is chemically heterogeneous in a host rock when it is not, and vice versa. Therefore, it is important to determine the correct uncertainty for every model parameter.

Under the assumption that our data points y_i, with standard deviations s_i, are Gaussian distributed about the model, we can write the total probability of making our set of measurements with our fitting function $f(x_i)$ with parameters a_j: (Eq. 8.3 from Bevington and Robinson, 1992):

$$P(a_i) = \prod \left[\frac{1}{s_i\sqrt{2\pi}} \right] e^{\left(-\frac{1}{2}\Sigma \left[\frac{y_i - f(x_i)}{s_i} \right]^2 \right)}$$

(2.1)

The well-known goodness-of-fit parameter chi-squared (Eq. 2.2) is optimized by minimizing (Eq. 8.4 from Bevington and Robinson, 1992):

$$\chi^2 = \Sigma \left[\frac{1}{s_i^2} (y_i - f(x_i))^2 \right]$$

(2.2)

The optimum parameter values, a_j, are the set of values which minimize χ^2. The reduced χ^2 value is the minimum of χ^2 divided by the degrees of freedom (the number of data points, N, minus the

number of model parameters, P). The reduced χ^2 value should be approximately equal to one. Minimization of χ^2 is typically done with a computational algorithm. The uncertainties of the fit parameters, σ_j, are typically determined computationally by varying aj until the minimum of χ^2 varies by one (i.e., $\chi_0^2 \rightarrow \chi_0^2 + 1$).

It is critical to have a good estimate of the s_i data uncertainties in order to determine good estimates of the a_j values. If the s_i data uncertainties are too small, χ_0^2 values will be much larger than the degrees of freedom, resulting in underestimated parameter uncertainties σ_j. On the other hand, if the s_i data uncertainties are too large, then χ_0^2 will be much smaller than the number of degrees of freedom, and the inferred σ_j parameter uncertainties become too large. In early experiments with our own in situ Raman spectra of carbonaceous meteorite samples, most χ_0^2 values were much greater than the number of degrees of freedom (Gasda and Taylor, 2013; Gasda et al., 2012; 2013). Initially, we hypothesized that the problem stemmed from our assumption that the s_i data uncertainties were dominated by Poisson noise. Poisson distributed noise should represent the minimum uncertainty on each data point, but we found that the noise in our data is somehow related to the fluorescence background. Further investigation prompted us develop the new approach presented in this paper because we could not determine how the fluorescence background present in every spectra propagated into the s_i data uncertainties (Gasda et al., 2013).

We have determined that we cannot use a χ^2 minimization routine, so in order to calculate reasonable uncertainty values for each parameter value, we must employ a Bootstrapping method (Chernik, 1999). Bootstrapping is ideal for any spectroscopic analysis because it is the most general and robust method for determining σ_j without a need to calculate χ_0^2. We avoid the inherent requirements of χ^2 minimization: fully understanding s_i and data that is Gaussian distributed about our model (Andrae et al., 2010). Additionally, error estimation using a resampling technique (see Methodology for further explanation) is both easy to implement with the bootstrapping method and a very intuitive approach (Andrae, 2010).
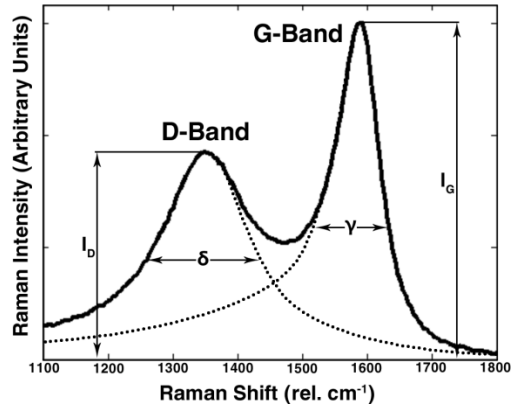
Figure 2.1: The idealized Raman spectrum of MMC. The D- and G-bands are labeled with band widths (δ and γ) and intensities (I_D and I_G).

2.2.2 The Raman Spectrum of Graphitic Materials

Raman spectroscopy measures shifts in photon energy that occur when a sample scatters light from an incident laser source. The incident laser excites an electron from the valence band to the conduction band. The electron can either emit a phonon (Stokes process), absorb a phonon (Anti-Stokes process), or neither emit or absorb a phonon (Rayleigh or elastic process), and relax back to the valence band emitting the photon that the Raman instrument measures (Dresselhaus et al., 2005). The MMC Raman spectrum is characterized by two bands (Figure 2.1), the D-band (~ 1350 cm^{-1}) and the G-band (~ 1600 cm^{-1}). The G-band is first order (single-phonon) Raman scattering mode for graphite. The D-band is a combination of two second-order Raman scattering modes (a one phonon, one elastic mode and a two-phonon mode) and it requires a defect in the MMC structure or an edge (Cançado et al., 2002).

Because the D-band arises from defects in the Raman-active graphite-like portion of the MMC structure (an extended network of aromatic carbon rings), the accurate measurement of D- to G-band intensity ratio (I_D/I_G) and G-band full width at half maximum (γ) is necessary to understand the chemical structure of the MMC (Cançado et al., 2011). In defect free graphite, only the G-band is present and γ is at its most narrow. As defect density increases, the I_D/I_G increases up to a maximum and γ increases. This is akin to Stage 1 of the three stage amorphitization trajectory of the Ferrari and Robertson (2000) model where I_D/I_G is proportional to the inverse of the 'crystallinity' of the graphite. As Cançado et al. (2011) explain, the

14

maximum I_D/I_G is the point where defects have saturated the graphite structure. Beyond this point, the defects are close enough together to begin to coalesce; the number of six-membered rings begins to decrease (i.e., the density of the structure that is responsible for the D-band decreases). Thus, I_D/I_G decreases proportionally to hexagon density (Stage 2 of the Ferrari and Robertson [2000] model). Cançado et al. (2011) show that γ always increases with increasing defect density. So, the relationship between the Raman spectrum and the defects within the graphitic part of the MMC chemical structure can be well described by measuring I_D/I_G and γ.

The Raman spectrum fitting function used in our work (Gasda and Taylor, 2013; Gasda et al., 2012; 2013) is based on the fitting procedures in use extensively in the literature to describe graphite-like materials (Bonal et al., 2006; Ferrari and Robertson, 2000). These models fit the D band using a Lorentz line shape (Eq. 2.3), and fit the G-band using an asymmetric Lorentz line shape called the Breit-Wigner-Fano (BWF) (Eq. 2.4) function.

$$F_L = I_1 \frac{\delta/2\pi}{(x-\omega_D)^2 + (\delta/2)^2} \tag{2.3}$$

$$F_{BWF} = I_2 \frac{[1+2(x-\omega_G)/Q\gamma]^2}{1+(2(x-\omega_G)/\gamma)^2} \tag{2.4}$$

The variables of F_L and F_{BWF} correspond to the spectral parameters of the D- and G-bands. The variables I_1 and I_2 are related to the intensity, ω_D and ω_G are the peak positions (cm^{-1}), and δ and γ are the full width at half maximum (FWHM) (cm^{-1}) of the D- & G-bands, respectively. Q is the asymmetry factor of the G-band. The G-band asymmetry arises from the coupling of the G-band mode with the continuum. Other workers (Busmann et al., 2007) use only the Lorentzian line shape for both the D and G bands. It has been shown (Busmann et al., 2007) that there are systematic variations between the resulting fit parameters when using different fit models, but the general trends shown with either model are essentially the same. We chose a BWF profile for our model because it is more general; when asymmetry of the line shape is low, Q goes to infinity and the general form of Eq. 2.4 reduces to the general form of Eq. 2.3.

Note that when using the BWF line shape, G-band intensity and position are calculated in the following manner:

$$I_G = I_2 \left(1 + \frac{1}{Q^2}\right) \tag{2.5}$$

15

$$\text{G-band Position} = \omega_G + \frac{\gamma}{2Q} \tag{2.6}$$

Since the asymmetry factor Q influences both G-band position and intensity, it is important for any model that uses the BWF line shape to accurately calculate Q especially when Q is small (a highly asymmetric G-band).

Cançado et al. (2011) state that the D-band should be fit with two Lorentzian profiles to account for the two separate phonon processes that occur with the D-band. However, they state that the two peaks are best constrained by the position of the G′-band in the Stokes and anti-Stokes spectrum (Cançado et al., 2002). Since our experimental setup cannot measure the anti-Stokes spectrum, we chose to fit the D-band with only one Lorentzian profile to lower the number of unconstrained free parameters in our model. In addition, the difference between the two D-band positions is smaller than the average one standard deviation uncertainty of the measured position of the D-band. So we are unlikely to be able to resolve the two peaks.

2.3 Methodology

2.3.1 Second Derivative Fit to Remove Background Fluorescence

Rather than fitting a function to the background, we propose Savitzky-Golay Second Derivative (SGSD) fitting. SGSD removes the effect of any smoothly varying background fluorescence component from the Raman spectrum fits by taking the second-derivative of the spectrum. Second derivative spectra are fitted using the second-derivative of Eq. 2.3 and Eq. 2.4 by constrained least-squared minimization. It is necessary to smooth the noisy Raman spectrum, in this case, between 956 and 1840 cm^{-1}, before calculating the second-derivative, by applying a second-order Savitzky-Golay (SG) smoothing function (Zhang and Ben-Amotz, 2000). If the raw spectrum is smoothed too much, then spectral information is lost. But if smoothed too little, the second-derivative spectrum becomes too noisy and it is not easily fit computationally. We found that a window size of 27 retains the important Raman spectral structure without smoothing the data too much, while greatly reducing the noise in the derivative spectra (Holler et al., 1989).

The non-text Supplementary Materials of this dissertation includes a copy of the source Matlab (The Mathworks, Natick, MA) code that produces and fits the simulated data with the SGSD method using the reader's own data. The reader can compare the results with the linear background subtraction and the floating background method (also supplied in the non-text Supplementary Materials). All methods use the same fit numerical minimization routine as described later in this section in order to determine the best fit model parameters (the variables in Eq. 2.3 and Eq. 2.4) and estimate the uncertainties.

2.3.2 Monte Carlo Uncertainty Estimation

To ascertain the precision of our measurements, it is necessary to determine the uncertainties of the spectral parameters (e.g., peak position, peak width) given in Eq. 2.3 and Eq. 2.4. A resampling technique based on a Monte Carlo bootstrap method is used (Chernik, 1999). The algorithm generates an array of empirical uncertainties (s_i) by computing the distance between each measured data point and the SG smoothed spectrum. From this array, we randomly draw values (allowing repeats) that we add to the original smoothed spectrum. Using this new simulated data spectrum, we recalculate our second-derivative fit parameters as described above. For example, repeating this process 10^3 times yields 10^3 values for each parameter in Eqs. 2.3–2.6. The one sigma uncertainty of the fit parameters is simply the standard deviation of these 10^3 values for each parameter (there is no error propagation necessary for parameters calculated from Eq. 2.5 and Eq. 2.6).

2.3.3 Explanation of the MATLAB code

We have developed a new method to model Raman data of MMC in Matlab (R2012a). The Matlab code is available in the Supplementary Material for use with the reader's own data. The code fits the second-derivative of the Savitzky-Golay smoothed Raman spectra with the second-derivative of Eq. 2.3 and Eq. 2.4. The program performs a specified number of Monte Carlo runs to estimate the uncertainty and the most likely value of the fit parameters. The starting parameters for I_1, I_2, and δ are calculated by estimating the area of each peak by integration with a lower bound of zero and an upper bound defined by ten times the initial guess of the peak height or width. The starting band positions, with bounds in parentheses, are 1360 cm^{-1}

17

(1320, 1380) and 1580 cm^{-1} (1530, 1620) for the D and G bands, Q = −5 (−50, 0), and γ = 100 cm^{-1} (0, 500), and can be changed to suit the user's spectra. Matlab's constrained nonlinear optimization routine 'fmincon' is then used to optimize the fit using a least-squared method and the bounds defined around the initial guesses of the parameters. Fmincon optimizes the model parameters using the interior-point algorithm with a supplied analytical Hessian matrix and gradient vector in the SG smoothed spectrum. The Monte Carlo routine then generates a new spectrum as described in the previous section. Each Monte Carlo run uses the same starting parameters as the initial fit. A typical spectrum with 10^3 Monte Carlo runs takes ~ 60–500 s depending on the spectral signal to noise.

      The SGSD technique is compared to two other fitting techniques later in the Simulations of Real Spectra section: linear background subtraction (the standard method) and floating linear background (the 'line float' method). These two techniques are used to fit the same spectra, supplied with the same starting parameters and using the fmincon optimization routine in Matlab and our Monte Carlo routine to estimate uncertainties. Both of these techniques use the regular (non-derivative) versions of Eq. 2.3 and Eq.2.4 to fit the D- and G-bands. The linear background subtraction method subtracts a line from the background by fitting a line to two ranges of points sufficiently outside the D- and G-bands (675–900 cm^{-1} and 1800–2025 cm^{-1}) so that they do not overlap the tails of the peaks in most spectra. The same fitting technique is used for the other background subtraction methods, except the floating line method. The floating linear background technique includes the equation for a line with Eq. 2.3 and Eq. 2.4, so that the slope and y-intercept become free parameters during the peak fitting process. The slope and y-intercept are initially guessed by using the same line from the linear background subtraction method. All fitting methods tested for this paper use the same Monte Carlo uncertainty estimation technique as the one used for the SGSD method.

2.3.4 Raman Spectroscopic Experiments

      All Raman experiments were performed using a WITec Raman alpha300 R confocal microscope instrument. Single Raman spots were collected for 2 hours, with a frequency-doubled solid-state Nd:YAG (neodymium-doped yttrium aluminum garnet) 532 nm laser at ≤ 50 μW power and a ~ 10 μm laser spot size (20x objective), or a power density of ~ 64 W/cm^2.

Low laser power was achieved using a series of neutral density filters to prevent sample alteration by the laser. All Raman spectra were standardized using a pure Si-wafer with a true Raman line at 521 cm^{-1}.

The Antarctic meteorite samples for the Raman experiments are three specially prepared chips of Renazzo-type (CR) chondrites provided by the Johnson Space Center (JSC) Meteorite Curation Laboratory: Queen Alexandra Range (QUE) 99177 (CR3, least altered by water) (Abreu, 2007), Elephant Moraine (EET) 92161 (CR2, some water alteration) (Abreu and Brearley, 2004), and Grosvenor Mountains (GRO) 95577 (CR1, extensively altered by water) (Perronnet and Zolensky, 2006). The CR chondrites are a group of primitive meteorites (Kallemeyn et al., 1994), that contain a vast variety of organic carbon compounds ranging in size from large (Cody and Alexander, 2005; Pearson et al., 2006) to small, including amino acids (Glavin et al., 2010) and nucleobases (Callahan et al., 2011). The CR chondrite group contains meteorites that are some of the most pristine rock samples of the early Solar System and some that are extensively altered by water (Krot et al., 2002); thus, understanding their components is important for understanding the origins of graphitic materials in meteorites and the behavior of the MMC during aqueous alteration (Kerridge, 1999). The CR chondrite samples obtained from JSC are chips obtained from the center of the meteorite. The samples have not been impregnated with epoxy, nor were the meteorites cut with oil or water. One side of the CR2 and CR1 meteorite chips were polished with fine diamonds and washed once with 95 % ethanol. Raman measurements were performed on both polished and unpolished sides of the samples.

2.4 Background Subtraction Techniques

Background subtraction techniques can be broadly separated into two categories: background fitting techniques that assume a functional form for the background and those that do not assume a particular functional form. Figure 2.2 shows how each of three common background subtraction techniques (first- through third-order polynomial backgrounds), the floating line technique, and the new SWiMA algorithm performed on an example spectrum from the meteorite EET 92161. Figure 2.2 plots four background fitting techniques with 50 percentile error ranges (dotted red lines) for an example spectrum, the (A) 'standard' linear subtraction, (B)

floating line fitting technique with accompanying fit in Figure 2.2C, (D) second-order polynomial fit, and (E) a third-order polynomial fit with accompanying fit in Figure 2.2F. Figure 2.2G and 2.2H show examples of the SWiMA background subtraction technique with different moving average window sizes. The fit for three of the techniques is shown in the right-hand column of Figure 2.2 along with the calculated Raman spectral parameters and 2σ uncertainties. The fit of this spectrum using the standard technique and SGSD is shown in Figure 2.3D and 2.3F, respectively. The calculated Raman spectral parameters in 1σ uncertainties are provided in Table 2.1.

2.4.1 Background Fitting with an Assumed Function

Although the slope of the background in this example spectrum is nearly the same as the slope of the left side of the D-band peak, the part of the spectrum between ~ 1000 cm^{-1} and ~ 1200 cm^{-1} appears to be a part of the background. A small kink in spectral shape at ~ 1200 cm^{-1} is where the tail of the D-band begins. As a consequence, all of the background fitting techniques tend to overestimate the peak areas. In the first case, Figure 2.2A the linear background fit, is generally a poor fit because the slope of the background on the left and the right of the D- and G-bands is different; a line cannot be fit to this background.

The 'floating line' fitting technique accuracy and precision is generally worse than the standard line subtraction technique, in this case. The fitted peaks (Figure 2.2C) appear fine, but the resulting D-band width and intensity ratio is too large. The uncertainties are larger than the standard linear background subtraction due to the two additional free parameters for the linear background. The linear background can be degenerate with the G-band asymmetry factor Q, resulting in poor stability of the fitting routine (especially when the background slope and intercept are constrained), and poor precision of the fit parameters. This difference between the two techniques is further described in the Simulations of Real Spectra section.

The two polynomial background subtraction techniques (Figure 2.2D, second-order, and Figure 2.2E, third-order) are very similar to each other. In both cases, the background is fit using the same method as the linear fit, but with higher order functions. The third-order polynomial is only incrementally better than the second-order polynomial, although it still gives the D-band a longer tail. The third-order polynomial has a wider D-band than the second-order fit (the second-

20

order fit is higher than the third-order fit on the low wavenumber side of the peaks), but the third-order fit estimates a smaller total peak area compared with the second-order polynomial. For this reason, we show the third-order polynomial background subtracted peak fit in Figure 2.2F. The fit is an improvement on the standard fit (Table 2.1) and the floating linear fit, but the D-band width is still too wide.

Background fitting techniques that were not considered include the cubic spline (or similar spline) background fits (Fries et al., 2009). Cubic splines are expected to perform worse than the other background subtraction techniques shown here since splines only use the few nearest points on either side of the peaks to fit the background beneath the peaks. Splines are therefore very sensitive to small variations in the background near the peaks and perform poorly in an unsupervised algorithm, or with variable or noisy fluorescence background.

There are two general problems with any background fitting technique when the background fluorescence is fit with a function (e.g., a polynomial). First, no matter what function is used to fit the background, the shape of the background beneath the peaks is an assumption. When performing unsupervised fitting of larger datasets, one must assume that the background functional form does not change. Second, the number of points used to define the background affects the fit. It is always better to choose more points from the background to constrain its shape, but this can be problematic in real Raman spectra that may have other peaks present near the D- and G-bands. Third, the background away from the fits can be fit extremely well (Figure 2.2E), but the important region, the background beneath the peaks, may diverge significantly from the background shape away from the peaks. In the case of spectra of carbonaceous materials, where the fluorescence tends to be present in the spectra where the carbonaceous peaks are present, we cannot take a background spectrum to understand how the background behaves when the peaks of interest are not present.

Finally, the peak areas depend on the range of points that are defined as the background. This is a major problem with spline or interpolation methods because only two points are used to guess the background beneath the peaks. Somehow (either manually or computationally), the background start and end points near the peaks have to be defined. This can be very hard to determine especially when the slope of the tail of the D-band is very similar to the background slope, as seen in Figure 2.2, because the same range of points needs to be used for the whole data

set to keep the results consistent with each other. Otherwise, this range of data points could become a variable in the data sets that affects the peak fit parameters. Other background fitting methods (e.g., a polynomial) are superior to a linear background, but selecting the range of points to use is largely subjective, and still requires the user to pick a range of points that are far away from the peak range but still provide a good estimate of the local shape of the background fluorescence. This can be especially difficult when the spectra are variable, or have variable backgrounds. Therefore, the subjective definition of the background range and background functional form is a limitation in using background fitting methods for large datasets with varied spectra. A fitting method that does not need to define the background range or assume a functional form would circumvent these issues.

The floating background fit methods overcomes the problem of defining a subjective range of points as the background. Instead, the entire spectrum is used to fit the background as the peaks are being fitted. However, this method produces new problems. The background fit adds new unconstrained variables which could cause the fitting process to become less robust or unstable. Additionally, the calculated Raman parameters may have larger uncertainties because of the two additional fitted variables.

2.4.2 Background Fitting without an Assumed Function

The automated moving-average background subtraction procedure was previously discussed in detail by Schulze et al. (2012). The automatic moving average procedure, SWiMA, uses a small window to apply a moving average to the background. The averaging window size increases iteratively until there is no more change in the estimated background area. Automatically increasing the averaging window size by the 'window increment' frees the user from having to guess a suitable window size for their spectra. This method is shown to be suitable for 'congested peaks' in Raman spectra (Schulze et al., 2005), but not suitable for very wide peaks. Wide peaks tend to not be recognized as peaks because the moving average window is very small compared to the peak widths. In some cases, the D- and G-bands are recognized by SWiMA, but the program confuses the interpeak valley as a part of the background. In other cases, most of the peaks are subtracted out with the background. This causes the peak areas and widths to be greatly underestimated, as illustrated in Figure 2.2G. The SWiMA background

subtraction can be improved by increasing the starting window size to something larger (e.g., 40), but peak areas are still underestimated slightly in Figure 2.2H when SWiMA subtracts too much of the interpeak area, and the resulting Raman parameters have lower reported band widths. Overall, although the SWiMA procedure does a superb job subtracting the background, the necessity of picking a suitable window size does not make this procedure ideal for the unsupervised analysis of large datasets (see Figure 2.4). Perhaps, when analyzing individual spectra, the SWiMA procedure, with a well-chosen window size and window increment, would be preferred over all the previous examples.

Another background subtraction technique, in the same vein as the SWiMA procedure, the median background subtraction method, was discussed in detail by Schulze et al. (2005). An automatic moving noise median method (NMM) that uses a small window to apply a median to the background is very similar to the moving average method. We do not show an example of it because we expect it to perform at least as well as SWiMA. The only difference between SWiMA and NMM is that it uses the median instead of the mean of the noise, so the data does not need to be smoothed beforehand.

All of the examples in Figure 2.2 show that there are problems with fitting the background and subtracting it from the peaks to produce a flat baseline. Either background is added to the peaks, increasing peak area, or peak area is lost during the subtraction. The change in the peak areas change the resulting Raman fit parameters. In all cases, the fitted curve matches the data points well, but each method produces a different answer with different precision. Clearly, we need a method that can fit the peaks without subtracting the background. We use the SGSD technique to solve this problem. Second derivative fitting eliminates our need to know or assume the function of the background because the background is not subtracted.
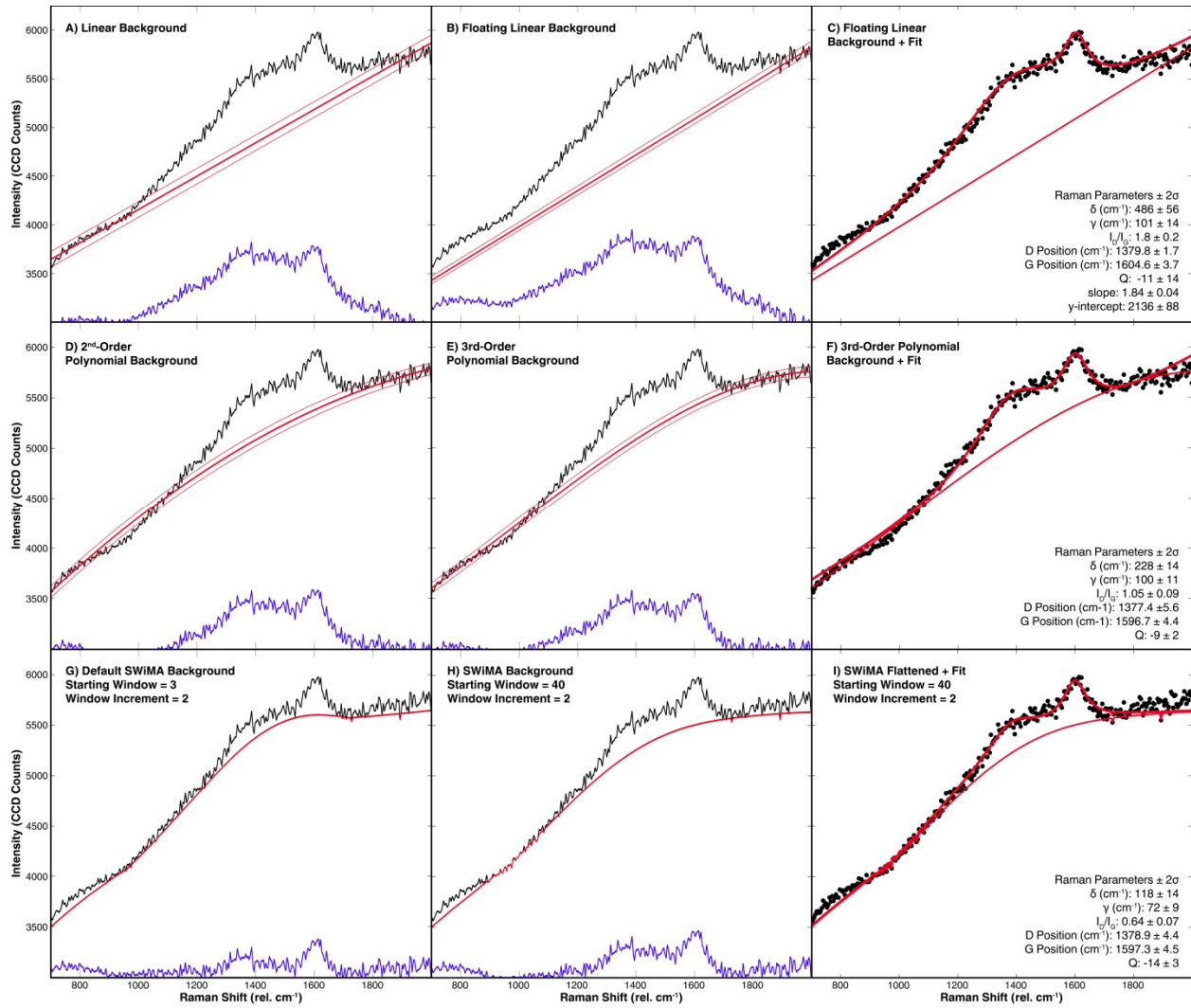
Figure 2.2: Various background subtraction techniques are tested with a spectrum from EET 92161 (CR2) chondrite. Raw data is shown in black and the background subtracted raw spectrum is shown in blue. Red curves represent fits of the background and of the data, and dotted red lines are the 50 percentile uncertainty ranges for the fitted backgrounds.
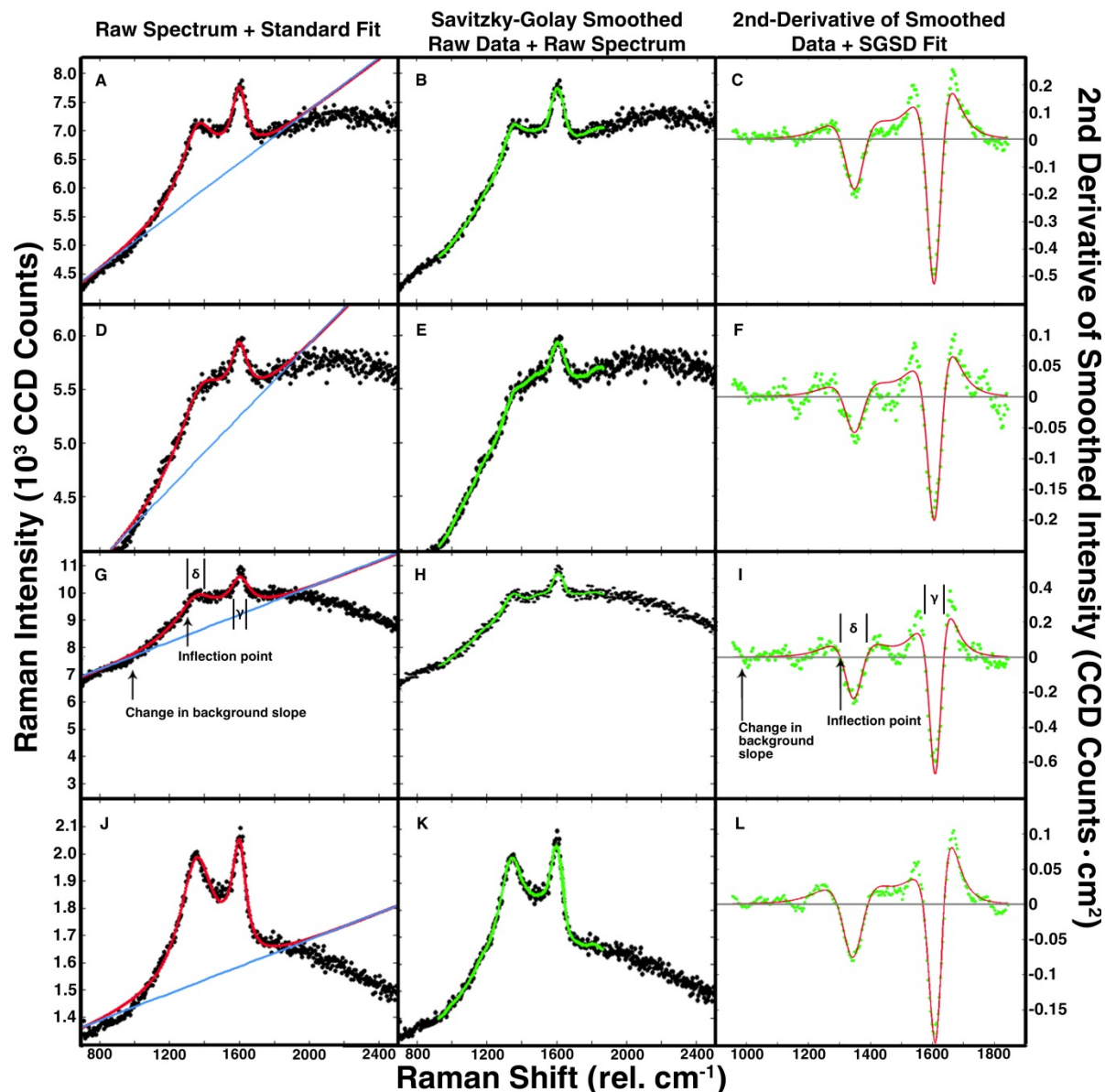
Figure 2.3: A side-by-side comparison of fits (red lines) of Raman data (black points) for four Raman spectra from CR carbonaceous chondrites. The raw data are fitted using the standard method on the left and the second-derivative of the smoothed data are fitted using the SGSD method on the right. The center column shows the Savitzky-Golay smoothed spectrum (green line) overlain on the raw data (black points). (2.3A–2.3C): an unpolished GRO 95577 (CR1) spectrum. (2.3D–2.3F): a polished EET 92161 (CR2) spectrum, the same spectra from Figure 2.2. (2.3G–2.3I): an unpolished QUE 99177 (CR3) spectrum. (2.3J–2.3L): an unpolished GRO 95577 (CR1) spectrum.

Table 2.1: Comparison of Raman parameters with 1σ uncertainties for the standard and SGSD methods for real spectra in Figure 2.3.

	Standard	1σ	SGSD	1σ	Standard	1σ	SGSD	1σ
	Figure 2.3A and 2.3C Parameters				**Figure 2.3G and 2.3I Parameters**			
δ (cm^{-1})	247.77	4.74	187.23	20.72	279.48	6.79	162.09	18.50
γ (cm^{-1})	108.06	3.77	136.13	4.35	151.60	13.02	117.23	5.50
I_D/I_G	1.094	0.020	0.713	0.096	1.128	0.042	0.770	0.100
D Position (cm^{-1})	1361.70	1.82	1349.86	3.61	1352.96	4.64	1345.09	4.71
G Position (cm^{-1})	1598.65	1.07	1600.26	1.21	1603.10	2.05	1604.06	1.99
Q	−24.16	5.88	−7.46	5.16	−50.00	0.00	−12.80	14.27
	Figure 2.3D and 2.3F Parameters				**Figure 2.3J and 2.3L Parameters**			
δ (cm^{-1})	337.32	7.11	201.77	78.65	236.26	4.32	193.29	12.15
γ (cm^{-1})	125.93	6.53	134.69	8.44	107.61	3.69	130.61	2.89
I_D/I_G	1.377	0.041	0.668	0.300	1.156	0.019	0.905	0.058
D Position (cm^{-1})	1378.43	2.28	1353.37	13.19	1353.55	1.22	1343.42	1.77
G Position (cm^{-1})	1598.70	1.71	1600.39	2.22	1598.72	0.94	1599.34	0.92
Q	−33.27	11.80	−9.66	11.33	−10.87	1.15	−3.62	0.52

2.5 Results and Discussion

2.5.1 Comparison of Data Analyzed by the Standard Method and the SGSD Method

Figure 2.3 contains four side-by-side comparisons of real spectra fit with the standard line-subtraction method on the left and the smoothed second-derivative data fit with the SGSD method on the right. The center column of Figure 2.3 shows the Savitzky-Golay (SG) smoothed data. The spectral parameters for each fit are compared in Table 2.1. Although these spectra are not completely representative of the different types of fluorescence we see in our data sets, the examples in Figure 2.3 include some of the most extreme examples of fluorescence that we see. The spectra in Figure 2.3 help prove the point that the SGSD method tends to give more consistent fits while the standard method fit parameters, in some cases, differ wildly from the SGSD method. These backgrounds have varying steepness (blue lines on the left side of Figure 2.3 show the line fitted to the background), shape, but tend to have similar amounts of noise (~ 0.5–1%).

There are a few aspects of the second-derivative spectrum that make it less intuitive to understand than the raw spectrum. First, the range in y values on the second-derivative plots is much smaller than for the raw spectra. Although deviations in the fit (red line) to the raw data look small, they are large because of the large range in y values. On the other hand, variations that appear large on the second-derivative plot are magnified because of the small range in y values on the second-derivative plots. Second, the raw baseline contains a lot of noise, which causes small variations in the smoothed spectrum. It is not important to fit the small variations (e.g., between 1000 and 1200 cm^{-1}) that get propagated into the second-derivative spectrum just as it is not important to fit small variations in the noise of the non-derivative spectra. The intensity of the noise is small compared to the intensity of the peaks, so the noise is ignored by the fitting program. If the noise is larger than the bands of interest, the second derivative fit will likely fail, but there is no expectation to fit spectra with signal to noise ratios less than one. For example, the small peak around 1500 cm^{-1} in the second-derivative spectra, is an artifact of the SG smoothing in the very noisy inter-peak valley, but not a peak.

Figure 2.3A is a spectrum from an unpolished section of GRO 95577, its smoothed spectrum is shown in Figure 2.3B and the second-derivative and resulting fit is shown in Figure

2.3C. This spectrum has a steep fluorescence background, and the curvature of the fluorescence changes in the vicinity of the D- and G-bands. Figure 2.3D is a spectrum of polished section of EET 92161 its smoothed spectrum is shown in Figure 2.3E and the second-derivative and resulting fit is shown in Figure 2.3F. This spectrum is similar to Figure 2.3A, but has a steeper background and a much lower S/N. According to Table 2.1, the widths of the bands increase substantially when the standard method is used compared with the SGSD method. However, we should be careful before drawing conclusions from Figure 2.3 because, as opposed to a simulated data set, we do not know the 'true' values of the peak widths (see Section 2.5.2).

Figure 2.3G is a spectrum from an unpolished section of QUE 99177 its smoothed spectrum is shown in Figure 2.3H and the second-derivative and resulting fit is shown in Figure 2.3I. This spectrum has a concave down background. Figure 2.3G is the most extreme example of a curved fluorescence background that begins just to the left of the D-band. Below ~ 1000 cm^{-1}, the background is relatively flat, but then it abruptly changes slope and adds curvature above 1000 cm^{-1} (see 'Change in Background Slope' label in Figure 2.3G). This change in slope is not as obvious in Figure 2.3A or 2.3D, but it is present in roughly the same place. In Figure 2.3G, the standard fit saturates the lower bound of Q (see Table 2.1), probably because the background area between ~ 1100 and ~ 1200 cm^{-1} is not properly subtracted. This part of the spectrum is fit as a part of the D-band, leading to erroneous results.

The SGSD method fits areas of concave down the best. In a practical sense, this is what one wants when fitting peaks. The part of the spectrum that we want to fit is the signal and not the noise. Mathematically, the spectral peak corresponds to the area between the most concave up parts of the data, near the inflection points. On the other hand, a non-derivative fitting process recognizes a peak by an abrupt change in slope from a flat baseline. As we can see in Figure 2.3D and 2.3G, there is very little difference in the slope of the line subtracted from the spectra and the slope of the curving background. However, the SGSD method recognizes the peak as starting near an inflection point, and where the second-derivative changes sign from positive to negative (see 'Inflection Point' labels in Figure 2.3G and 2.3I). This is the one example that exposes the difference between the SGSD method and the standard method and demonstrates how the SGSD method performs with a background composed of any smoothly varying function.

28

It is important for the fit to go through the inflection points of the D- and G-bands because the inflections points define the width of the peaks (δ and γ). The leftmost inflection point is labeled in Figure 2.3G and 2.3I. The peak 'begins' around where the second-derivative is the most positive, which is just to the left of the labeled inflection point in Figure 2.3. To the left of this area, the spectrum is dominated by background and noise, which should not be fitted. In every case, the non-derivative fit tends to include parts of the background as a part of the D-band, giving rise to very large δ values seen in Table 2.1. In some cases, parts of the background are included in the raw spectrum fit of the G-band, which overestimates γ. The SGSD peak widths, defined as the distance between the inflection points, are labeled in Figure 2.3G and 2.3I to more clearly see the how much the non-derivative fit (Figure 2.3G) overestimates the peaks widths.

The last fluorescence shape example, Figure 2.3J through 2.3L, deals with the case where the steepness of the background is opposite on each side of the D- and G-bands. In this case, the background is sloping up on the left, but is sloping down on the right. In all the other cases, the background is still increasing on the right side of the G-band, such as in Figure 2.3A and 2.3D. The background is nearly flat in Figure 2.3G to the right of the G-band. But in Figure 2.3J it is impossible to fit a line to the background because of the change in the sign of the slope. With the SGSD method, this type of pitfall is avoided, and we see that the SGSD method fits both peaks very well.

2.5.2 Simulations of Real Spectra

The disadvantage of using comparisons of the fitting techniques using real data (e.g., Figure 2.3) is that we do not know the actual values and the noise level is a variable. Thus, we cannot tell which method is more accurate. Previous experiments with simulated data provided mixed results because the simulated data was too well-behaved (Gasda et al., 2013); the backgrounds were not representative of real-world backgrounds, such as those in Figures 2.2 and 2.3. So, we must devise another simulation experiment that uses a 'real-world' fluorescence background. In this new simulation experiment, with results shown in Figure 2.4, we use an equation that features a slope break at position, S, and a background functional form change from an exponential in low wavenumbers, and a Gaussian at high wavenumbers.

$$f(x) = \begin{cases} 10^3 e^{\frac{1.6x+100}{1600}}, & x < S \\ 10^3 e^{\frac{1.6x+100}{1600}} + \frac{10}{500\sqrt{2\pi}} e^{\frac{-(x-(S+700))^2}{5\times10^5}} - \frac{10}{500\sqrt{2\pi}} e^{\frac{-(S-(S+700))^2}{5\times10^5}}, & x \geq S \end{cases} \qquad (2.7)$$

As the slope break increases, the Gaussian center also increases linearly. The third term in the Gaussian part of Eq. 2.7 ensures that the background is continuous at S. This background simulation equation has the effect of slowly varying the shape and slope of the background over a range of S values that range from 900 to 1800 wavenumbers (above 1800 cm^{-1}, this function becomes non-differentiable and the SGSD method cannot be used for this background). Figure 2.5 gives some examples of the shape of the background and the superimposed D- and G-bands at important values of S.

Susceptibility of the linear subtraction (Bonal et al., 2006; Quirico et al., 2003), line float method (Busemann et al., 2007), and SGSD fitting methods to changes in the fluorescence shape was tested by increasing S and keeping the Gaussian noise at 0.05%, on par with the noise seen in real spectra (Figure 2.3). Figure 2.4 shows the results of these tests for all the spectral parameters. In each plot of Figure 2.4, the results for each spectral parameter are subtracted from the actual value for the simulated data (Q = −4.0, I_D/I_G = 0 .535, δ and γ = 120 cm^{-1}, D Position = 1350 cm^{-1}, G Position = 1580 cm^{-1}), meaning that the data closest to zero (blue line) are the most accurate. The red line corresponds to the SGSD result, the black line corresponds to the line subtraction method, and the green line corresponds to the line float method. Errors are represented as dashed lines and they are 1σ of ~ 10^4 Monte Carlo runs. For each value of S, we simulated 120 spectra (with the same actual values and noise level, but with a new random seed to generate the noise) and performed 100 Monte Carlo runs on each spectrum.
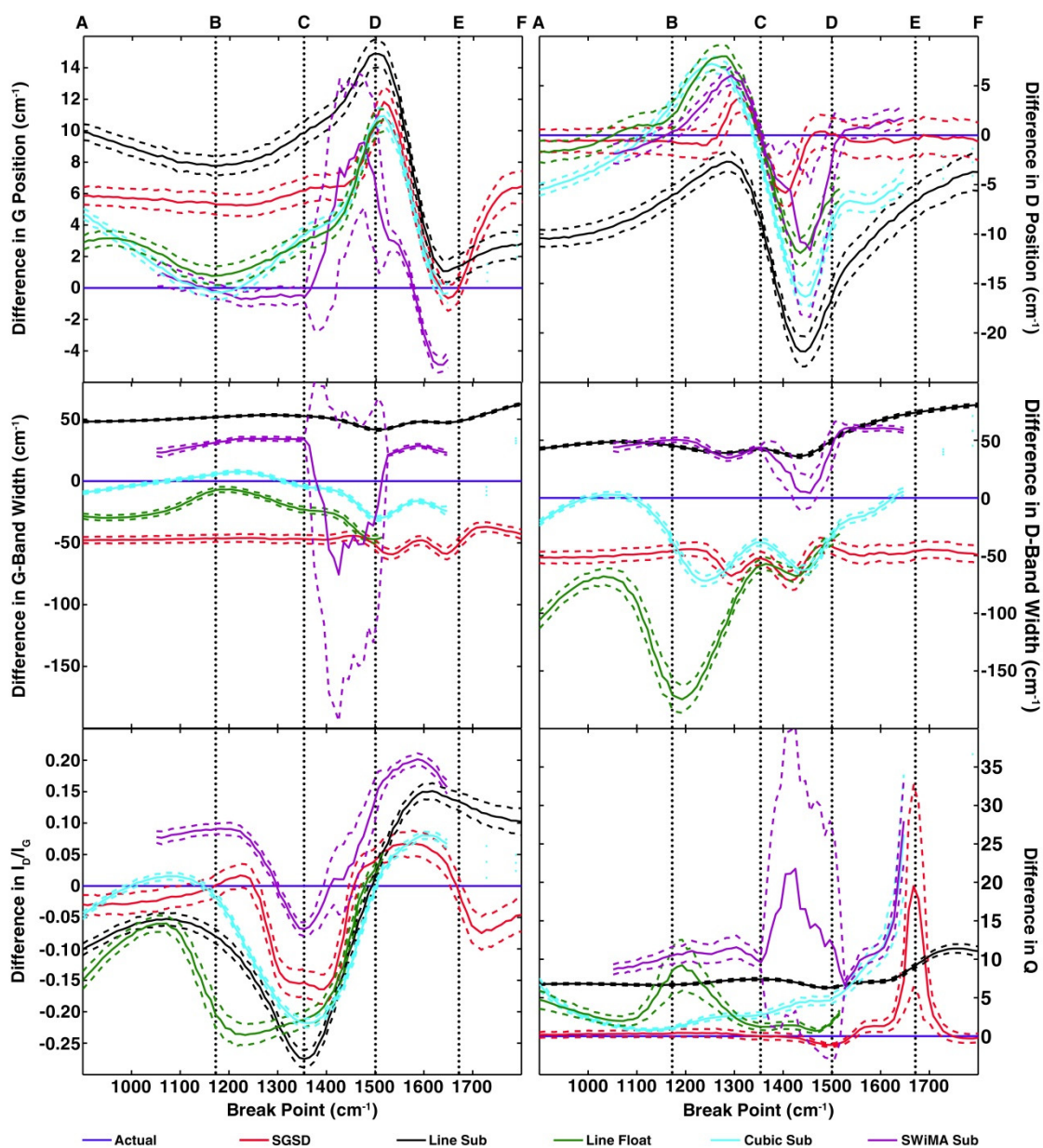
Figure 2.4: The effect of increasing the break point, S, in Equation 2.7 on the modeled Raman parameters found using the SGSD method (red), the standard method (black), the line float method (green), third-order polynomial (cubic) background subtraction (cyan), and SWiMA method subtraction with a window size of 40 and a window increment of 2 (purple) for simulated spectra. These data are plotted as the difference between the fit and the actual value. The curves closest to zero (blue line) are the most accurate values. Solid curves are most likely values.

31

Dashed curves represent the range of the 1σ of ~ 10⁴ Monte Carlo runs. Vertical dotted lines labeled A–F correspond to individual spectra shown in Figure 2.5.
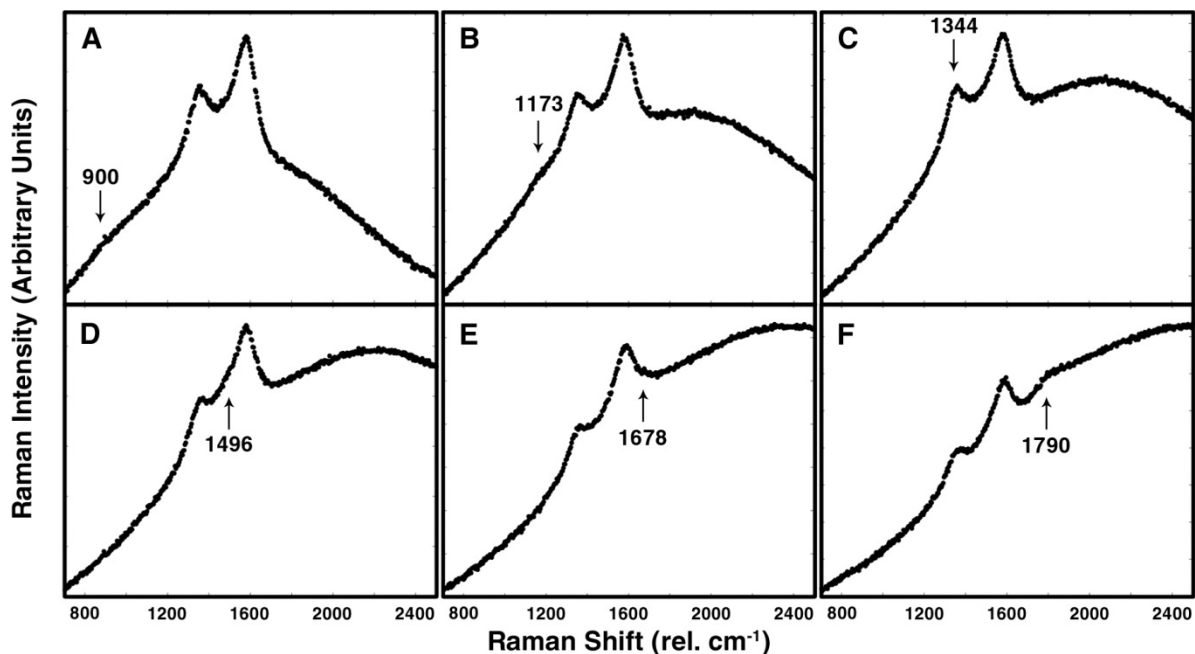
Figure 2.5: Endmember (A & F) and important simulated spectra (B–E) used for the simulation of real spectra that correspond to the vertical dotted lines in Figure 2.4. The location of the break point, S, in wavenumbers is labeled in each spectrum.

Figure 2.5A–2.5F shows the simulated spectra at specific values of S that are highlighted by the vertical dotted lines in Figure 2.4 (labeled A–F). The two endmember spectra A & F, are where S equals 900 and 1790 cm⁻¹, respectively. Figure 2.3 contains some of the real spectra we are attempting to model in this experiment. Figure 2.5A has a background that is very similar to Figure 2.3G and 2.3J, and Figure 2.5B–2.5D contain backgrounds similar to those in Figure 2.3A and 2.3D. So, we conclude that these spectra are a good representation of the types of backgrounds we see in real experiments.

Some of the plotted methods shown in Figure 2.4 have gaps in their data. For these methods, these were cases where the fitting method could not converge properly at that value of S. Typically, either the spectrum would not converge after a large number of iterations or at least one of the Raman fit parameter bounds becomes saturated. The floating line, third-order

polynomial subtraction, and SWiMA methods all have values of S that resulted with no fit convergence. For the floating line and third-order polynomial subtraction methods, Q becomes saturated as S becomes large (the background becomes dominated by the exponential). Though the third-order polynomial subtraction method does marginally better than the float line method, third-order polynomial subtraction method cannot fit spectra with S above 1678 cm^{-1} (Figure 2.5D). The SWiMA method cannot fit spectra with high S, nor can it fit spectra with S below ~ 1100 cm^{-1}, and the method has difficulty fitting between S = 1350 and 1500 cm^{-1}. We used the same parameters as Figure 2.2H for this SWiMA experiment, and the values of S that do not converge are likely due to the window size value. Figure 2.4 shows that the floating line, third-order polynomial subtraction, and SWiMA methods are not suitable for unsupervised fitting of large datasets with varying fluorescence because they cannot reliably fit all types of backgrounds.

The only two methods that converge in all the cases are the SGSD and standard line subtraction methods, so they are the most suitable for unsupervised fitting of large datasets. Figure 2.4 shows that the SGSD method is at least as accurate as the standard line subtraction method in most cases. For I_D/I_G and Q estimation, the SGSD method is the most accurate method, except in a few instances (Figure 2.4 and Figure 2.5D and E). On the other hand, the SGSD method is much less affected by variations in S. There is variation of the D- and G-band parameters only when S is directly under their respective peaks. The variation of the parameters in these ranges of S is also smaller than all of the other methods. For example, the variations in band widths and positions, due to changes in S, are about the same for the SGSD method, about 50 cm^{-1} in width and 10 cm^{-1} in position. When calculating I_D/I_G when S is under the D-band (Figure 2.5c), I_D is large compared to I_G, and vice versa when S is below the G-band, but to a lesser extent. The other techniques behave similarly for I_D/I_G estimation, but have greater variations, and they are only more accurate than the SGSD method when they cross over from over- to underestimating I_D/I_G.

The variations in the calculated Raman parameters become important when interpreting data with real Raman datasets. In many instances (Bonal et al., 2006; 2007; Quirico et al., 2003; 2009; Busemann et al., 2007; Gasda and Taylor, 2013, Rotundi et al., 2008, Sforna et al., 2014, Fries et al., 2009; Starkey et al., 2013), variations with respect to I_D/I_G (for example) are reported

in the literature. In Figure 2.4, variations in I_D/I_G of ~ 0.45 for the line subtraction and ~ 0.3 for the float line methods occur solely due to changes in the fluorescence background. The actual value of I_D/I_G in this experiment is ~ 0.5, so the variations due to changes in fluorescence background approach 100 %. If the raw Raman spectra have interference from high fluorescence, then reported data can only be considered meaningful if they have variations greater than those seen in Figure 2.4.

Because Q also influences both I_G and G-band position (Eqs. 2.5 and 2.6), it is important to pay attention to Q values calculated by any method. All methods can report large magnitude Q values, but for different reasons. Poor Q estimation occurs with the subtraction or float background methods because the background is poorly represented with a simple function, indicating that this method fits intense fluorescence backgrounds poorly. A very large in magnitude Q occurs with the SGSD method in a very specific circumstance of this simulation, when S is on the upper edge of the G-band. So spectral parameters calculated with the SGSD method that have large Q magnitudes and errors should be used with caution.

2.6 Conclusions

The non-text Supplementary Material of this paper includes our versions of the SGSD, linear subtraction, and line float method algorithms. The authors recommend that the reader try each algorithm with their own data to understand the differences between the three. All three techniques use MATLAB's fmincon constrained least-squared minimization routine with analytical gradients and Hessian matrices; this algorithm converges rapidly and is very robust compared to other minimization routines. Additionally, since the uncertainty on each pixel of the spectrum is not well quantified (and we cannot use χ^2 minimization to calculate uncertainties without knowing these uncertainties very well), a Monte Carlo method is used for estimating uncertainties.

We have justified that our method is the more accurate and robust, within the constraints of our experimental conditions, compared to other methods that assume a fluorescence background can be fit with a line or other simple functions. Visual evidence in Figure 2.3 illustrates that the SGSD method fits the real data very well. Figure 2.2 and 2.3 give examples

that show how the other methods poorly fit the background by mistaking parts of the background between 1000 and 1200 cm^{-1} as a part of the D-band peak. Yet, according to Table 2.1 and Figure 2.4, the standard line subtraction method can still be more accurate than the SGSD method in some cases, and more precise in almost every case.

However, the uncertainty of the parameter values resulting from methods using background fits do not take into account the systematic uncertainty from the variable non-linear background. The poor accounting of the background is not well appreciated until we look at examples (e.g., Figure 2.3G) that illustrate the quality of the fits using the standard method. It is clear that any method that fits a line or other function to a curve will tend to confuse the fluorescence background as a part of the D-band peak, as seen in Figure 2.2 and 2.3. The standard linear subtraction method is incapable of fitting Figure 2.3G properly because it saturates our lower bound of Q. Yet, there are many examples in Table 2.1 where the standard deviation values for the standard method are smaller than those for the SGSD method. Given these problems, how can we trust that the linear background fits (and by extension, the various other background methods tested here) are giving us the proper uncertainties? We posit that the small standard deviation values estimated by the standard method are underestimated and the higher precision can lead us into believing that the standard method is the better choice. In reality, the SGSD method is preferred because it is more effective at fitting the peaks and taking any slowly varying background into account. Additionally, the SGSD method tends to have higher accuracy when fitting simulated spectra and possibly real spectra. Therefore, we suggest that uncertainties provided by background fitting techniques are underestimated, because the basic assumption about the functional form of the background fluorescence is not accounted for in the uncertainty estimation.

Since the SGSD method can account for various types of backgrounds, it is a more robust method than a float line or background subtraction method. The SGSD method is not any better than linear background fit methods when the fluorescence background is indeed linear. However, we have shown that SGSD is generally more accurate than the other methods in a variety of other, more general, situations. SGSD varies much less than the float line, third-order polynomial subtraction, and SWiMA methods with changes in background shape, despite being less accurate in some cases for the Raman parameters.

35

The results from Figure 2.4 give us an idea of the systematic errors associated with SGSD and the other fitting methods, which then can be used as an estimate for the systematic error in real Raman spectra fit parameters if the SGSD method is used for analysis. The variations in the Raman parameters in Figure 2.4 also help us estimate the significance of the variations in our real datasets that are known to have variable background fluorescence. For a trend to be significant and scientifically meaningful, the variation of the parameters will have to be at least as large as the variations seen in Figure 2.4.

In real Raman in situ data sets, there can be other peaks around the D- and G-band, notably that of pyroxene (peak ~ 1050 cm^{-1}) (Downs, 2006), that can interfere with a background fitting technique (for example, the slope of the line would be underestimated or the y-intercept overestimated to compensate for a strong peak at 1050 cm^{-1}), and require manual tweaking of these types of algorithms. The major strength of our method is that those peaks are ignored in the fitting process completely because the peaks are not present within the inflection points of the D- and G-bands. The automatic and robust nature of the SGSD algorithm allows for unsupervised analysis of large data sets which may have backgrounds or spectral artifacts that were not addressed in this paper.

We propose on the basis of our results that the SGSD method can be applied to in situ Raman spectra of the macromolecular carbon in carbonaceous chondrites or other rock samples. SGSD produces good fits of our simulated and real Raman spectra with greater accuracy than the standard linear background subtraction techniques when varying and non-linear fluorescent backgrounds are present. In addition, we have proposed a robust method to determine the uncertainties of the Raman spectral parameters of the MMC or other graphitic materials found in rocks. The SGSD technique and Monte Carlo uncertainty estimation may be useful for other spectroscopy applications where variable and/or undefined backgrounds are present, and when uncertainties on each point cannot be well quantified. The technique may be particularly useful when it is used to analyze large Raman spectral data sets automatically, such as in situ Raman spectral images.

Chapter 3

Chemical Properties of Carbon Materials in CR Carbonaceous Chondrites: the Effects of
Aqueous Alteration

In preparation for publication in *Meteoritics and Planetary Science* as Gasda, P.J.; Hellebrand,
E; and Taylor, G.J., Chemical properties of carbon materials in CR carbonaceous chondrites: the
effects of aqueous alteration

3.1 Abstract

The CR chondrites contain up to ~ 5 wt% carbon, mainly in the form of macromolecular carbon (MMC). Members of the CR group range from petrologic type 3 (primitive) to type 1 (extensively aqueously altered), which makes these particular meteorites interesting for studying the results of fluid-organic-mineral interactions. These interactions may be analogous to the processes that led to the origin of life. We have studied the MMC using in situ Raman spectroscopy and electron probe micro analysis (EPMA). We utilized both spectral mapping and the spot analysis techniques for both instruments. EPMA mapping of the carbon Kα X-rays reveals that there are three types of carbon materials in the matrices of these chondrites: high carbon phases (HCPs), matrix carbon (MC), and calcium carbonate. Both mapping and single-spot measurements using Raman spectroscopy show that the HCP and MC spectra are consistent with MMC. Additionally, Raman shows that the MC is MMC, and that the MMC is essentially unaltered by the aqueous alteration experienced by the CR chondrites. However, high resolution EPMA X-ray mapping suggests that as aqueous alteration progresses, physical and chemical changes in the carbon do occur: the morphology of the HCPs changes, the spatial distribution of the MMC can change, the abundance of the MMC decreases, and the atomic H/C ratio increases. Apparently, the changes in the MMC structure due to aqueous alteration are below the detection limit of Raman spectroscopy. We propose multiple chemical mechanisms that could explain the morphological and chemical differences of the MMC among the CR chondrites. Future isotopic measurements may help us differentiate between possible parent reservoirs of the MMC and shed light on the mechanism that altered the MMC during aqueous alteration.

3.2 Introduction

Carbonaceous chondrites contain samples from the earliest epoch of the Solar System and even contain presolar material. They are composed of products from different stages of protoplanetary disk evolution, hence they contain a record of the processes that occurred in the protoplanetary disk, including the composition and evolution of organic chemicals that led to the origin of life on Earth (Krot et al., 2009). A central goal of our work is to better constrain the

processes that dictate the abiotic evolution of organic molecules in the early Solar System by studying the fate of organic molecules in chondrites that are thought to have undergone aqueous alteration in their parent bodies (Glavin et al., 2010; Elsila et al., 2012; Alexander et al., 2014). Water mobilizes organic molecules, serves as a medium in which molecules can react, and can be a reactant or a product in organic chemical reactions. Primary (igneous) minerals are converted into secondary (weathered or aqueously altered) minerals, minerals react with water and the soluble ions contained in the fluid, and soluble ions can precipitate into new phases (Brearley, 2006; De Leuw et al., 2010; Beck et al., 2010).

The purpose of this paper is to determine if or how the macromolecular carbon (MMC) organic materials in CR chondrites are affected by aqueous processes in the parent body. Carbonaceous chondrites contain up to ~ 5 wt% carbon. Depending on the alteration history of the meteorite, carbon can be in the form of organic molecules (primitive and aqueously altered meteorites), carbonates (extensively aqueously altered meteorites), and carbides (primitive meteorites) (Krot et al., 2007; 2009). Up to ~ 90% of the carbon is in the form of insoluble organic material (IOM), also called macromolecular carbon (MMC) herein, which is sometimes described as kerogen-like or graphite-like, and is insoluble in neutral and acidic water and most organic solvents (Sephton, 2002). MMC is ubiquitous in carbonaceous chondrites, but its chemical composition varies among meteorite groups and can change depending on the conditions of alteration of the meteorite parent body (Bonal et al., 2006; 2007; Quirico et al., 2003; 2009).

The MMC initial starting composition is not fully understood, and there is no consensus as to how or where it formed (Kerridge, 1999). MMC may have primarily formed in carbon-rich AGB stars and then was incorporated into the solar nebula (Kwok, 2004; 2009), or the MMC primarily formed in the presolar molecular cloud (Sanford et al., 2001; Busemann et al., 2006). Another possible source of the MMC is processing of organics in the solar nebula (Flynn et al., 2003) via: the irradiation of organic mantles on silicate dust grains (Nakamura-Messenger et al., 2006), irradiation of organics within ices (Ceisla and Sanford, 2012), or polymerization of formaldehyde (Cody et al, 2011; Kebukawa et al., 2013). Astronomical observations of the interstellar medium (ISM) indicate the presence of refractory organic materials that are similar to the MMC (Pendleton and Allamandola, 2002). Free floating carbon materials in the nebula are

also subject to alteration when exposed to electromagnetic radiation, and collisions with other molecules in space and high energy particles (Ehrenfreund and Charnley, 2000; Tielens, 2005). As a meteorite parent body was heated internally from the decay of radionuclides, the composition of MMC will approach that of graphite, which is the most thermodynamically stable form of carbon under all but the most oxidizing conditions (Tuinstra and Koenig, 1970; Wopenka and Pasteris, 1993; Ferrari and Robertson, 2000; Beyssac et al., 2002; 2004; Busemann et al., 2007). Small organic molecules are much more easily oxidized than MMC and they will decompose into carbon dioxide and water when heated.

Although the major types of secondary minerals are similar among the aqueously altered meteorites CI, CM, and CR, the different meteorite groups underwent slightly different styles of aqueous alteration in terms of fluid composition, temperature, and pressure (Brearley, 2006). The range of pressure and temperature conditions predicted for the individual chondrite groups, such as CR chondrites, is large (Weisberg and Huber, 2007). Thus, to fully understand how or if aqueous alteration affects MMC, we need samples of primitive chondrites that contain organic molecules and MMC that accreted from the solar nebula and samples of aqueously altered meteorites that are in the same class. Hence, we focus on the CR meteorite group because the CR chondrites have at least one example of both primitive (petrographic type 3) and completely altered meteorites (petrographic type 1), with numerous examples in between (petrographic type 2). In addition, we use both single spectra and spectral imaging to determine not only how MMC changes chemically, but if MMC changes morphologically as a result of aqueous alteration. Spectral imaging may also shed light on the petrographic relationships between the primary and secondary minerals of the meteorite and MMC.

MMC is 'insoluble' because it cannot be dissolved in the demineralization fluids or typical organic solvents used in wet chemical studies of meteorites. Hence, MMC is expected to be hydrophobic and unreactive in an aqueous system. However, past studies of aqueously altered meteorites have shown that different meteorite groups have different MMC chemical signatures in, for example, their Raman spectra (e.g., Busemann et al., 2007), ^{13}C nuclear magnetic resonance (NMR) spectra (Cody and Alexander, 2005), and carbon X-ray Absorption Near Edge Spectroscopy (XANES) spectra (Cody et al., 2008). Differences among the MMC in different

meteorite groups could result either from alteration on their parent bodies or from interactions in the solar nebula before accretion in their parent bodies.

Previous studies of MMC are grouped into two broad categories: destructive and non-destructive. Destructive techniques are characterized by their pyrolytic (e.g., thermogravimetric analysis and ICPMS) (Sephton, 2002) and demineralization techniques. Demineralization has been the primary method used to determine the structure and composition of MMC and soluble organic molecules (Busemann et al., 2007; Cody and Alexander, 2005). Typically, demineralization is a multi-step procedure of increasingly caustic, acidic, and/or oxidizing chemicals designed to leach out certain ions, hydrolyze peptide bonds, and dissolve minerals, leaving behind the carbonaceous materials. Reactions of MMC with demineralization fluids introduce an inherent bias. MMC that is resistant to acid is concentrated while the rest is altered. The leftovers are a new mixture of acid resistant MMC which is related to, but not the same, as the original carbon material. The Raman spectrum of MMC can change after demineralization (Goodyear et al., 2012).

We argue that non-destructive techniques are needed to understand the structure of MMC. In situ studies of MMC are more difficult because less material is sampled by the analytical technique in any one measurement and there are significant interferences in spectra from other materials in the sample (e.g., intense fluorescence backgrounds in Raman spectra). However, in situ studies are important because they provide information on textural relationships between the MMC and minerals, and allow for morphological studies of the MMC itself.

A few different studies have shown the utility of in situ studies of carbon in meteorites. Using TEM, Garvie and Buseck (2007) found organic carbon in phyllosilicate minerals. Two studies by Pearson et al. (2002; 2007) used osmium tetroxide (OsO_4) staining to map the organic material in meteorites at a larger scale. There have been several recent non-destructive in situ Raman spectral studies of MMC (Bonal et al., 2006; 2007; Quirico et al., 2009; 2014).

3.2.1 Raman Spectroscopy of Graphitic Materials

Typically, MMC is described as a graphite-like or kerogen-like material. The structure has a number of aromatic and aliphatic functional groups (Cody and Alexander, 2005; Remusat et al., 2005; Peeters et al., 2011; 2012a; 2012b) attached to a Raman-active aromatic carbon

structure. The extensive aromatic system in the MMC has a large Raman cross-section; the Raman signal from these groups dominates the Raman spectrum. The other parts of MMC chemical structure are not detected by Raman spectroscopy.

Graphite or graphene spectra are very similar to that of the MMC spectra, so these materials are the best model to use when describing the Raman-active portion of MMC. Pure graphite is composed of sheets of sp^2 hybridized carbon atoms arranged in a hexagonal pattern, also called a 'honeycomb' or hexagonal lattice. Carbon atoms in the sheets are aromatic. Defects, for example single and double carbon vacancies, 5-8-5 ring and 5-7-7-5 ring (Stone-Wales) defects (e.g., Kotakoski et al., 2011), grain boundaries (Biró and Lambin, 2013), and adsorbed, chemisorbed, and intercalated species (Casiraghi et al., 2007) commonly occur in graphite and graphitic materials. Defects decrease the aromaticity of the carbon (see Dietz et al., 2000; El-Barbary et al., 2003; Hashimoto et al., 2004; Kudin et al, 2008; Terrones et al., 2010 and references therein).

Raman spectroscopy measures shifts in photon energy that occur when a sample scatters light from an incident laser source and excites an electron to a virtual state. The electron can either emit a phonon (Stokes process), absorb a phonon (Anti-Stokes process), or neither emit nor absorb a phonon (Rayleigh or elastic process), and then undergo radiative relaxation (Dresselhaus et al., 2005). Scattering processes that create/absorb phonons shift the energy of the laser line, producing a Raman spectrum that is unique to the sample. The MMC Raman spectrum is characterized by two major bands (Figure 3.1, green curves), the D-band (~ 1350 cm^{-1}) and the G-band (~ 1600 cm^{-1}). The G-band is the first-order Raman scattering mode for graphite. The D-band is due to the scattering of the electron off a defect or edge (Cançado et al., 2002).

Fluorescence makes the interpretation of Raman spectra challenging. Figure 3.1 shows the raw spectrum (black dotted curve) from the GRO 95577 sample that is typically seen in our Raman mapping dataset. The fluorescence feature in the spectrum is the very intense and broad band that is centered at ~ 2200 cm^{-1}. The typical approach to interpreting Raman spectra of carbonaceous materials is to fit the bands with a model and calculate the parameters of the bands (band width, intensity ratio, and position) and their uncertainties. This requires some treatment of the background, whether the background is fitted with a function (Bonal et al., 2006; 2007; Rotundi et al., 2008; Quirico et al., 2003; 2009; 2014; Sforna et al., 2014) or a spline (Fries et al.,

2010) and subtracted before modeling the spectrum or fitted along with the spectrum (Busemann et al., 2007). Some systematic studies have been done to assess how changing background fluorescence affects the accuracy or precision of these different methods (Schulze et al., 2005; Rotundi et al., 2008; Gasda and Ogliore, 2014). The systematics of spectral fitting are especially important when dealing with large datasets of Raman spectra, where sifting through the multitude of data to discard 'bad' data would be extremely tedious. Moreover, discarding 'bad' data introduces a bias to the results.

3.2.2 Modeling the Raman Spectrum of MMC

To model the Raman spectrum of the MMC, we use a newly developed method called Savitzky-Golay Second Derivative (SGSD) fitting (Gasda and Ogliore, 2014). We use the typical LBWF (Lorentzian and Breit-Wigner-Fano) model (Ferrari and Robertson, 2000; Bonal, et al., 2006; Quirico et al., 2009) for the spectral parameters that include the 'Q' (asymmetry) factor to account for the asymmetry of the G-band:

$$F_L = I_1 \frac{\delta/2\pi}{(x-\omega_D)^2 + (\delta/2)^2} \tag{3.1}$$

$$F_{BWF} = I_2 \frac{[1+2(x-\omega_G)/Q\gamma]^2}{1+(2(x-\omega_G)/\gamma)^2} \tag{3.2}$$

The variables of F_L (Lorentzian function, light green dashed curve in Figure 3.1) and F_{BWF} (Breit-Wigner-Fano, asymmetric Lorentzian function, olive dashed green curve in Figure 3.1) correspond to the spectral parameters of the D- and G-bands. The variables I_1 and I_2 are related to the intensity (Eqs. 3.3 and 3.5), ω_D and ω_G are the peak positions (cm^{-1}), and δ and γ are the full width at half maximum (FWHM) (cm^{-1}) of the D- & G-bands, respectively. Q is the asymmetry factor of the G-band. The G-band asymmetry arises from the coupling of the G-band mode with the continuum. Since the G-band is modeled with an asymmetric line shape, band parameters need to be derived from these equations that involve the asymmetry factor Q.

$$I_G = I_2 * \left(1 + \frac{1}{Q^2}\right) \tag{3.3}$$

$$\text{G-band Position} = \omega_G + \frac{\gamma}{2Q} \tag{3.4}$$

The intensity of the D-band, I_D, is calculated using Eq. 3.5.

$$I_G = \frac{I_1}{\pi\delta} \tag{3.5}$$

43
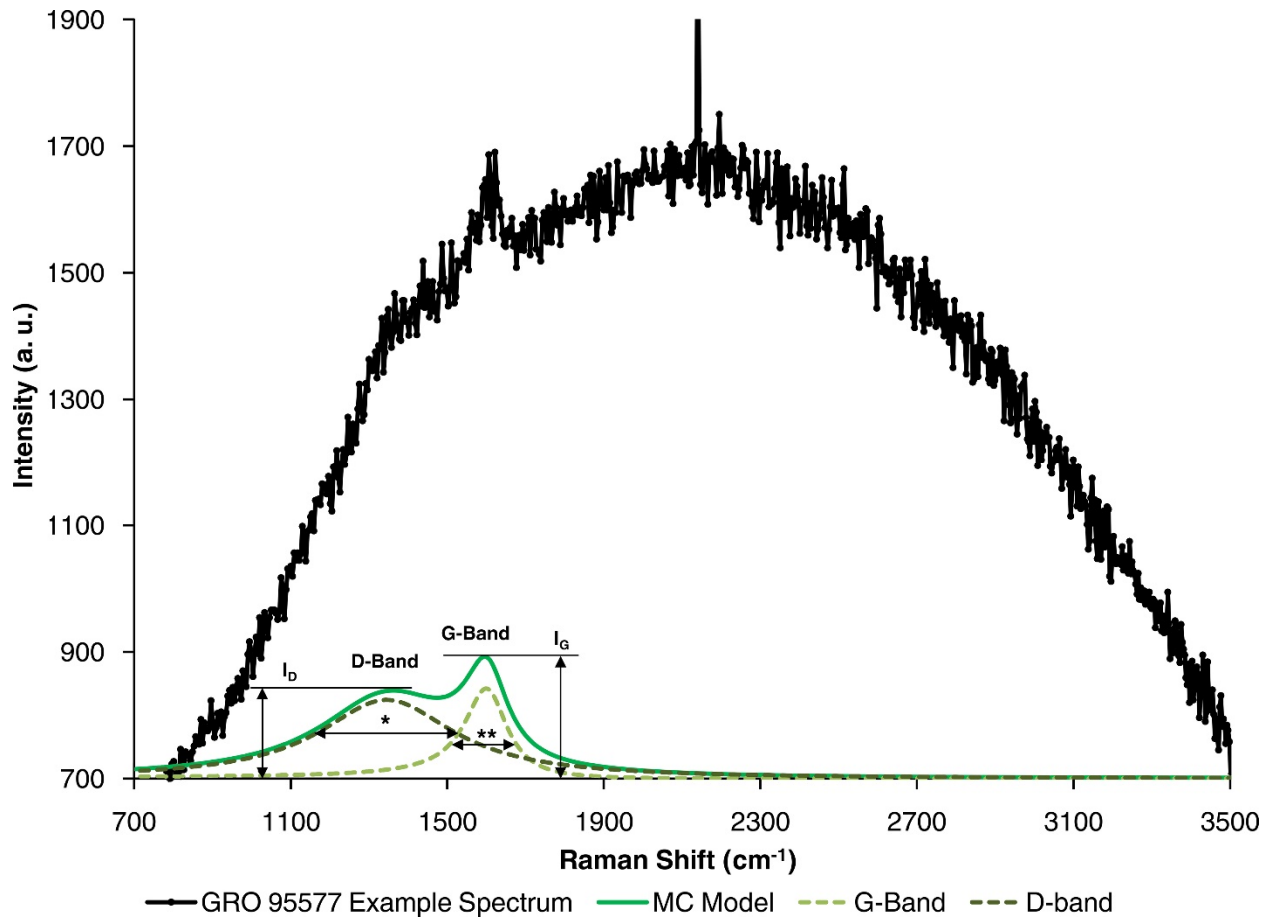
Figure 3.1: A typical raw Raman spectrum of macromolecular carbon from the CR chondrites (black). This particular spectrum is an individual spectrum (15 s integration time) from a Raman spectral map of GRO 95577, modeled (green curves) using the Savitzky-Golay second derivative method (see text). The green dashed curves show the Lorentzian (dark green dashed curve, Eq. 3.1) and Breit-Wigner-Fano (light green dashed curve, Eq. 3.2) component functions of the Savitzky-Golay second derivative model (solid green curve) of the raw spectrum. The model spectrum D- and G-bands are labeled with band intensity (I_D and I_G), D-band width (labeled with an asterisk) and G-band width (labeled with a double asterisk).

44

Rather than subtracting or fitting the background, our new method smooths the spectrum with a second-order Savitzky-Golay smoothing function over a small spectral window, and then takes its second derivative. Then the second derivative of Eqs. 3.1 and 3.2 are used to fit the data. Using a resampling Monte Carlo technique, where the noise from the original spectrum is randomized and added to the smoothed original spectrum, simulated spectra are modeled. All of the simulated Raman spectra are fit with the SGSD method, producing a distribution of fit parameters. The most likely value from these distributions is found and reported as the Raman fit parameters while the uncertainties of the reported values are the standard deviation of these distributions. The performance of this technique is described in greater detail by Gasda and Ogliore (2014).

3.2.3 Comparison with Previous Literature Results

There are two main differences between our work and the literature. First, we are using completely non-destructive methods and we are focusing on in situ analysis only, whereas many previous results have used acid dissolution techniques. Second, we have designed a new fitting method expressly for the purpose of analyzing the Raman spectrum of MMC when there is intense and variable fluorescence present in the spectrum. Previous literature tends to rely on background fitting techniques, which we have shown in Gasda and Ogliore (2014) to be not robust enough to fit large datasets of this type, nor do the fits yield accurate results. Some Raman spectra reported in the literature can have very intense fluorescence backgrounds, and because of the limitations of background fitting techniques, these spectra are discarded from models (e.g., Busemann et al., 2007; Starkey et al., 2013; Sforna et al., 2014), potentially biasing the results. Since our new SGSD method is much more robust, we can avoid introducing biases to our results.

Gasda and Ogliore (2014) shows that when fluorescence backgrounds are fit with a function (such as a line or a polynomial) the D-band peak widths tend to be overestimated. For example, Busemann et al. (2007) uses a technique that fits the background with a line and the D- and G-bands with Lorentzian functions simultaneously. Table 1 in Busemann et al. (2007) shows that spectra from the various aqueously altered chondrites (CI, CM, CR, some CO and ungrouped meteorites) have intense fluorescence (≥ 10 % of the spectra were discarded,

potentially biasing these results). Our work shows that the technique that fits the Raman bands simultaneously with the background tends to greatly overestimate some Raman fit parameters such as D-band width. If our results are correct, then there is a potential problem with Eq. 1 from Busemann et al. (2007), which depends greatly on D-band width. Cody et al. (2008) reports that Raman is not reliable enough to determine the petrographic grade or peak metamorphic temperature of a meteorite, and presents a technique using carbon XANES. Cody et al. (2008) use data from Busemann et al. (2007) to support this claim and proposes an improved equation to determine peak metamorphic temperature using carbon XANES results. However, we believe that the Busemann et al. (2007) model could be improved significantly for the samples with high fluorescence backgrounds, decreasing both the scatter in the results and the potential for sample bias, if the new data analysis and interpretation techniques were employed.

The SGSD technique also introduces a new method for determining uncertainties by Monte Carlo estimation. Other workers tend to use chi-squared minimization to determine uncertainties on the Raman fit parameters. Chi-squared minimization is only applicable when the uncertainties on each raw data point are known. Since this cannot be known well when there is a fluorescence background, we decided to implement a difference uncertainty estimation method instead. The SGSD method uses a Monte Carlo technique that resamples the noise from the original spectrum 1000 times and adds this noise to the original smoothed spectrum to produce and fit 1000 simulated spectra, resulting in a distribution of Raman fit parameter values (1000 values for each parameter distribution). The maximum likelihood value of these distributions gives the solution, and the standard deviation of the distributions gives the uncertainty on the parameter. The advantage of this technique is it does not require distributions to be Gaussian and it is a more intuitive approach for estimating the uncertainty.

Lastly, Gasda and Ogliore (2014) shows the requirements which are needed for a scientifically meaningful, and not just statistically significant, result. Since statistically significant differences can have a large effect on interpretations of data (e.g., statistically separated results could be interpreted as a signature of chemically heterogeneous MMC in the meteorite), we need to determine if these differences have any scientific meaning. For example, depending on the shape of the baseline and the resulting fit parameters, intensity ratio can vary by almost 100 % of the actual value. SGSD tends to have more consistent results, but it still

suffers from this problem to a lesser degree. Thus, Figure 2.5 of Gasda and Ogliore (2014) shows that the threshold for a meaningful result is much higher than the analytical uncertainties (1σ of the fit parameter); the threshold depends on the background fitting technique used for analysis. The threshold for scientifically meaningful results while using the SGSD method tends to be less than the threshold for other techniques when intense and variable fluorescence is present in the Raman spectrum.

3.3 Analytical methods

3.3.1 Sample Preparation

We were allocated three specially prepared chips of CR chondrites from the Johnson Space Center Meteorite Curation Laboratory. Specifically, the Antarctic meteorites Queen Alexander Range (QUE) 99177 (CR3), Elephant Moraine (EET) 92161 (a CR2 sample paired with meteorite EET 92042), and Grosvenor Mountains (GRO) 95577 (CR1). We used chips free of fusion crust. The samples were not impregnated with epoxy, and the meteorites were cut or chipped dry rather than cut with oil or water. One side of the EET 92161 and GRO 95577 meteorite chips was polished with fine diamonds and washed once with 95 % ethanol. The QUE 99177 chondrite QUE 99177 was too friable to polish without fortifying it with epoxy, so we used an unpolished chip for Raman studies and crushed dust for EPMA.

3.3.2 Raman Spectroscopy

All Raman experiments were performed using a WITec Raman alpha300 R confocal microscope spectrometer with a 5 W frequency doubled solid-state Nd:YAG laser. Raman images were collected using integration times of 15 s per pixel, $\sim$ 10 μm laser spot size (20x objective). Laser power of $\leq$ 50 μW was achieved using a series of neutral density filters. One 100 μm^2 image took $\sim$ 15 hours to collect. Single Raman spots were collected with the same power and spot size settings for 2 hours each (240 s integration time and 30 accumulations). All Raman spectra were standardized using a pure Si-wafer with a true Raman line at 521 cm^{-1}.

3.3.3 Raman Data Reduction

Approximately 68,000 spectra among 26 Raman images were collected for this project. In order to analyze this large data set, we used the Linux-based Condor high-throughput computer software (HTCondor, Univ. Wisconsin, Madison) located at Hawaii Institute of Geophysics and Planetology. This software allows programs to run in parallel on a set of networked computers, greatly decreasing the amount of time needed to perform a task. Our data were analyzed over ~ 300 equivalent CPU days (each spectra taking 400 s to analyze on average), which amounted to ~ 7.5 real time days on the Condor system.

Laser power for our instrument did not fluctuate more than 0.1 μW over the course of recording a single 15 hour map. For all images presented in the main text, the average laser power for nine GRO 95577 images was 45.5 ± 0.6 μW and the average laser power for 14 EET 92161 images presented in the main text was 41.8 ± 3.4 μW. The average laser power for the 52 single-spot experiments for all samples was 44.3 ± 2.9 μW.

3.3.4 EPMA mapping and quantitative analysis

The Smithsonian Institution National Museum of Natural History (NMNH) provided new standards that were prepared by the University of Hawai'i, Mānoa Lapidary Facility. Standards of anorthoclase (NMNH 133868), augite (NMNH 122142), calcite (NMNH136321), fayalite (NMNH85276), A-99 basaltic glass (NMNH113498-1), magnetite (NMNH 114887), San Carlos olivine (NMNH 111312-44), and Lake County plagioclase (NMNH115900) were embedded into epoxy bullets and mounted in a single 1"-round Al sample holder. A graphite sample (Graphtek LLC, > 99.9 %) was used as a carbon element standard for EPMA and pressed into gold foil (EPSL, 99.999 %, cleaned by ion sputtering and annealed) which is mounted on a sample holder.

The EET 92161 and GRO 95577 samples were embedded in indium metal (Indium Corp, 99.999 %) inside a copper jacket. QUE 99177 sample dust particles were pressed into a clean gold foil mount (EPSL, 99.999 %, annealed). Indium and gold mounted meteorite samples, as well as the standards, were simultaneously coated with 25 nm of aluminum (Lesker, 99.99 %) measured with a FTM-2000 thickness sensor in a Torr International Coater metal evaporation/coating chamber. The Al coating is still conductive in the electron probe because the oxidation layer is only on the surface of the Al.

All electron microprobe analysis was performed using JEOL JXA-8500F field emission gun EPMA instrument at the University of Hawai'i, Mānoa. For every sample measurement, 10 KeV accelerating voltage and 5 nA probe current was used. Typical spot analyses used a beam diameter defocused to 1–3 µm. X-Ray images were collected in each sample at high spatial resolution (0.5 µm pixel size and 1024 × 1024 pixels) and low spatial resolution (1–2 µm/pixel), using a 20 ms dwell time per pixel. The Kα energies of the elements C, Ca, Mg, Si, and Al, as well as backscattered electron signal (BSE) were collected simultaneously for each map.

After the mapping phase of this study, quantitative EPMA spot measurements were performed on each of the three meteorite samples to ascertain the abundance of carbon in the matrix. All the major species in the matrix (Si, Al, Fe, Mg, Ca, Na, S, and K) were measured along with the direct measurement of the carbon Kα X-rays in order to calculate the actual carbon abundance using mass absorption coefficients (MACs) and phi-rho-z corrections (also known as ZAF corrections). For this work, calculations were done using the Full Pouchou and Pichoir correction with FFAST MACs built into the Probe for Windows (Probe Software Inc., Eugene, OR) software (Chantler et al., 1995; Chantler et al., 2005). See the Supplementary Materials for more details on how we reduced the data.

3.4 Results and Discussion

3.4.1 Description of Samples and Regions Studied

Detailed descriptions of the meteorite samples QUE 99177 (type 3) and GRO 99577 (type 1) can be found in the literature (Weisberg and Prinz, 2000; Perronnet and Zolensky, 2006; Weisberg and Huber, 2007; Abreu, 2007; Abreu and Brearley, 2010). EET 92161 has not been previously described, but it is paired with EET 92042 (see Abreu and Brearley, 2004). The CR chondrites are breccias containing Mg-rich silicate chondrules with Fe-Ni metal and sulfide inclusions, abundant matrix, and rare CAIs or other refractory phases. The matrix in CRs usually contains aqueous alteration products such as phyllosilicates. The matrices of the CRs also contain 'dark inclusions,' or areas of the matrix with more abundant alteration products (e.g., calcite and phyllosilicates) (Weisberg et al., 1995). More recent studies have shown that QUE 99177 has seen limited amounts of aqueous alteration (Bonal et al., 2013). GRO 95577 is a type

1 CR that is completely aqueously altered; the chondrules are replaced with phyllosilicates and the matrix has abundant magnetite and calcite.

Figures 3.2–3.5 show the EPMA image data for QUE 99177, EET 92161, and GRO 95577, respectively. Each Figure shows the backscatter electron (BSE) image along with two red green blue (RGB) false-color images of the C-Si-Ca X-ray maps, the Mg-Si-Al X-ray maps, and one single channel greyscale image of the carbon X-ray map. The C-Si-Ca false-color images are useful for differentiating between the different phases of carbon; solid phases of carbon are bright red, calcite grains are purple, and silicon carbide would be yellow-orange. The Mg-Si-Al false-color images are useful for seeing the silicate phases and the matrix materials: forsterite is red-orange, Mg-pyroxenes are light orange, calcium aluminum inclusion (CAI) minerals are bluish-green in both false-color images, matrix materials are dark green and brown, and metals and sulfides appear black in false-color (and correspond to bright areas in the BSE image).

QUE 99177 (CR3) (previously characterized by Abreu, 2007). The surface of the sample is too uneven and is too friable to cut into a section without epoxy; no Raman maps could be recorded for QUE 99177. We collected twelve single spot spectra on all sides of the sample. For EPMA X-ray mapping, a grain mount of this sample was prepared. During mounting of the grain, the grain was crushed, damaging the sample. Nevertheless, the petrologic context of the sample is preserved. The grain mount contains both mineral and matrix portions. The mineral portion includes a Ca- and Al-rich area in Figure 3.2B in the lower left (likely formerly a CAI), and olivine and pyroxene areas are present throughout the samples (likely formerly chondrules or mineral grains). The matrix material (dark brown in Figure 3.2A) is abundant and has small variations in composition, including in its carbon content (see Figure 3.2C).
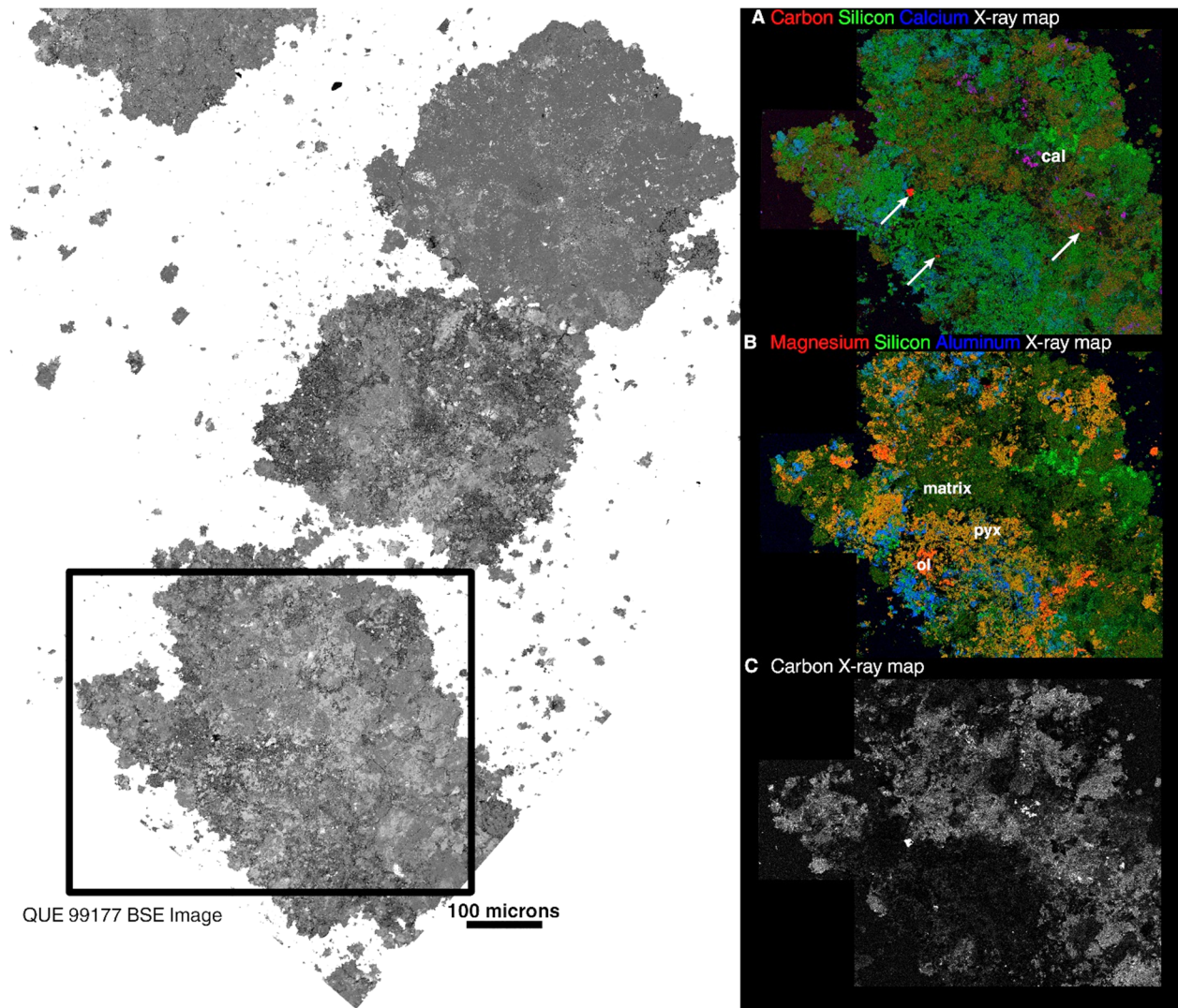
Figure 3.2: EMPA BSE image of the QUE 99177 grain mount (left) and X-ray maps (A–C) for the area shown in the black box in the BSE image. All the images are to the same scale shown in lower right corner of the BSE image. A) Carbon (red)-silicon (green)-calcium (blue) false-color X-ray image, in which calcite grains appear purple. Arrows in A point to three different high carbon phases. B) Magnesium (red)-silicon (green)-aluminum (blue) false-color X-ray image. Examples of olivine (red-orange) and pyroxene (orange) grains are labeled. C) Carbon greyscale X-ray map image.
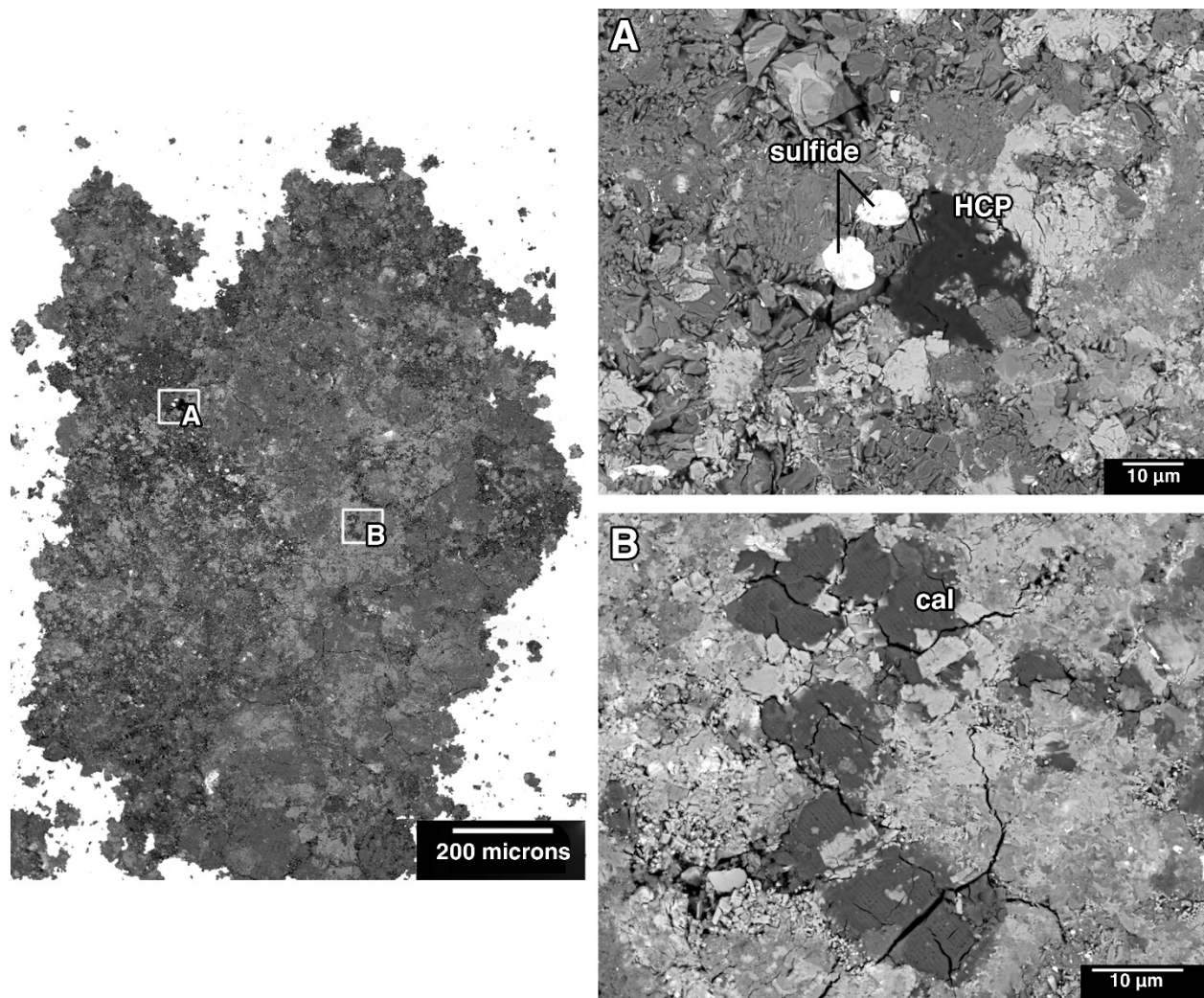
Figure 3.3: High resolution BSE images of an example of a high carbon phase (HCP) (A) and calcite grains (B) in the QUE 99177 grain mount (left). The left BSE image is the overview image of one portion on the QUE 99177 grain mount with two areas (A and B) surrounded by white boxes. On the right, two BSE images of the areas labeled A and B at a higher magnification. The HCP in A (leftmost arrow points to it in Figure 3.2A) is extremely dark in BSE and surrounded by matrix to the right and silicate grains from a crushed chondrule to the left. The calcite grains in B (labeled as 'cal') are dark in BSE and are surrounded by matrix grains on all sides.
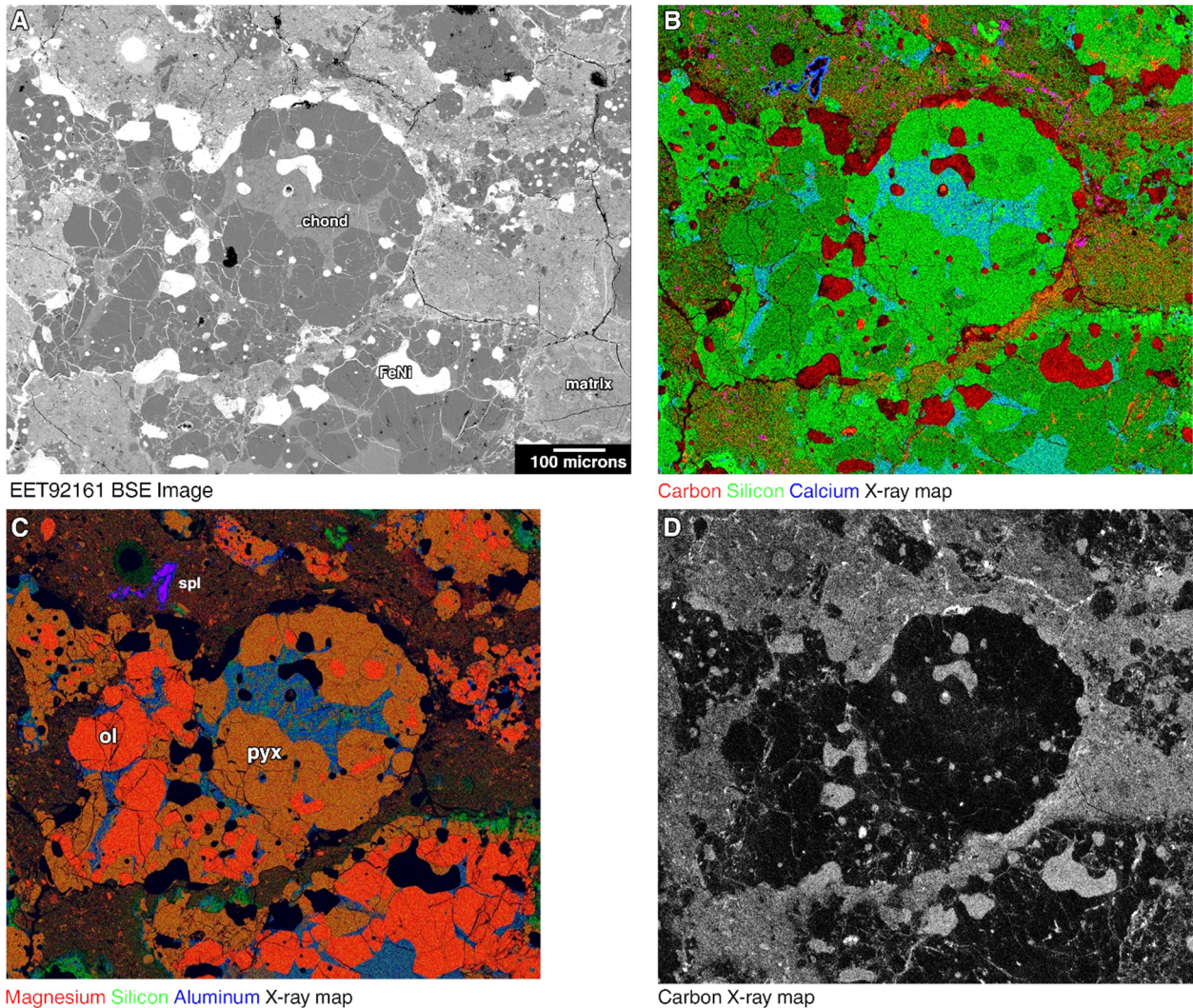
Figure 3.4: EMPA BSE image of a chondrule in the EET 92161 sample (A) and the associated X-ray maps (B–D). All the images are to the same scale shown in lower right corner of A. (B) Carbon (red)-Silicon (green)-Calcium (blue) false-color X-ray image. Diamond contamination in B (bright red phases and along a crack in upper right of B) are not high carbon phases, and can be seen in cracks, in small pits, and inside metal grains. Metal grains are bright white in A, where one is labeled. The major carbon phase in EET 92161 is matrix carbon. (C) Magnesium (red)-Silicon (green)-Aluminum (blue) false-color X-ray image with examples of the major phases labeled. (D) Carbon greyscale X-ray map image.

A few carbon phases stand out in the QUE 99177 carbon images in Figure 3.2. The bright red phases Figure 3.2A (three arrows point out prominent examples and the leftmost example is shown in Figure 3.3A) that correspond to bright parts of the carbon x-ray map (Figure 3.2C) appear to be almost pure organic material. These spots were verified as being a part of the sample by looking at the secondary electron image for these areas. Errant dust grains on the surface of a sample or cracks/holes in a sample (which can be a problem with poorly polished samples and samples that are not embedded with epoxy such as these) can cause sample charging, resulting in a brightening of the BSE and C X-ray images. These carbon areas, which we dub High Carbon Phases (HCPs), are any non-mineral carbon phase seen in these images > 1 μm in size. Unlike the diamonds used for polishing, HCPs have no chemiluminescence when hit by the electron beam. The prominent HCP shown in Figure 3.3A is ~ 10 μm across. HCPs are more resistant to electron beam damage than the calcite grains in this sample.

The two other types of carbon phases seen in QUE 99177 are calcite and what we call Matrix Carbon (MC). MC (dark brown in Figure 3.2A) is carbon that is associated with the matrix material (dark green in middle right of the image). The amount of carbon in MC is variable, but the carbon abundance of the MC is lower than the abundance of carbon in calcite (C is ~ 12 wt% in calcite). We tentatively characterize the MC as extremely fined grained carbon phases that are much smaller than the EPMA instrument BSE spatial resolution (even at the highest magnification, no individual phases can be discerned) and finely intermixed with the silicate phases of the matrix. Calcite grains are seen as purple in Figure 3.2A and in a higher magnification BSE image in Figure 3.3B. Calcite grains were only seen in this one part of our QUE 99177 grain mount, and they are surrounded by matrix materials associated with relatively low amounts of MC. It is possible that this part of the meteorite is a dark inclusion, but it is difficult to determine if it is a dark inclusion with just this information (see later sections).

The portion of polished surface of EET 92161 (CR2) is shown in Figure 3.4. This sample is a breccia characterized by the presence of primary minerals such as olivine and pyroxene in chondrules (primarily porphyritic but there is one radial chondrule in this section that is not pictured) and lithic clasts, sulfides, and Fe-Ni metal. There appears to be a small CAI in the upper left of the area imaged in Figure 3.4, identified by the presence of two large spinel grains with hibonite inclusions and calcium rich rims. The CAI is almost completely unaltered. There

also is an unaltered Ca-Al-rich glassy mesostasis within the chondrule in the middle of the images in Figure 3.4. Abreu and Brearley (2004) reported that secondary minerals occur in the fine-grained matrix of meteorites paired to this sample, but the portions of EET 92161 that we have studied appear unaltered. This sample has been moderately terrestrially weathered (weathering grade B/C, according to the Meteoritical Bulletin (Grossman and Score, 1996)), so it has many iron-rich weathering veins cross-cutting the sample, although they are not immediately apparent in the images in Figure 3.4.

MC is likely the main carbon phase in EET 92161. Because this sample has been heavily fractured and has many plucked grains, it is difficult to obtain BSE images for most of the sample; thus, Figure 3.4 is one of the few intact parts of the sample suitable for EPMA study. Unfortunately, many cracks and holes are contaminated with diamonds from the polishing process, which can be seen clearly in the top right false-color X-ray image. Visually, these high carbon areas can be mistaken for HCPs, but they exhibit chemiluminescence when the electron beam is focused on them. Hence, there are no confirmed HCPs in this sample. We found no evidence for extraterrestrial calcite; calcite present in veins are likely due to terrestrial weathering. Nevertheless, the sample is interesting because it has abundant MC, and we mapped the sample extensively using Raman (see Section 3.4.3), so it is useful for studying the evolution of carbon phases in the CR chondrites.

There appears to be elevated carbon in the metal grains. This could be a real signature of carbon in the sample, but it is unlikely for three reasons: the higher electron backscatter increases the background in the carbon region of the X-ray spectrum, the sample was roughly standardized on graphite coated with 25 nm aluminum but not a proper metallic Fe standard, and the carbon might be diamond contamination from the polishing. Without a proper standard it would be difficult to accurately assess the actual abundance of carbon in the metal, but it is certainly above the background. Contamination seems to be the most likely explanation because we already have evidence for diamond contamination in the rest of the sample. Although the polished samples were briefly washed with ethanol at the Meteorite Curation facility, the washing step did not clean diamonds out of the ubiquitous cracks and holes in the EET 92161 sample. Metals are soft, so the diamonds might be easily embedded onto the surface. The electron beam penetration depth into the metals is very low at 10 KeV, which the setting used to map the samples, so the

metal compositions are dominated by anything at the surface, such as diamond contamination. Analytical artifacts, possibly resulting from surface contamination or C ingrowth during analysis, are considered unlikely, considering the oil-free vacuum system (scroll and turbomolecular pumps). Several tests on standard materials were run to assess these effects (see Appendix).

Figure 3.5 shows a portion of the polished surface of GRO 95577 (CR1). Detailed petrographic descriptions for this meteorite are available (Weisberg and Prinz 2000; Weisberg and Huber, 2007; Perronnet and Zolensky, 2006). The GRO 95577 sample is characterized by chondrules that are completely replaced by secondary phyllosilicates. Additionally, there are abundant alteration products that crystallized from fluids such as magnetite and calcite, but the sulfides remain unweathered. Some large magnetite blebs have rims or are layered and appear to have been altered in place rather than crystallized from an aqueous fluid. Dolomite was not detected. Aside from a few rust colored spots in a different part of the sample (not shown in Figure 3.5), this sample has experienced very little terrestrial weathering. GRO 95577 contains carbon as MC, calcite, and HCPs, but the HCPs are morphologically different from those in the other samples (see below) and they are almost always associated with other alteration products.

Calcite-magnetite assemblages (CMAs), are common throughout this sample, and almost all have associated HCPs (e.g., Figure 3.6A). The HCPs in GRO 95577 are morphologically distinct; they are composed of diffuse masses or clumps of individual HCP 'grains' that are ≤ 1 µm in size. There could be two reasons why these diffuse HCPs seem to exist almost exclusively near CMAs: either the diffuse HCPs formed with the CMAs or the CMAs preferentially crystallize around the diffuse HCPs. We predict that the latter scenario is the case because, if the diffuse HCPs are indeed MMC, then there is no evidence that this material should dissolve in water, even if it is hot or extremely acidic/caustic. The reason for preferential crystallization of the CMAs around the diffuse HCPs is not yet understood.

A
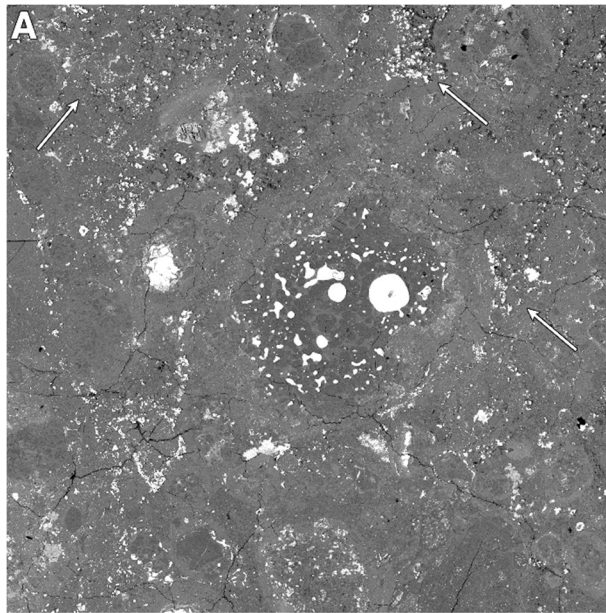
GRO95577 BSE Image

B
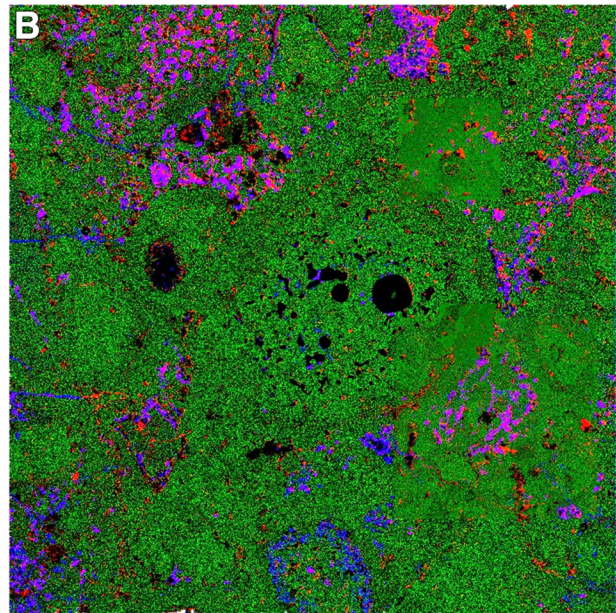
Carbon Silicon Calcium X-ray map

C
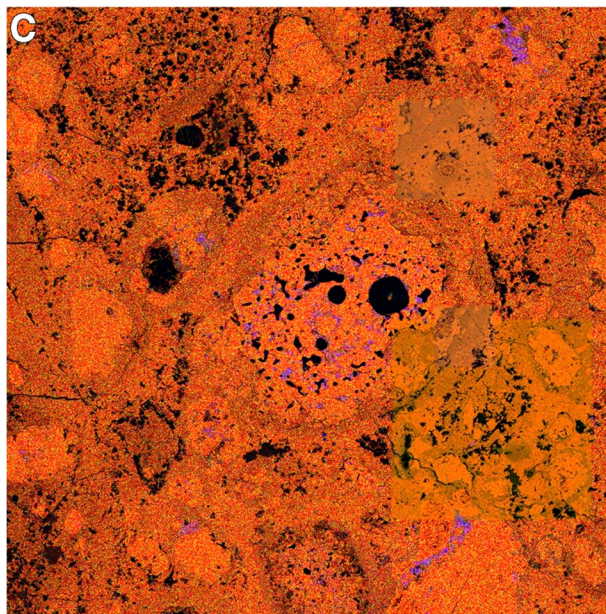
Magnesium Silicon Aluminum X-ray map

D
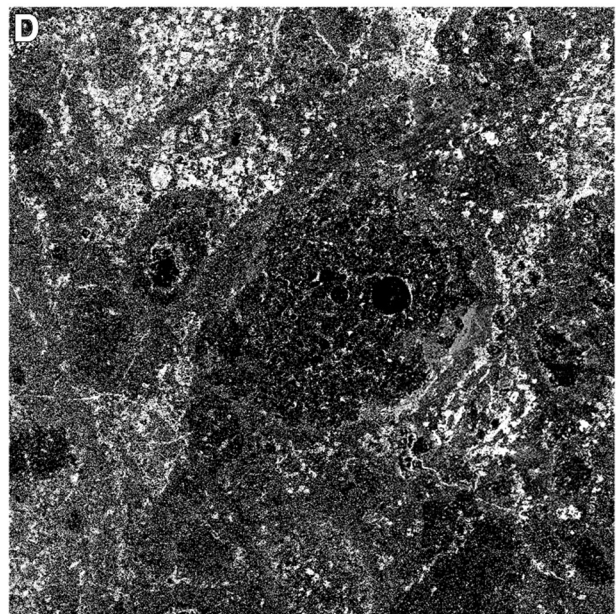
Carbon X-ray map

500 microns

Figure 3.5: EMPA BSE image of a portion of the GRO 95577 sample (A), with arrows pointing out three examples of prominent calcium-magnetite assemblages, and the associated X-ray maps (B–D). All the images are to the same scale shown in lower right corner of the carbon image. (B) Carbon (red)-Silicon (green)-calcium (blue) false-color X-ray image. (C) Magnesium (red)-Silicon (green)-Aluminum (blue) false-color X-ray image showing that the sample is dominated by Mg-rich phyllosilicates formed by in-place aqueous alteration of the chondrules. (D) Carbon

greyscale x-ray map image, where bright areas are calcite grains and mid-tone areas are where carbon is present in the matrix.
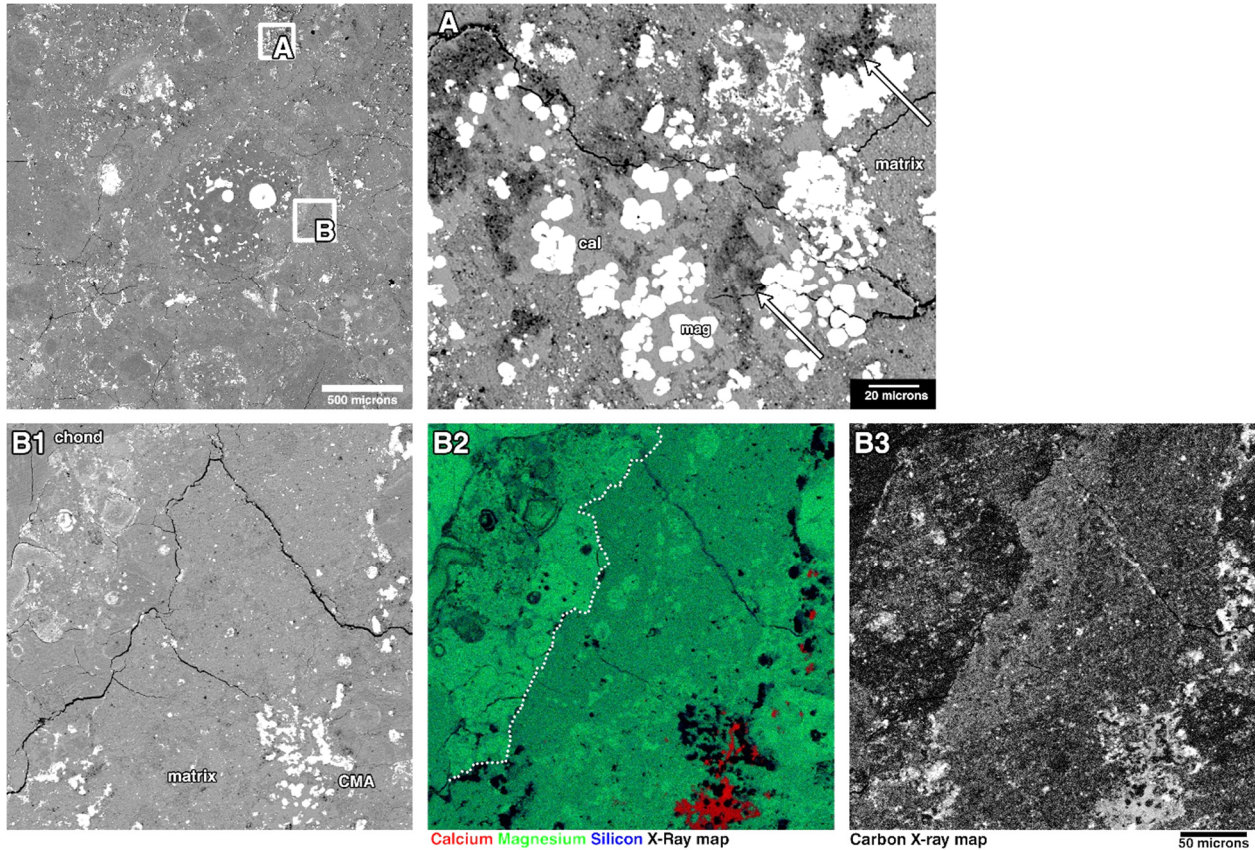
Figure 3.6: An example of CMAs (calcite-magnetite assemblages) (A) and heterogeneous carbon distributions (B) in the GRO 95577 sample. The left BSE image is the overview image of one portion on the GRO 95577 sample with two areas (A and B) surrounded by white boxes. Two BSE images of the areas labeled A and B1 at a higher magnification. (A) Example of a large CMA with major phases labeled. (B) A region of the matrix next to a replaced chondrule. A small CMA is present in the lower right. (B2) RGB false-color image of the Calcium (red)-Magnesium (green)-Silicon (blue) X-ray maps. The dotted line in the false-color image helps show the boundary between the matrix (right two thirds of the image) and the altered chondrule (left one third of the image). (B3) Greyscale carbon X-ray map. B1–B3 share the scale bar in the lower right of Figure 6, and the other images have their own scale bars.

Figure 3.6 shows BSE images of morphologically typical CMAs found in GRO 95577. In Figure 3.6A, the magnetite grains are large (~ 5 µm) and clumped together. Surrounding the magnetite grains are calcite grains (grey in BSE with a smooth texture). The matrix (grey in BSE but with a rough texture) around the calcite and the magnetite contain diffuse HCPs (dark grey). There is a smaller CMA in the bottom left of Figure 3.6B. In Figure 3.6B2, the calcite grains appear as red and the magnetite grains appear black. A small amount of diffuse HCPs is visible in Figure 3.6B3 (brighter white than the calcite grains to their left) near the location of the CMA.

The MC in GRO 95577 is generally much lower in abundance in this sample than in the EET 92161 and QUE 99177 samples. The carbon abundance in the MC also varies depending on its location. In the high resolution carbon X-ray map in Figure 3.6B, there is a small but distinct gradient in carbon abundance across the matrix between the CMAs and the edge of the chondrule alteration rind. This could be due to either a depletion of the carbon in the matrix from the formation of calcite, or a preferential concentration of the carbon near the sides of the altered chondrule. Moving left from the white dotted line in Figure 3.6B, immediately inside the alteration rind of the chondrule, there is no detection of carbon in the mineral phases. There is a higher concentration of carbon farther left in an area where water may have intruded into the chondrule. In the top left corner, the carbon concentration sharply declines to zero at the sharp contact with a large mineral grain within the chondrule itself.

3.4.2 Raman Measurements

Single spot MMC spectra were obtained from each aqueously altered meteorite sample in ten polished locations and in twelve unpolished locations of the QUE 99177 chondrite. Sample sites were chosen randomly to insure that the resulting spectra would be representative of the bulk MMC composition for each sample. Ten spectra were taken from the polished sides to determine the effects, if any, polishing has on the Raman spectrum of MMC.

Raman spectral image data were collected on the polished surfaces of the EET 92161 and GRO 95577 samples. Spectra with calculated FWHM and band position values with 2σ uncertainties consistent with zero were discarded. Using this threshold for good spectra, ~ 16,000 spectra are left (~ 10,000 spectra in GRO 95577 and ~ 6,000 spectra in EET 92161) out of a total of ~ 68,000 spectra. To represent these data clearly, the dataset was split into 100 bins and then

59

shown as a 2-dimensional histogram in Figure 3.7 (Eilers and Geoman, 2004); colors represent the field of data points from each meteorite within 2σ of the mean. The mean is centered in the area of the highest frequency of data points within a bin (darker colors). Data points greater than 2σ from the mean are shown as small dots. Overlain on these 2D distributions are the Raman data from the polished (stars) and unpolished (white and black dots) spot spectra.

We see statistically significant differences between the Raman parameter data distributions for the two meteorites, but no differences in the Raman data from unpolished spots. There is some scatter in the spot data. For clarity, the analytical uncertainties are not shown for the spot data, but the scatter is consistent with the distribution of the Raman map data distributions. The statistical significance of the two distributions is assessed with a two-tailed multivariate statistical energy test (Aslan and Zech, 2005). The test shows that the two distributions have a statistically significant difference at a 95 % confidence level (p-value = 0). The difference between the distributions is easiest to see in Figure 3.7; of the six different calculated Raman parameters, band width and intensity ratios have the largest range of data and have the greatest difference between the two sample distributions.

In order to determine if these statistical results are meaningful, we need to know how much of this difference can be due to errors in fitting, changes in fluorescence background, and effects of polishing the sample. Changes in the background shape correlate with changes to the value reported by the Raman fit model; the maximum variation of a given Raman parameter depends on the fitting method that is used (Gasda and Ogliore, 2014). The maximum variation in I_D/I_G due to changes in fluorescence of the simulated spectra in Gasda and Ogliore (2014) is ~ 0.3 when using SGSD fitting and the typical fit error is ± 0.04. For D-band width, the maximum variation in the values is ~ 40 cm^{-1} and the typical fit error is ± 20 cm^{-1}. The difference between the two mean values GRO 95577 and EET 92161 is statistically significant; the standard errors are very small due to the very high number of data points in each distribution. However, the absolute difference between the two means is less than the maximum variation (i.e., < 0.3) in Figure 5 of Gasda and Ogliore (2014), so there is no meaningful difference in I_D/I_G between the distributions. In other words, the absolute differences in these distributions is less than the variation that we would expect is due to changes in the background fluorescence, so the change in I_D/I_G is not scientifically meaningful.
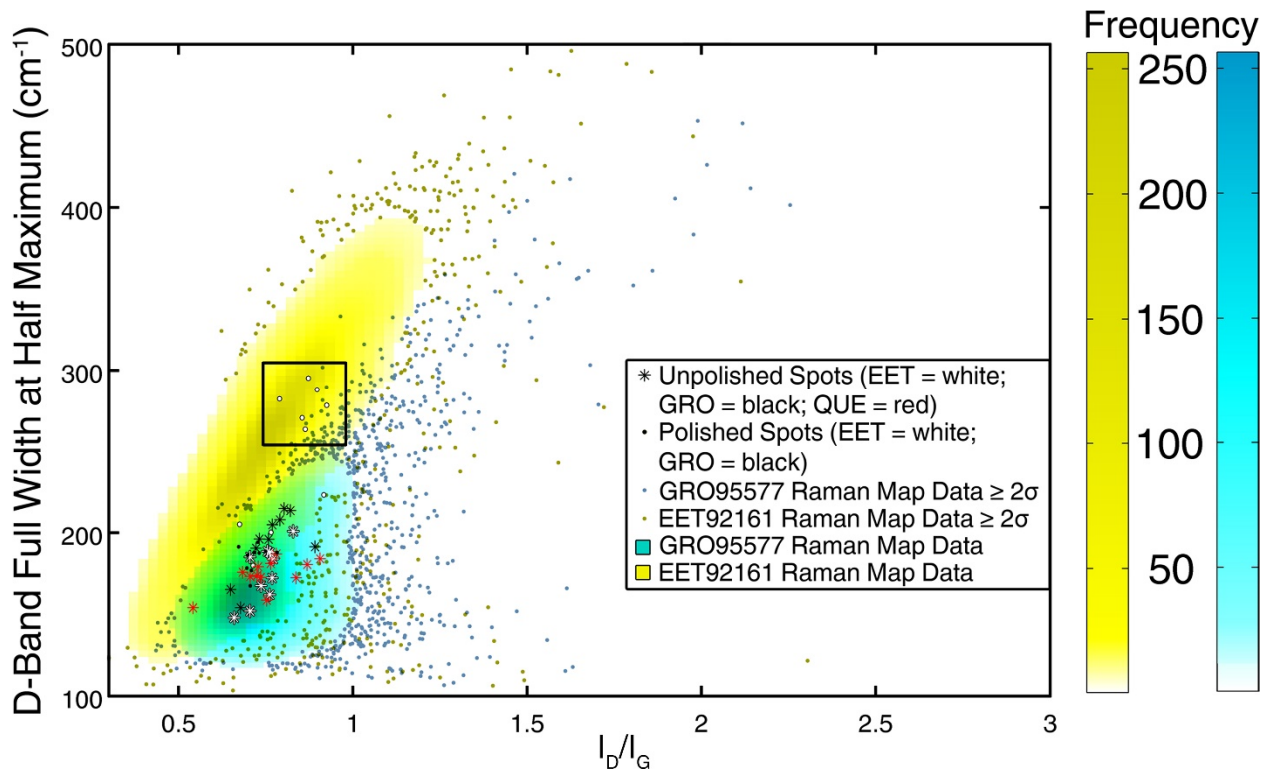
Figure 3.7: The above figure is a 100 × 100 bin 2D histogram where colors (blue for GRO 95577 and yellow for EET 92161) indicate the number of points within each bin. Results from Raman spot measurements of the polished and unpolished sides of the samples are overlain on the histograms. We plot the D-band Full Width at Half Maximum (FWHM) and D- to G-band intensity ratio because this graph shows the most variation among all the other Raman spectral features. A box highlights results from six polished spot spectra from EET 92161 that plot in the distribution for the EET 92161 map spectra.

The difference in D-band width is higher than 40 cm^{-1}; this difference is meaningful, but we suspect that this difference is due to sample polishing. All map data for GRO 95577 and EET 92161 were measured on polished surfaces. All unpolished spots and many polished spots for the samples fall into the GRO 95577 distribution. Six EET 92161 polished spot spectra plot inside the EET 92161 distribution (black box in Figure 3.7). These six spots have wider D-band widths and a shift in D-band position of 20–30 cm^{-1}. The difference between the widths of the peaks for the polished EET 92161 points is ~ 10 cm^{-1} for the G-band and ~ 100 cm^{-1} for the D-band. There is no significant change in G-band position. Interestingly, the polished-unpolished shift is not the same for all samples or spectra. There are detectable differences in band width and I_D/I_G for GRO 95577, but it is especially apparent in the EET 92161. It is not entirely clear why the EET 92161 MMC seems to be more susceptible to this change in band width and I_D/I_G. The pattern may be a more of a consequence of the particulars of the cutting and polishing process that occurred in the Meteorite Curation Lab such as different material properties of the two meteorites. GRO 95577 is cemented together as a result of aqueous alteration whereas the unaltered samples are more friable and loosely consolidated.

The micro-diamonds used to polish samples physically alter the surface of MMC. Given that the incident laser cannot penetrate far into the dark and light-absorbing MMC, the Raman spectrum of graphitic materials is extremely sensitive to the surface and the alteration thereof. The alteration can occur in two ways: the diamonds can cut larger MMC into small pieces, and the diamonds can introduce new or enhance already present defects. Either explanation is consistent because they both predict that I_D/I_G and D- and G-band width will increase as a consequence of increasing both edge and point-like defects in MMC.

3.4.3 Combined Raman and EPMA Carbon X-Ray Imaging

Figures 3.8 combines 12 Raman images (four Raman images in the first region of interest, two in the second, and six in the third)for the two areas of EET 92161 and one area of GRO 95577 with EPMA BSE images and X-ray maps. The leftmost images are the BSE image of the areas (henceforth referred to as regions of interest, or ROIs). Next to these images are Raman spectral images overlain onto the BSE images of the ROI. Each spectral image is square

and consists of at least 1600 spectra (40 × 40 pixels, one spectrum per pixel). If the spectrum had a detection of the Raman bands, and the 2σ uncertainties of the calculated Raman bands were not consistent with zero, then this was considered a 'detection,' and the pixel is filled in. Otherwise, the pixel is clear, corresponding to a non-detection of MMC in that particular pixel. Depending on the size of the image, the pixel size can be ~ 2–5 μm, though the laser spot size remains the same (~ 7 μm). To the right of the Raman detection images are the carbon Kα X-ray maps (white areas are high in carbon) of the ROI followed by the false-color calcium (blue), silicon (green), carbon (red) Kα X-Ray maps. In the false-color maps, calcite is seen as purple, and high carbon areas range from orange to red, depending on the concentration of carbon.

The first ROI is a thin matrix area sandwiched between two pyroxene chondrules in EET 92161. The chondrule on the left has a large Fe-Ni metal bleb. Along the right side and top half of the matrix area (dark grey in BSE), there are many terrestrial weathering veins (lighter grey because they are Fe-rich). Although there are detections of carbon in the terrestrial weathering veins, there are no D- or G-bands detected in the Raman spectra. The bottom central part of the matrix in this ROI is carbon-rich according to the carbon X-ray map, and it corresponds to a wide area of positive detections of D- and G-bands. The bright red areas in the bottom right of the ROI are pits in the sample that contain high amounts of diamond contamination.

The second ROI of the EET 92161 sample is in a brecciated section of the meteorite. There are small amounts of matrix surrounding small fractured chondrules in the center left part of the ROI. Numerous terrestrial weathering veins cross-cut the matrix and the clasts, and the terrestrial weathering products fill the cracks of the fractured chondrule. There are pits in the upper half of the matrix in this ROI that are filled with diamond contamination and some calcite that are likely formed by terrestrial weathering. Despite the contamination, we were able to collect two Raman maps in 'clean' parts of the matrix in this ROI that correspond to carbon-rich portions of the EPMA X-ray map. Additionally, there is a single yellow pixel in the false-color image in the matrix inside a sulfide grain in the bottom middle of the ROI that is SiC, as confirmed by energy dispersive spectrometry.

GRO95577 ROI 1 **EET92161 ROI 2** **EET92161 ROI 1**

Backscatter Electrons

Raman MMC Detection

D- and G-bands present in Raman Spectrum

Carbon X-Ray Map

C-Si-Ca X-Ray Map

Carbon
Silicon
Calcium

64
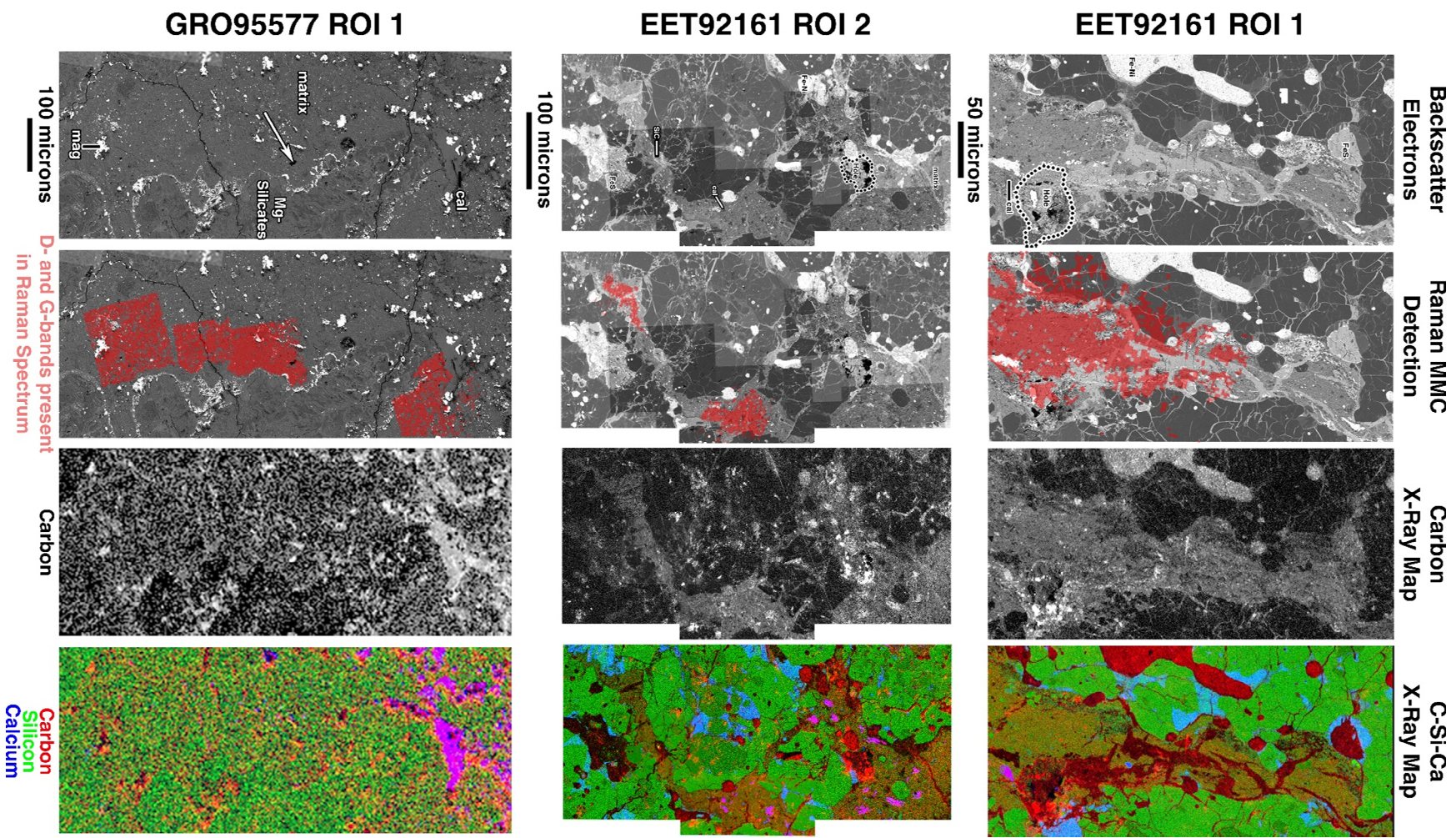
Figure 3.8 (previous page): An array of BSE and X-ray map images from the EET 92161 and GRO 95577 samples in the areas studied with Raman spectroscopy. Each of the rows has a different study area from a meteorite (labeled to the left of the row). Each column contains a different type of image (labeled above the top row). From left to right: BSE image of the Raman study area with the scale bar for each row directly below. BSE image of the Raman study area overlain with red pixels where the D-and G-bands were detected. Greyscale carbon EPMA X-ray map. False-color carbon (red), silicon (green), and calcium (blue) X-ray map image for the Raman study area.
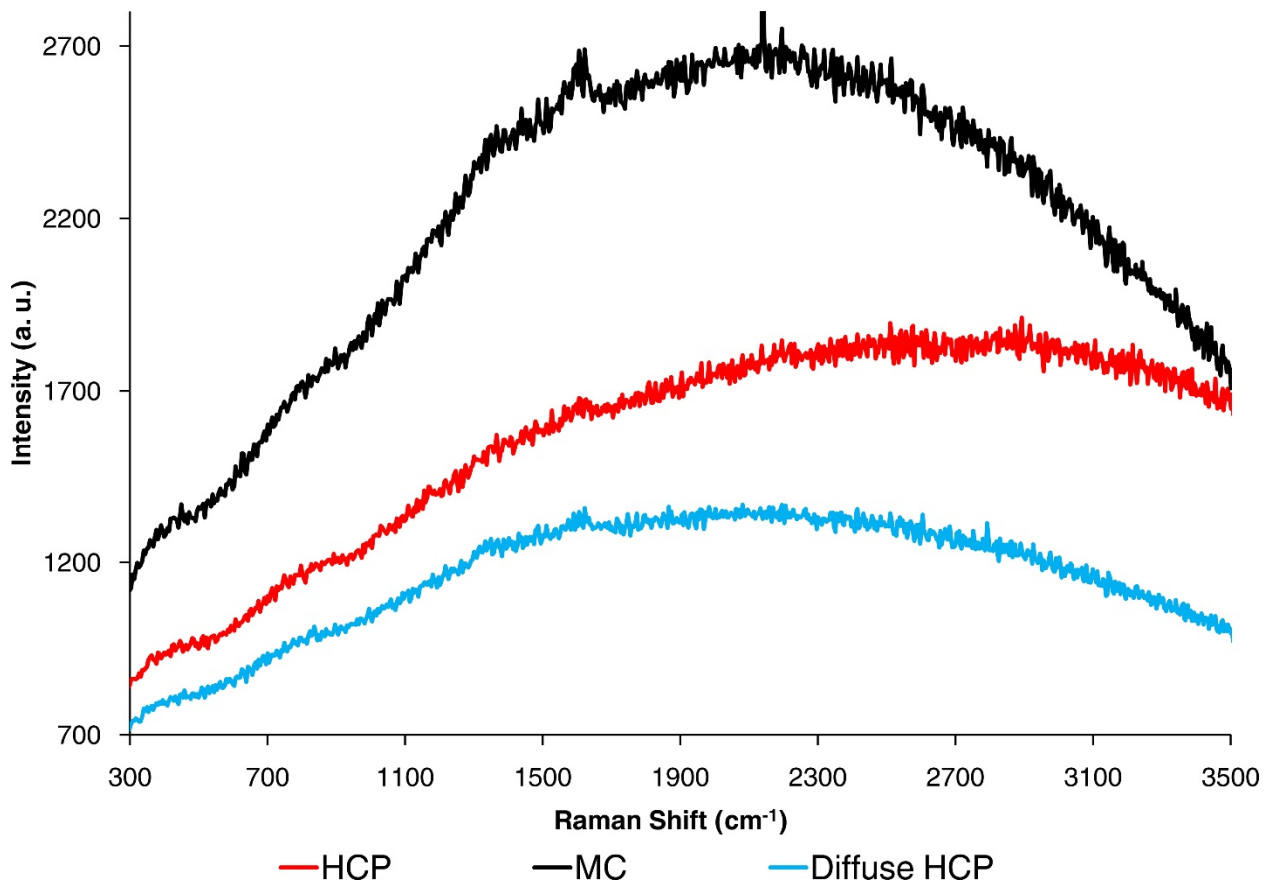
Figure 3.9: Typical Raman spectra of the MMC (MC, Matrix Carbon; HCP, High Carbon Phase) in GRO 95577.

The GRO 95577 ROI is a broad area of matrix near a group of aqueously altered chondrules (right side of ROI) and a small CMA (top part of the ROI). The D- and G-band detections in the Raman maps occur in the matrix areas of the ROI that contain carbon according to the carbon X-ray map. The Raman maps have sharp boundaries on the edges of the chondrules; no carbon is detected within these chondrules. The Raman map near the top of the ROI detects D- and G-bands right up to the boundary between the matrix and calcite in the top middle of the ROI. Separate Raman maps cover areas with HCPs; one diffuse HCP is next to a magnetite grain (labeled) in the bottom middle of the ROI, and a small lone HCP is near the middle of the ROI (labeled with arrow). None of the HCPs have detections of D- and G-bands in the Raman spectra.

The extensive evidence in Figure 3.8 confirms that detections of D- and G-bands (i.e., detections of MMC in the Raman spectrum) are almost exclusively confined to the carbon-rich matrix of the ROIs. Therefore, the matrix carbon is composed of (at least some) macromolecular carbon. However, there are a few features of the data that need to be addressed. First, there are some HCPs and diffuse HCPs inside the Raman ROIs. If our hypothesis is correct and HCPs are organic carbon, then one might expect intense D- and G-bands in their spectra. However, we only observe weak D- and G-bands in the diffuse HCP spectrum in Figure 3.9. Second, MMC is not detected in the weathering veins in spite of carbon being detected in the terrestrial weathering veins by EMPA. Third, there appear to be areas on the edges of the matrix, especially in the first EET 92161 ROI, that have detectable MMC in areas that are clearly chondrules in the BSE image. In contrast, the GRO 99577 sample contains chondrules in the Raman maps, but they have no detectable MMC in them. All three anomalous features can be explained by the difference between laser and electron beam penetration depths in these dark, heterogeneous samples.

The individual spectra from the maps need to be looked at more closely to understand why there are no detections of D- and G-bands in the HCP spectra. Figure 3.9 shows the typical raw spectra of MMC collected in a Raman spectral map. These spectra are collected with 15 s integration time. Spectra from the matrix (MC, black dots) have distinct D- and G-bands, while high carbon phases (HCPs, red and blue dots) have less distinct or no bands. The diffuse HCP spectra are likely that of MMC based on the visible peaks, but the peaks have a counter-

intuitively less intense signal despite a greater amount of material and the high Raman cross-section of MMC bands. Since MMC is opaque to visible light, the laser cannot penetrate by more than a few nm, so the amount of material that produces the Raman signal that the instrument measures is very small compared to a transparent material. Therefore, the HCP spectra will have very low intensity D- and G-band peaks, if any. When more transparent matrix materials (silicic materials) are mixed with the MMC, then more MMC surfaces can be sampled as the light scatters inside the sample (so diffuse HCP D- and G-bands should have greater intensity D- and G-bands than the large HCPs, but still low intensity overall compared with the MC spectra). The signal from the MMC will decrease only as the concentration approaches the detection limit of the instrument (a few vol%). Likewise, the signal from all Raman active species will decrease when more light absorbing or opaque materials are present (e.g., metal, metal oxides, and sulfides).

We can apply the above logic to the terrestrial weathering bands, which contain significant amounts of iron oxides. This is confirmed by looking at the Raman spectra of the weathering bands; there are peaks around 200, 550, 700, 1400, and 1650 cm^{-1} that are consistent with the minerals akagenite and ferrihydrite (Neff et al., 2006). Both of these minerals are products of the oxidation of iron metal in meteorites (Shah et al., 2004). Iron-rich materials are opaque and dark, so they tend to absorb the incident laser light so that the Raman scatterers in the sample do not interact with much incident light. Thus, the Raman scatterers produce a very weak Raman signal, if at all.

We detect MMC in the first EET 92161 ROI where the Raman map overlaps with the side of the chondrule on the left side of the matrix area. EPMA does not detect carbon in this area. Similar Raman maps in the GRO 95577 sample do not have MMC detections on the edge of chondrules. There is a plausible explanation for this problem. First, the sampling depth of the Raman laser is greater than the EPMA beam. The Raman laser, much like the electron beam, penetrates the sample, and the penetration depth is dependent of the confocality of the microscope (~ 50 μm) and how the sample absorbs light at the laser wavelength. In transparent samples, the practical signal (where the laser is focused the strongest) is limited to a depth of ~ 30 μm as long as the laser is perfectly focused on the surface of the sample. The EPMA beam does not penetrate into the sample as far as the Raman beam, especially since these samples are

coated with 25 nm of Al for electron microprobe analysis, which absorbs 20 % of the incoming electrons. The dense solid silicate phases, as opposed to the porous matrix material, absorb more electrons, so it is unlikely that the electron beam can penetrate 30 μm into a chondrule. Second, the alteration histories of the two samples play a role. The chondrules in GRO 95577 are primarily serpentine-class minerals, which are typically waxy and milky minerals instead of the translucent primary igneous materials, absorb most of the incoming laser light. The EET 92161 sample chondrules have nearly euhedral to subhedral pyroxene and olivine crystals (e.g., the chondrule in the center of Figure 3.4). The incident laser light may easily penetrate the mineral grains and scatter off the edge of the matrix that is below the chondrule. Thus, the translucent materials in EET 92161 allow the incident laser light to penetrate into the chondrule and scatter off the matrix materials that contain MMC that are up to 50 μm below the chondrule. The amount of matrix that is sampled by the Raman laser tapers off as the map gets away from the matrix due to the curvature of the chondrule beneath the surface.

3.4.4 Quantitative Measurements of the Matrix using EPMA

The goal of the quantitative EPMA work is to determine the distribution of organics in the matrix and the effects of aqueous alteration on the MMC. To do this, the dataset needs to be reduced in a logical way. The complication is that we can only measure C in the matrix with the electron probe, but if the carbon is organic, then H, N, and O are associated with it. We know that the C is organic because our measurements show that the carbon abundance distribution (mapped with the EPMA instrument) and the MMC distributions (mapped by Raman spectroscopy) match. So, we used published atomic H/C, N/C, and O/C ratios to determine the concentration of those elements in the matrix. If the totals from the calculation look reasonable (e.g., are distributed around 100 %), we accepted the analysis. If not, then we used a simple model to determine an atomic H/C ratio that is reasonable (more on that later). At the end of this iterative exercise, we will have the traditional element oxide weight percent values, along with calculated water and organic weight percent values. We compare those values with the literature results. For more information, the Appendix lists the procedure used for calculating the wt% oxides, show two example calculations, and then show the final results for each measurement.

Our data analysis also involves five assumptions. The first is that we have measured all the major elements in the matrix with concentrations greater than 1 wt%. The only major element we neglected to measure was Ni, which has oxide weight percent in the matrix of ~ 1.1 wt% (Ni/Si for EET 92161 fall Renazzo is 0.079) (McSween and Richardson, 1977). This is a fairly good assumption because all of the raw measurements have totals in the 80–90 % range, which is similar to the totals determined by McSween and Richardson (1977) for the matrix in Renazzo (EET 92161).

The second assumption is that the electron probe properly estimates the number of oxygens (neglecting C and S, which do not make solid oxides in these samples) that should be there based on stoichiometry. The oxides are assigned from this pool of oxygen atoms. Iron is partitioned slightly differently than what is typically done. First, sulfur is partitioned by assigning all of it to iron. This assumption seems reasonable because the Fe sulfides dominate the sulfur chemistry in the CRs, and Fe sulfides are still present in the GRO 95577 sample. The rest of the iron is partitioned as total iron oxide (FeO_T) in the EET 92161 and QUE 99177 samples and in GRO 95577 as magnetite (Fe_3O_4), which is a major phase of Fe in the matrix. Magnetite also serves as a representation that some of the iron is present as Fe^{2+} and some is present Fe^{3+} in Fe-bearing silicates in the matrix (e.g., fayalitic olivine and Fe-bearing phyllosilicates contain Fe^{2+} and Fe^{3+}, respectively).

The third assumption is that, ideally, the EPMA totals would add up to 100 % if all the light elements (N, O, and H) were measured. The fourth assumption is that any leftover oxygen atoms (form the oxygen atom pool determined by stoichiometry) not assigned to any phase are assigned hydrogen atoms to form water. In our model, we calculate water as H_2O. Calculating water as OH or H_2O makes little difference in the totals because the number of hydrogen atoms in water are an order of magnitude less than the hydrogen atoms in the organics.

The last assumption is that the carbon is organic. This is a good assumption because the Raman measurements of the matrix have an MMC signal. Multiple literature studies confirm that organics in the matrix are both soluble (small organic compounds) (Glavin et al., 2010; Elsila et al., 2012) and insoluble (large MMC compounds) (Sephton, 2002; Busemann et al., 2007). However, presolar carbide, diamond, or graphite may also be present. Based on the abundances of these species in the meteorites (~ 100 ppm or less) (Floss and Standermann, 2009; Nguyen et

al., 2010; Leitner et al., 2012) it is clear that they do not have a large effect on our calculations. The presence of calcite might be significant, especially in the GRO 95577 chondrite. We measured C wt% in calcite standards, and it is ~ 12 wt%. We discard measurements in GRO 95577 that have 12 wt% C in the matrix for the purposes of this calculation (also see caveat below). The remaining sample spots have low Ca abundance, which further confirms that calcite abundance in the matrix is low. In the raw dataset, only one measurement in 34 has elevated Ca abundance, so we suspect that the calcite abundance in the matrix in micro to nano-sized grain regime is < 5 wt%. Carbon concentrations in the other sample matrices are generally elevated, so it is much harder to determine what proportion is from calcite, though the calcite concentration in the matrix should be low to negligible in the less aqueously altered EET 92161 and QUE 99177 samples.

One important caveat remains. The quantitative EMPA measurements used the graphite standard to center the spectrometer on the carbon peak. The carbon Kα X-ray peak position for graphite is slightly shifted from the calcite carbon peak position. When the calcite grains were measured, both the calcite and graphite standards were used to center the spectrometers. Using the graphite peak position to measure the calcite standard, the raw C concentration decreases by ~ 2 wt%. So, concentrations of as little as 10 wt% could also be due to a major influence from calcite. There are many measurements in EET 92161 and QUE 99177 that are > 10 wt%. Hence, we need to assume that the calcite in the matrix is negligible in EET 92161 and QUE 99177 for this calculation. This assumption could be problematic if the measurements we make in QUE 99177 are in dark inclusions. GRO 95577 has generally low carbon abundance in the matrix, so we can assume any elevated carbon measurements are from calcite and remove these measurements from this calculation. The rest of the measurements we assume are calcite free for the purposes of the calculation.

3.4.5 Organic Carbon Modeling

Since we assume that the carbon we measure in EPMA is organic, then it should be possible to calculate the amount of H, N, and O that should be in the organic material, but cannot be measured directly. We could calculate the abundance of these species by tweaking the atomic H/C, O/C, and N/C ratios (starting from published values) until the EPMA totals are distributed

around 100 wt% after water is calculated. There are a number of published values for bulk IOM atomic ratios (Alexander et al., 2007; Cody and Alexander, 2005; Alexander et al., 2013). The major disadvantage of these measurements is that they were performed in situ, so we do not know what the atomic bulk matrix H/C, N/C, O/C ratios should be for each meteorite. For greater accuracy, we should obtain atomic bulk H/C, N/C, O/C matrix values. Unfortunately, these measurements are not available in the literature, so we use the most recent and complete atomic H/C, N/C, O/C dataset (Alexander et al., 2007) of demineralized IOM residues, which we are calling 'Endmember 1' (See Table 3.1). We ignore the atomic S/C values from Alexander et al. (2007) because the value is very low. For this dataset, GRO 95577, QUE 99177, and EET 92042 were measured. Since EET 92161 and EET 92042 are paired samples, we use the values from Alexander et al. (2007) for EET 92042 for our calculations.

In the first pass through the data using Endmember 1, the atomic H/C ratio is < 1 for all the samples. For the samples with high C content in the matrix (the EET 92161 and QUE 99177 samples), this endmember produces too many hydrogen atoms; all calculated totals are > 100 % after the amount of water is calculated. The totals for GRO 95577 are slightly < 100 %, close to the value we are aiming for. We considered two other endmembers: completely saturated carbon (C_nH_{2n+2}) and very low hydrogen (atomic H/C = 0.05). The saturated endmember created about twice as many hydrogen atoms as Endmember 1, which are too many hydrogen atoms for the GRO 95577 sample. The third endmember created too little hydrogen for all three samples, but the totals for the EET 92161 and QUE 99177 samples were much closer to 100 wt% than with any of the previous attempts.

Using the information from the endmembers, we made a simple model (Table 3.1) where we minimize the number of leftover atoms after water wt% is calculated by adjusting atomic H/C. We left atomic N/C and O/C constant for this simple model. One atomic H/C ratio is used for each sample. EET 92161 and QUE 99177 tend to have high carbon values, so these two samples work better with low atomic H/C ratios. GRO 95577 has low carbon but also higher original totals, so this sample tends to work well with an atomic H/C ratio close to 1. For QUE 99177 and EET 92161 samples, the average totals are within 0.1 wt% of 100 wt%, but there is significant spread. The standard deviation of QUE 99177 is ~ 1.8 wt% of the totals while the standard deviation of EET 92161 is ~ 2.9 wt% of the totals. This spread likely reflects some

heterogeneity of the matrix organic composition or some influence from calcite in the matrix. Further tweaking of the atomic H/C ratios gave us totals near 100 %, which are the 'Model Ratios' in Table 3.1.

A population of high carbon wt% measurements with high final totals results from the second pass through the data with the Model Ratios for atomic H/C (see Appendix Figure A.12). The high-C-abundance population seems to be different from most of the other GRO 95577 measurements because they have EET 92161- or QUE 99177-like values for the elements. To make the model simpler, we discarded these anomalous measurements, and calculated a revised GRO 95577 atomic H/C value of 1.45 ± 2.4 wt%. All the measurements are ± 5 wt% of 100 wt% (1σ errors). There are two outliers in EET 92161 with significantly higher totals, with these two values discarded, the new atomic H/C value is 0.135 ± ∼ 2.1%. These values are recorded in Table 1 as the 'Revised Model.' Using the revised model, we calculate the CHNO organics, water, sulfide, and oxide weight percent of the matrix in the CR chondrites. Two examples of the calculation are in the Appendix.

3.4.6 Checking the Model

We checked the reliability of the results by comparing them with the literature. First, the calculated water values are consistent with estimates of water in CRs calculated by different methods. Alexander et al. (2013) gives estimates of water as OH (EET 92161: 0.35 wt%; QUE 99177: 0.39 wt%; GRO 95577: 1.22 wt%). Our values are elevated by comparison (EET 92161: 0.55 wt%; QUE 99177: 2.19 wt%; GRO 95577: 1.46 wt%). The GRO 95577 and EET 92161 samples are both elevated by ∼ 0.2 wt% after taking the difference between H_2O, which was used in our calculation, and OH into account. This difference is small, and it shows how accurate results using this model can be compared to literature values. The elevated QUE 99177 water values may indicate that we sampled dark inclusions in this meteorite rather than normal matrix. Since both QUE 99177 and GRO 95577 have similar amounts of water, our study has essentially two data points for aqueous alteration, with QUE 99177 representing an intermediate level of alteration.

Table 3.1: Literature, endmember, and model values of atomic H/C, N/C, and O/C ratios in CR chondrites. All literature values for 'EET 92161' are from EET 92024 (paired with EET 92161 meteorite in this study).

	H/C	N/C	O/C
ENDMEMBER 1[a]			
QUE 99177	0.803	0.0365	0.146
EET 92161	0.757	0.0383	0.166
GRO 95577	0.756	0.0316	0.114
ENDMEMBER 2[b]			
QUE 99177	4		
EET 92161	4		
GRO 95577	4		
ENDMEMBER 3[c]			
QUE 99177	0.05	0.0365	0.146
EET 92161	0.05	0.0383	0.166
GRO 95577	0.756	0.0316	0.114
MODEL			
QUE 99177	0.275	0.0365	0.146
EET 92161	0.11	0.0383	0.166
GRO 95577	1.2	0.0316	0.114
REVISED MODEL			
QUE 99177	0.275	0.0365	0.146
EET 92161	0.135	0.0383	0.166
GRO 95577	1.45	0.0316	0.114

OTHER LITERATURE

	H/C	O/C
EET 92161[d]	0.78–1.18	30% C groups 1 oxygen
GRO 95577[e]	1	
EET 92161[e]		0.05

	C	H	N	O
CM[f]	100	48	1.8	12

[a]IOM residue bulk ratios (Alexander et al., 2007)

[b]Maximum number of hydrogen atoms (C_nH_{2n+2})

[c]Very low hydrogen

[d]NMR (Cody and Alexander, 2005)

[e]Alexander et al., 2013

[f]Pyrolysis of residues (Sephton, 2002)

Second, our oxide weight percent values are consistent with previous results (e.g., values for Renazzo in Table 1 from McSween and Richardson, 1977). Our Na_2O and Al_2O_3 measurements are lower by ~ 1 wt% (absolute) compared to Renazzo (McSween and Richardson, 1977), but that might reflect the different analytical treatment, improved mass attenuation coefficient corrections for the elements (which result in lower calculated abundances in our results), and differences between our EET 92161 meteorite and the Renazzo CR chondrite.

3.4.7 EPMA Results

Our revised model of atomic H/C, N/C, and O/C ratios are compared to values from the literature in Table 3.1. The atomic H/C value for GRO 95577 is relatively ~ 100 % higher than previous measurements and the atomic H/C values for EET 92161 and QUE 99177 are much smaller than previous measurements (Cody and Alexander, 2005; Alexander et al., 2007; 2010; 2013). The EET 92161 and QUE 99177 atomic H/C values are similar to those in CV, CO, and ordinary chondrites measured by Alexander et al. (2010). This discrepancy is likely due to measuring the carbon in situ rather than by demineralizing the samples.

These literature results all used demineralized samples, which could cause a loss in information that we can only see with in situ studies. For example, in the Alexander et al. (2010; 2007) papers, the C wt% of the IOM residues does not exceed 2 wt%, except for two samples. A rough calculation that assumes as much as 50 % matrix in the CR meteorites would indicate that the C abundance from demineralization is ~ 5 wt% at most. Our measurements show that the C wt% is at least 2 wt% and up to 15 wt% (and total organics from 5–25 wt%) in the matrix. Thus, demineralization must cause significant loss of MMC. The change in the atomic H/C ratios between these previous studies and ours suggest that demineralization changes the chemical structure of the organics as well, so perhaps our model (which uses the atomic O/C and N/C ratios from these previous papers) may need to be improved in future studies.

The geochemical plots in Figure 3.10 summarize the results of quantitative chemical analyses of the matrices of the three CR chondrites studied. All the plots in Figure 3.10 have MgO wt% on the x-axis and the other species wt% values on the y-axis. The data generally split into clusters, which correspond to each meteorite. Generally, with the exception of the Na_2O and

74

H$_2$O plots, there are trends with MgO in all of the plots from little or no aqueous alteration (EET 92161) to intermediate alteration (QUE 99177) to complete aqueous alteration (GRO 95577).

Note that QUE 99177 is classified as a CR3, but our measurements indicate an intermediate level of aqueous alteration. This result provide further evidence that some of the measurements done on QUE 99177 were in dark inclusions. The dark inclusion areas are only slightly altered; otherwise, the geochemical data would more closely match GRO 95577. Rather, the QUE 99177 dark inclusions are at an intermediate stage of alteration between the drier EET 92161 and completely aqueously altered GRO 95577. Water concentrations conspicuously do not fit with this narrative. Our data reduction techniques assume that QUE 99177 had a calcite-free matrix, and these geochemical data show that this assumption might not be correct. If some of the carbon in QUE 99177 is partitioned into carbonate, there would be a threefold decrease (relative to the carbon) of the remaining oxygen, decreasing the amount of calculated water by ~ 1.5 wt%. Judging by the Figure 10, the QUE 99177 matrix is consistent with dark inclusions being the dominate lithology in QUE 99177.

Terrestrial aqueous alteration trends in mafic materials (Nesbitt and Wilson, 1992) rely on an open system model, where fluids carry away soluble ions and concentrate residues of non-soluble components. Although meteorites are closed systems, there are locally open systems that behave in a similar manner to the terrestrial aqueous alteration models. For example, soluble ions in the matrix of the meteorite are carried out of the matrix and precipitate as separate large phases (e.g., CMAs). These phases are avoided in our EPMA measurements because they are not matrix. So the soluble species are essentially lost during alteration of the matrix, although the bulk meteorite abundances may remain the same. As expected, Figure 3.11 shows that the sum of the soluble ions (Ca, Na, and K) declines in abundance as they are dissolved in the aqueous fluid and are precipitated into new phases outside of the matrix (e.g., calcite). The sum of the Fe and Mg species remains approximately constant because Fe and Mg are leached and re-precipitated from the primary materials at roughly equal rates (Nesbitt and Wilson, 1992). Al$_2$O$_3$ increases, which is expected because Al$_2$O$_3$ is not soluble in the fluid, and so Al$_2$O$_3$ becomes concentrated as a residue and transformed into clay minerals.
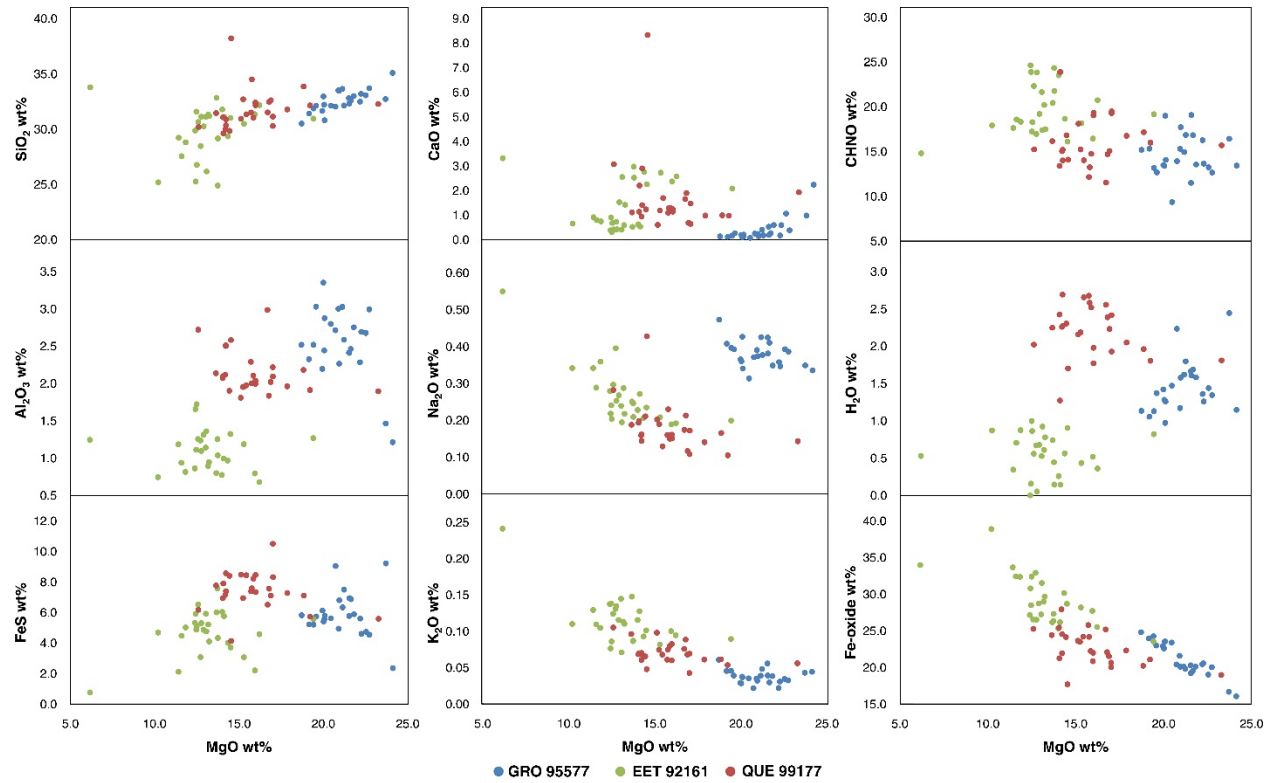
Figure 3.10: Oxide weight percent geochemical plots summarizing the results of the EPMA quantitative measurements of the matrices of the CR chondrites and the revised model calculation. The meteorite samples are represented by filled red (QUE 99177, CR3), green (EET 92161, CR2), and blue (GRO 95577, CR1) dots.
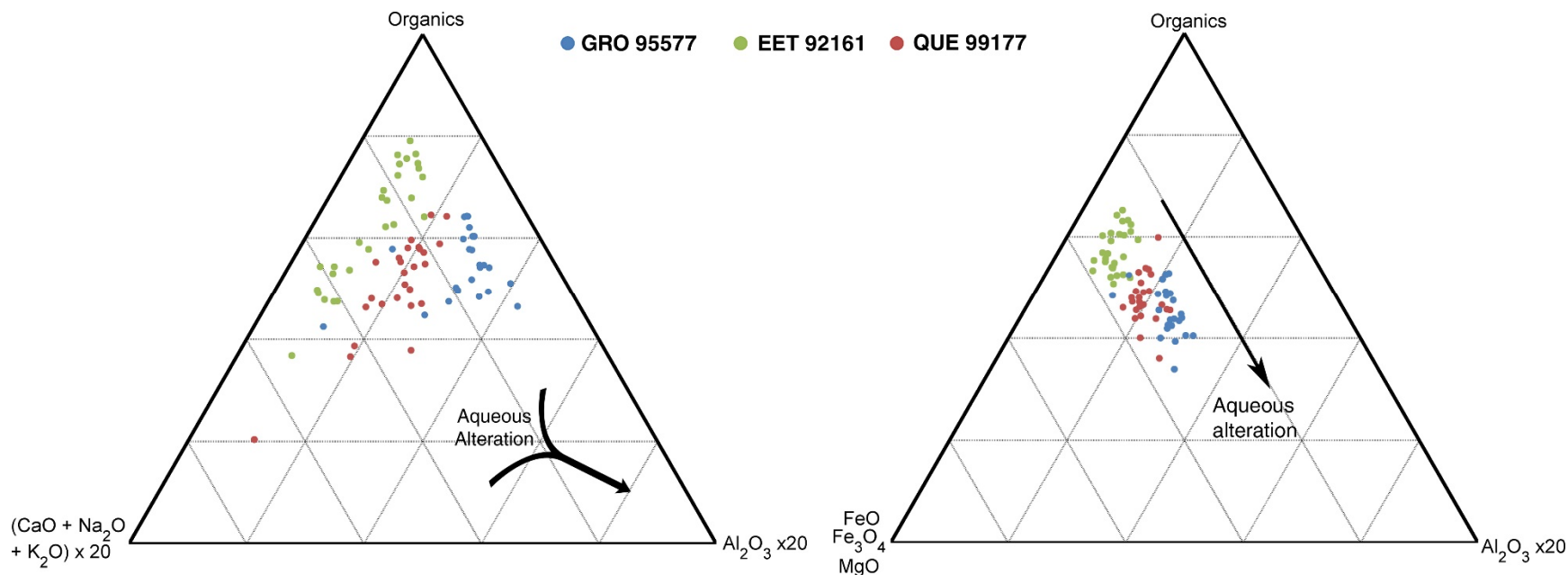
Figure 3.11: Mole fraction ternary diagrams that summarize the results of the EPMA quantitative measurements of the matrices of the CR chondrites and the revised model calculation. The 'Organics' label at the top vertex of each ternary plot, represents the calculated mole fraction of CHNO in each measurement. For clarity, the Al_2O_3 and $(CaO + Na_2O + K_2O)$ quantities are multiplied by 20 and the sum of the data is renormalized to 100.

Starting from an initial abundance of 15–20 wt%, according to Figure 3.10, Figure 3.11 shows that the organics decline in concentration with degree of aqueous alteration. It is possible that organics are destroyed by the production of calcite, which are abundant in the GRO 95577 sample. We also have evidence from EPMA carbon X-ray maps that the carbon content is lower near calcite phases (seen in Figure 3.3B and Figure 3.6B3 C Kα X-ray maps). Further work is needed to determine if calcite is a product of oxidation reactions involving the organics in the matrix. For example, the calcite carbon isotopic composition might be linked with the carbon isotopic ratio of the matrix organics (see Chapter 4).

3.4.8 Significance of the atomic H/C Ratios

The typical chemical formula for an organic molecule follows the equation C_nH_{2n+2} for completely saturated molecules and the atomic H/C ratio decreases as the molecule becomes more unsaturated. An unsaturated molecule like benzene has an atomic H/C ratio of one (C_6H_6). The only way to decrease the atomic H/C ratio below one is to make polyaromatic hydrocarbons (PAHs) by linking multiple benzene rings together ('fused' benzene rings). In PAHs, only the outside corner carbons have hydrogen atoms bonded to them, and the rest of the interior carbons have no hydrogen atoms bonded to them. For example, see Figure A.15.

For the QUE 99177 and EET 92161 MMC, the atomic H/C ratio is 0.775 and 0.135, respectively. In order to achieve these atomic H/C ratios in a molecule, there needs to be ~ 35 fused benzene rings in a sheet for QUE 99177 and about twice as many for EET 92161. A fused sheet would minimize the number of fused benzene rings needed, as opposed to a linear chain of fused rings which have a higher number of corner carbons. Let us assume for a moment that the GRO 95577 molecules are derived from EET 92161 and QUE 99177. We only need to break apart our large QUE 99177 molecule into smaller units of more saturated hydrocarbons with one benzene group to reproduce the atomic H/C ratio in GRO 95577. For example, an 11-carbon molecule with one benzene group and a branched saturated hydrocarbon side-chain has a formula of $C_{11}H_{16}$ and an atomic H/C ratio of 1.45. In reality, we need the hypothetical QUE 99177 MMC molecule to be a large in order for its decomposition products (the GRO 95577 MMC) to be large enough to express D- and G-bands in its spectrum. Small PAHs have sharp peaks near the D- and G-band positions that become broader and more MMC-like as the PAH

size increases (Shinohara et al., 1998; Castiglioni et al., 2000). Thus, the QUE 99177 MMC molecule will need to be large enough to accommodate this constraint. Following that logic, if the least aqueously altered EET 92161 MMC is the most primitive molecule, then the QUE 99177 organics are derived from it by splitting the EET 92161 molecule in half.

We know from previous studies that the macromolecular materials in meteorites have other chemical groups; this is how the N and O atoms are incorporated into the structure (Cody and Alexander, 2005; Remusat et al., 2005; Peeters et al., 2011; 2012a; 2012b). In order to incorporate these other groups into our hypothetical macromolecule, while preserving its atomic H/C ratio, we need to increase the number of internal carbons in the PAH group. Any group attached to the main PAH group will be less saturated than the PAH (any other organic group that is not another PAH will have an atomic H/C ratio ≥ 1), so interior carbons need to increase to compensate. Any carbon that gets replaced by an N or O in a ring structure must also be replaced somewhere else. Similarly, if one adds defects to the PAH structure (which might be expected since the Raman spectra detect strong D-bands), then the number of interior carbons decreases. To compensate, even more benzene rings must be added to the outside of the structure to keep the atomic H/C ratio below one.
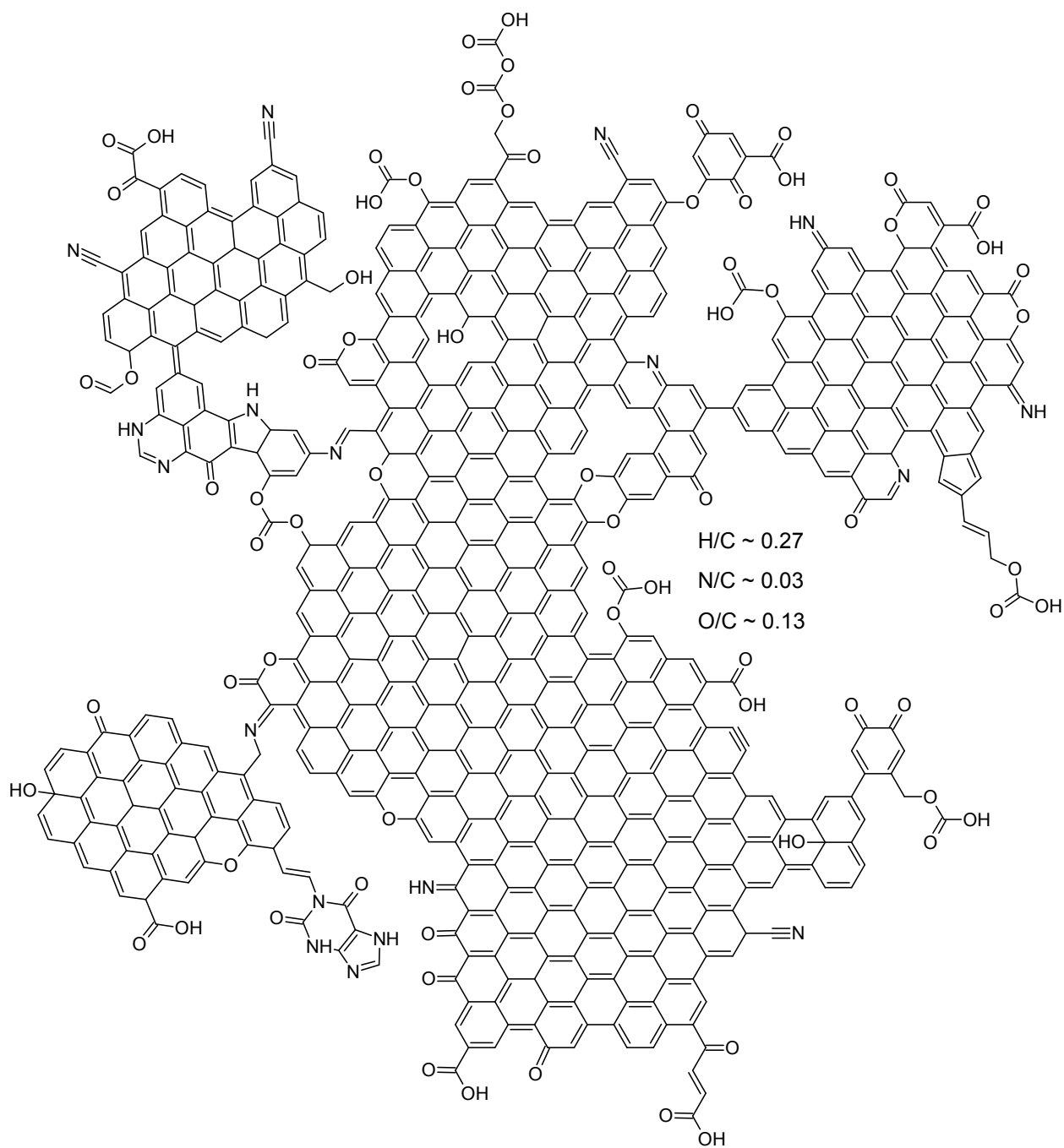
Figure 3.12: The hypothetical macromolecule that could exist using the Revised Model atomic H/C, N/C, and O/C ratios for QUE 99177 (Table 3.1). Side-chain chemistry reflects what is known from the results of C-XANES measurements of MMC residues (Cody and Alexander, 2005; Remusat et al., 2005; Peeters et al., 2011; 2012a; 2012b).

The resulting hypothetical molecule must be rather large. Figure 3.12 shows an example of such a macromolecule that fits the revised model for QUE 99177. The structure incorporates defects in the PAH structure and heteroatom containing side-chains. The molecule in Figure 3.12 is akin to the model of the carbonaceous material of the interstellar medium (ISM), suggesting that the ISM is a possible source of the MMC (see Figure 7 in Pendleton and Allamandola, 2002). Our model predicts that EET 92161 MMC must have even more interior carbons relative to the saturated side-chains. EET 92161 MMC then split in half at the onset of aqueous alteration to form the QUE 99177 MMC. The completely aqueously altered GRO 95577 MMC is either a decomposed product of the moderately aqueously altered QUE 99177 MMC (composed of mainly linear PAHs with some saturated side-chains) or the same size MMC molecule with very large side-chains of saturated hydrocarbon chains. Since we have already shown that the total carbon abundance decreases with aqueous alteration of the meteorite parent body and that the HCPs (which are likely concentrated MMC phases) change morphologically after aqueous alteration, we suggest that the GRO 95577 MMC is a decomposition product of the MMC in the less altered CRs. This can be tested with isotopic investigations because decomposition products of large molecules should retain the original carbon isotopic values (Grossman, 2002).

3.5 Aqueous Alteration of the MMC

We cannot distinguish between Raman MMC spectra in these three meteorite samples and there is no scientifically meaningful difference between the two Raman map distributions. However, there are physical changes to the distributions of MMC among the three samples, such as a decrease in abundance of MMC around calcite in the QUE 99177 and GRO 95577 samples and a change in the morphology in the HCPs from QUE 99177 (large HCPs) to GRO 95577 (diffuse HCPs). The physical differences seem to correlate with the extent of aqueous alteration (Figure 3.11). EPMA results imply that organics are destroyed by aqueous alteration. Modeling of the EMPA results suggest that there is a shift in H/C ratio from < 1 to > 1, implying the breakup of the internal MMC aromatic units. We tentatively conclude that the MMC can be altered by aqueous fluids, either by being suspended in or degraded by the aqueous fluid.

There are two main reasons why degradation could result in no detectable differences in the Raman spectra. Either the MMC is mechanically ground (similar to what occurs during polishing) when the MMC is suspended in solution and is moved along mineral grain boundaries, or the MMC is being chemically altered in a way that does not drastically change its Raman spectrum. Figure 3.7 shows clearly that, when the MMC is mechanically ground with diamond polish, the Raman spectra changed enough to detect a statistically significant difference between the polished and unpolished Raman spectra. Perhaps long-term grinding of the MMC with other minerals could achieve the same effect.

Chemical degradation of the MMC is possible so long as most of the internal aromatic structure of the MMC remains intact so that the Raman spectrum remains approximately the same. A mechanism to oxidize the MMC, which might involve an inefficient Fenton-like reaction (Walling, 1975), was mentioned previously by Cody and Alexander (2005). Fenton-like reactions has been shown to decompose PAHs (e.g., Kawahara et al., 1995; Lundstedt et al., 2006). A Fenton-like reaction, which produces OH (or other organic) radicals that react with the MMC on an iron catalyst, would also destroy the smaller organic compounds, producing CO_2 and H_2O. The destruction of the organic materials would lead to an overall decline in organics in the matrix, especially near areas with high amounts of iron catalyst material. The reaction occurs during aqueous alteration because it requires water. Oxidation of the organics produces CO_2, providing a source for calcite formation. This reaction mechanism might be a plausible explanation for the low MC abundance in the matrix near the magnetite grains in the GRO 95577 sample, where calcite grains are large and in high abundance.

There is other evidence in the literature that carbonaceous material can be altered by aqueous alteration. TEM and SIMS studies of the primitive QUE 99177 (QUE 99177) by Peeters et al. (2012a) have provided evidence of carbonaceous clumps, which might be the same as the HCPs we find in the same meteorite (but different samples). De Gregorio et al. (2013) classify nanoglobules found in demineralization residues of aqueously altered CR, CI, CO, and CM meteorites. Although it is unclear what connection there is between nanoglobules, MMC, and HCPs considering their size differences, De Gregorio et al. (2013) have shown that the morphology of MMC residues and the nanoglobules tends to change with aqueous alteration, with GRO 95577 having the most distinctly different nanoglobule morphology. The

82

nanoglobules and MMC should be affected by the same aqueous alteration on the meteorite parent body (though not necessarily in the same manner). Results from our study thus seem to agree that GRO 95577 has a distinctly different MMC morphology compared with the other CR chondrites. The De Gregorio et al. (2013) study is consistent with our first scenario wherein aqueous alteration mechanically alters MMC.

Another chemical alteration scenario that is less likely to occur would involve two (or more) competing processes. The first breaks apart and mobilizes MMC during the onset of aqueous alteration, and a second process re-polymerizes MMC, or forms new MMC from a small molecular precursor, such as when the fluid content decreases or becomes extremely basic during serpentine formation. The problem with this two-step process is that the Raman spectrum of the final product needs to be coincidentally very similar to the initial Raman spectrum. Additionally, there is less evidence from the literature to suggest that MMC can form on the parent body. There is a possibility that cold formamide can polymerize into macromolecular structures that are MMC-like under certain conditions (Cody et al., 2011; Kebukawa et al., 2013). However, the De Gregorio et al. (2013) study provides some evidence for formation of MMC on the CR parent body. They conclude, based on $\delta^{15}N$ results from the bulk MMC and individual nanoglobules that the nanoglobules in GRO 95577 may have formed on the parent body. Thus, a two-step formation scenario is plausible.

Isotopic studies of MMC are required to determine if any of these scenarios are correct. In the mechanical alteration case, the MMC should retain its primitive, possibly pre-solar, isotopic composition. In the second, MMC should contain some signature of the isotopic composition of the parent body as a result of alteration or formation (Elsila et al., 2012; Sephton and Gilmour, 2001). The De Gregorio et al. (2013) study is based on demineralized samples, and although demineralization should not change the isotopic signature of the carbonaceous materials, they have lost all spatial and petrologic information. We suggest that in situ isotopic analyses of samples characterized by petrologic and Raman measurements like the regions we identify as ROIs are essential to better understand how MMC has changed with aqueous alteration in the CR chondrites.

3.6 Summary and Conclusions

1. The distribution of macromolecular carbon has been mapped in the QUE 99177 grain mount and the EET 92161 and GRO 95577 meteorite samples. The Raman mapped macromolecular carbon distribution is consistent with the matrix carbon distribution mapped by electron probe microanalysis in the same locations. Therefore, the matrix carbon is the macromolecular carbon. Raman measurements of diffuse and normal high carbon phases are also consistent with macromolecular carbon.

2. There are statistically significant differences between the meteorites polished and unpolished single spot spectra as well as the distributions of the EET 92161 and GRO 95577 map spectra. Unfortunately, there is no scientifically meaningful difference between the two distributions due to changes in extent of aqueous alteration; rather the differences are due to changes in the fluorescence background.

3. Electron probe microanalysis mapping of carbon also reveals high carbon phases in QUE 99177 and diffuse high carbon phases in GRO 95577. The change in morphology suggests that the macromolecular carbon can be altered by aqueous alteration, either mechanically or chemically.

4. Calcite abundant in GRO 95577 and are present in QUE 99177 (suggesting that the areas that were probed by quantitative EPMA were dark inclusions). The abundance of the macromolecular carbon near the calcite grains is lower than in the rest of the matrix (matrix carbon, not high carbon phases). Calcite might be an alteration product of the reaction of the soluble organics with oxidizing radicals in a Fenton-like oxidation.

5. Modeling of the electron probe microanalysis results suggest that aqueous alteration changes the atomic H/C ratio of the macromolecular carbon from < 1 to > 1. Atomic H/C ratios of < 1 mean that there are a large number of internal carbons in the macromolecular carbon, making the molecule very large (Figure 3.12). If this very large molecule is broken up into smaller units, then the atomic H/C ratio increases. This could occur mechanically, chemically (Fenton-like oxidation is a possibility), or a combination of both.

Chapter 4

Isotopic Investigations of Carbon Bearing Phases in CR Chondrites GRO 95577 and QUE 99177

In preparation for publication in *Meteoritics and Planetary Science* as Gasda, P.J.; Thomen, A.; Nagashima, K. and Taylor, G.J., Isotopic Investigations of Carbon Bearing Phases in CR Chondrites GRO 95577 and QUE 99177.

4.1 Abstract

The source and mechanism of alteration of macromolecular carbon (MMC) materials in carbonaceous chondrites are open questions in cosmochemistry. The MMC could have been derived from materials formed in the interstellar medium, in the protosolar molecular cloud, within the solar nebula, or on chondrite parent bodies. Each of these space environments has a different isotopic signature, and these signatures make their mark on the MMC as it evolves and interacts in these environments. To address these questions, we performed in situ carbon and nitrogen isotopic measurements of the different carbon phases in two CR carbonaceous chondrites, GRO 95577 and QUE 99177. This study shows that the isotopic signature of the carbon phases in the matrix ('matrix carbon,' or MC) has $\delta^{13}C \approx -35$ ‰ and $\delta^{15}N \approx 160$ ‰, distinct from pure organic material we call 'high carbon phases' (HCPs) that have $\delta^{13}C \approx -25$ ‰ and $\delta^{15}N \approx 40$ ‰, relative to terrestrial values. We hypothesize that the MC isotopic signature, relative to other carbon phases previously measured in CRs, is a product of mixing soluble organic materials ($+\delta^{13}C$) and a 'missing' MMC phase ($-\delta^{13}C$). The HCPs seem to be distinctly different, perhaps related to cluster interstellar dust particles, and may be derived from organic carbon in the molecular cloud and ^{15}N enriched ices and organics. Alteration in the solar nebula could further enrich ^{15}N, but it is not necessary to produce the MC and HCP nitrogen isotopic signatures. Carbon isotopic measurements of calcite grains show that carbon becomes highly fractionated as the extent of aqueous alteration increases. We hypothesize that CO_2 is produced by oxidation of the organics, perhaps by a peroxide radical oxidation. Furthermore, the theoretically high $\delta^{13}C$ value for CO_2 ice in the solar nebula suggests that CO_2 ice cannot be the only source of the CO_2 that formed calcite on the CR parent body.

4.2 Introduction

Renazzo-type (CR) chondrites have three major carbon phases: macromolecular carbon, soluble organic carbon (SOC), and, in the aqueously altered samples, calcite. Macromolecular carbon (MMC), sometimes referred to as insoluble organic material (IOM), consist of kerogen-like molecules composed of large aromatic structures cross-linked with aliphatic organic groups

86

that usually contain heteroatoms (N, O, S, and P) (Cody and Alexander, 2005; Remusat et al., 2005; Peeters et al., 2011, 2012a, 2012b). The heteroatom to carbon ratio of the MMC is low (Alexander et al., 2007). SOC is comprised of small organic molecules. The number of carbons in the molecule, C#, is approximately ≤ 20, which means that the molecules are soluble in water or most organic solvents. The SOC includes amino acids (Glavin et al., 2011), nucleobases (Callahan et al., 2011), ketones, aldehydes, carboxylic acids (Sephton, 2002; Schmitt-Kopplin et al., 2010).

We build on our previous work (Gasda et al., 2014) by measuring the carbon and nitrogen isotopic ratios of the organics in situ. All three carbon phases exist as extremely fine grains in the matrix or dark inclusions of the CR chondrites, and the MMC and calcite exist as larger coherent phases. In Gasda et al. (2014), we devised a classification scheme of carbon bearing phases based on backscatter electron (BSE) images, electron microprobe analysis (EPMA) of carbon Kα X-rays, and Raman spectroscopic observations of the MMC in the samples. High Carbon Phases (HCPs) represent large coherent phases of MMC. The Queen Alexandra Range (QUE) 99177 sample has the largest HCPs (~ 10 μm). The Grosvenor Mountains (GRO) 99577 HCPs have a diffuse morphology and are usually made of small (< 1 μm) particles clumped together with interstitial fine-grained matrix. The diffuse HCPs are usually associated with calcite and magnetite assemblages abundant in the GRO 99577 sample. Calcite-magnetite assemblages vary in size and have large (1–10 μm) abundant grains of magnetite surrounded by calcite grains with matrix between the grains. Diffuse HCPs are embedded in the matrix touching the calcite and the magnetite grains. Matrix Carbon (MC) is observed in the matrix. The MC is likely to be a fine mixture of MMC, SOC, and calcite mixed with the fine grains of silicates, metal, and sulfides that comprise the matrix of the samples. Calcite in QUE 99177 are isolated, rare, and confined to the matrix. In both of the samples, calcite reside in areas of the matrix with a low abundance of MC.

The goal of the isotopic analyses is to determine if the refractory organic phases are resistant to aqueous alteration on the CR parent body. CR chondrites are an especially useful chondrite group to study in this regard: they experienced a low degree of heating and a large range in the extent of aqueous alteration on the CR parent body (pristine type 3 chondrites, intermediate type 2 chondrites, and completely altered type 1 chondrites) (Weisberg et al., 1993;

Weisberg, 1995; Brearley, 2006). The MMC has aliphatic chemical groups that may be released into, or undergo reactions with, the aqueous fluid during alteration. Therefore, determining the extent of alteration of the MMC is key to understanding the fate of organics in an abiotic system. The abiotic evolution of organic compounds in meteorite parent asteroids during aqueous alteration is akin to the reactions on the early Earth which produced chemistry suitable for life. Thus, studying pristine chondrites may help us understand the origin of life on Earth and if life is possible on other planets. We compare literature data on C and N isotopic fractionation trends with our in situ results from secondary ion mass spectrometry to determine if and how the MMC in our samples evolved with extent of aqueous alteration on the parent body.

4.2.1 Carbon and Nitrogen Isotopes and Fractionation Trends

The source of the MMC and its alteration by different space environments is highly debatable (Kerridge, 1999). The goal of many isotopic studies is to differentiate among different carbon sources based on their known endmember isotopic signatures and then track changes to the MMC using the known isotopic values of other isotopic reservoirs. It is possible that the MMC formed in any of the following environments: carbon-rich AGB stars (Kwok, 2004; 2009), the presolar molecular cloud (Sandford et al., 2001; Busemann et al., 2006), or the solar nebula (Flynn et al., 2003). Solar nebula alteration can occur via: irradiation of organic mantles on silicate dust grains (Nakamura-Messenger et al., 2006), irradiation of ices (Ciesla and Sandford, 2012), or polymerization of formaldehyde (Cody et al, 2011; Kebukawa et al., 2013). Astronomical observations of the interstellar medium (ISM) indicate the presence of organic materials that are similar to the MMC (Pendleton and Allamandola, 2002). Results from Gasda et al. (2014) suggest that the structure of the MMC is similar to the structure of carbon in the ISM estimated by Pendleton and Allamandola (2002). Some or all of the environments may have processed the MMC since its formation, leaving an isotopic signature (Kerridge, 1999). The isotopic signature may be altered during reactions, such as when MMC is exposed to electromagnetic radiation, collides with other molecules in space (which increases significantly in the cold and dense molecular cloud that preceded the formation of our Sun), or interacts with galactic cosmic rays (Ehrenfreund and Charnley, 2000; Tielens, 2005).

88

500

Bells
○

400

IDPs

CR   300

200

Renazzo ——   CR Amino Acids
○

100

Tagish Lake ——
○

CI ——   EL/EH

CM   CO

OC   CVred
CVox   -100

-200

-300

Inferred Sun, Jupiter   Solar Nebula
○

-400

Solar Wind

-500

CM, CI Individual Organics

-100   -50   50   100

δ^{15}N (‰)

δ^{13}C (‰)
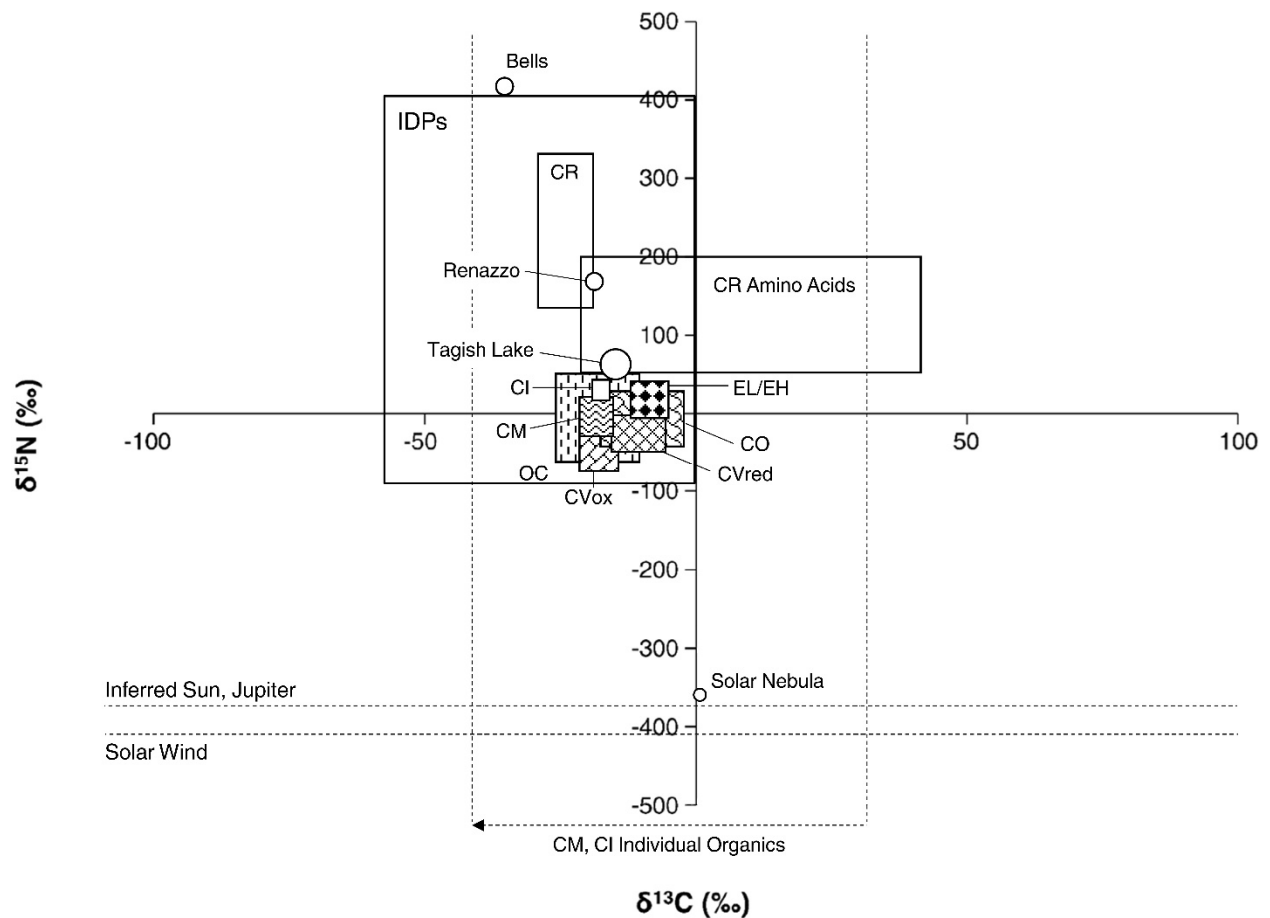
Figure 4.1: A compilation of δ^{13}C vs. δ^{15}N data from the literature for the different meteorite groups (Alexander et al., 1998, 2007, 2014), CR amino acids (Elsila et al., 2012), IDPs (Messenger, 2000), and the inferred solar nebula (Meibom et al., 2007). Only the range in δ^{13}C values are available for CM and CI individual organics (Sephton and Gilmour, 2001), and this range is represented by two vertical dashed lines. As the individual organic species increase in carbon number, the δ^{13}C value decreases, and this trend is represented by the dashed line arrow to the left. δ^{15}N values, inferred for the Sun from measurements of the Solar Wind (Marty et al., 2011) and Jupiter (Owen et al., 2001), are represented by the horizontal dashed lines.

89

The known $\delta^{13}C$ and $\delta^{15}N$ values (Eq. 4.1) for the different space environments mentioned above is shown in the plot in Figure 4.1. Data for the meteorite group fields are bulk acid insoluble IOM values (Alexander et al., 2007). Labeled individual falls, Bells (CM2) and Renazzo (CR2), are from stepped heating experiments of acid-insoluble organic material (Alexander et al., 1998). Tagish Lake values were determined by heating of the acid insoluble fraction (Alexander et al., 2014).

Other fields in Figure 4.1 include the CR amino acids (Elsila et al., 2012), CI and CM individual organics (Sephton and Gilmour, 2001), the solar nebula inferred from measurements of osbornite (Meibom et al., 2007), the solar wind (Marty et al., 2011), Jupiter (Owen et al., 2001), and cluster IDPs (Messenger, 2000). The study of individual organics in CI and CM chondrites by Sephton and Gilmour (2001) collected data only for carbon isotopes, so a set of dashed vertical lines shows the $\delta^{13}C$ range. The arrow to the left indicates that, as the C# increases, the $\delta^{13}C$ values decrease (Sephton and Gilmour, 2001). The study by Elsila et al. (2012) of the CR amino acids is consistent with the relationship between C# and $\delta^{13}C$ determined by Sephton and Gilmour (2001); the larger n-ω-amino acids tend to have the lowest $\delta^{13}C$ values. Isotopic studies of the solar system typically only report nitrogen isotopic values, so a set of horizontal dashed lines represents the $\delta^{15}N$ values. The solar nebula value is inferred from a study of grains of osbornite (TiN-TiC solid solution), inferred to be a refractory solar nebular condensate (Meibom et al., 2007), thus we believe it is a very precise $\delta^{13}C$ and $\delta^{15}N$ value for the solar nebula. The IDP field represents the range of values for secondary ion mass spectrometry measurements of most of the individual IDPs (Messenger, 2002).

Amino acids are a proxy for the other SOC molecules. The combination of the almost infinite number of organic side chains, core structure carbon chain length, stereocenter positions, and isomers mean that the amino acids can represent a very large number of organic chemical groups, formation pathways, and reaction conditions. Hence, we can use the detailed amino acid observations available in the literature as a benchmark for studying the SOC molecules in the matrix of our samples.

The only two meaningful sources for carbon to make carbonate are the organics or CO_2 ice. All other sources of carbon in the parent body (presolar grains, carbides, etc.) are not abundant enough (Floss and Standerman, 2009) to account for the large calcite grains found in

GRO 95577. From a chemistry standpoint, a molecule needs to be oxidized in a series of steps where the oxygen content of the molecule increases, in general. A molecule needs to be fully oxidized to decompose and produce CO_2. There are indications in the literature that C loss has occurred on aqueously altered meteorite parent bodies, indicating that CO_2 is produced (Cody and Alexander, 2005; Gasda et al., 2014). CO_2 ice formed at or beyond the CO_2 frost line in the solar nebula and thus the $\delta^{13}C$ value of the solar nebular CO_2 ice should be retained in comets (Mumma et al., 2003).

The measurement of Hale-Bopp comet (Jewitt et al., 1997) and the osbornite grain study (Meibom et al., 2007) may be inferred to be the $\delta^{13}C$ value for the CO_2 in the solar nebula. However, each of these studies has a problem with carbon fractionation. According to the Elsila et al. (2012) model, ^{13}C becomes concentrated in CO; the $^{13}C/^{12}C$ ratio becomes three to six times greater than other carbon reservoirs over the lifetime of the molecular cloud. Since CO_2 is derived from CO, and carbon isotopes in CO_2 have not been measured in a comet (Karen Meech, personal communication), we can only estimate that the $\delta^{13}C$ for Hale Bopp is three to six times 111 ± 12, the $^{12}C/^{13}C$ isotopic ratio of the HCN (Jewitt et al., 1997): ~ 2300–5700 ‰. Since measuring the carbon isotopes of CO and CO_2 is difficult (Wilson and Rood, 1994), and carbon and nitrogen isotopic data depends on the molecules measured, values for comet Hale-Bopp and the ISM are left off Figure 4.1.

Meibom et al., (2007) used carbon-bearing osbornite to infer the $\delta^{13}C$ and $\delta^{15}N$ for the solar nebula. Osbornite is a high temperature gas condensate. Thus, the carbon and nitrogen likely did not undergo significant fractionation as it condensed. It is not known if osbornite condensed from the CO/CO_2 reservoir (isotopically heavy C) or the organic reservoir (isotopically light C). If osbornite condensed from carbon from the CO/CO_2 reservoir, it would suggest that the CO_2 ice has approximately the same $\delta^{13}C$ value as the osbornite. If the osbornite condensed from carbon that originated in the organics reservoir, then the $\delta^{13}C$ in CO_2 in the solar nebula (from which the ice formed) can only be calculated theoretically (e.g., the Hale-Bopp example). In that case, the osbornite and the Hale-Bopp CO_2 ice $\delta^{13}C$ values would roughly agree, albeit largely theoretically. Additionally, the osbornite carbon could be formed by mixing the isotopically light organic carbon and the isotopically heavy CO_2 in the nebula. Hopefully, the

Rosetta mission will determine the $\delta^{13}C$ value for CO_2 ice in comet 67P/Churyumov-Gerasimenko and resolve this issue (Balsiger et al., 2007).

Further carbon fractionation occurs during aqueous alteration on the meteorite parent body where CO_2 gas is produced, dissolved in the alteration fluids, and calcite formed. Generally, kinetic fractionation dominates the fractionation of carbon for irreversible processes and equilibrium fractionation occurs in thermodynamically controlled systems (Grossman, 2002 and references therein). Since the $^{12}C–^{12}C$ bond is slightly weaker than the $^{12}C–^{13}C$ bond and the $^{13}C–^{13}C$ bond is the strongest of the three, the isotopically light bonds will be preferentially broken (all other variables being equal), but the energy differences are so small that fractionation will only occur in low temperature regimes (Grossman, 2002 and references therein). This may be an oversimplification because in organic chemistry all C–C bonds are not equal and the bonds will break depending on their bond energies, and whether or not the reaction is thermodynamically favorable.

It is more likely that the production of the CO_2 by oxidation of organics is a stochastic process and will not necessarily exhibit any fractionation at all, especially for reactions involving macromolecules (Grossman, 2002 and references therein). The heavier CO_2 molecule is slightly less soluble than the light molecules, and the solubility of the three species weakly depends on temperature and pH (Vogel et al., 1970; Mook et al., 1974; Lesniak and Sakai, 1989; Romanek et al., 1992; Zhang et al., 1995). The fractionation due to dissolution is overshadowed by the larger fractionation that occurs with the formation of calcite. The heavier dissolved inorganic species (DIC) are preferentially crystallized into calcite. The overall $CO_{2(g)}$-DIC-calcite system, which tends to incorporate the heavier carbon isotope into the calcite (the small dissolution preference toward the light isotope is outweighed by the formation of calcite) and this is weakly temperature and pH dependent. The enrichment factor for $\delta^{13}C$ is ~ 6–7 ‰ at 50°C and up to ~ 10 ‰ at 20 °C (Emrich et al., 1970; Romanek et al, 1992). Larger fractionations can only occur with Rayleigh distillation (Grossman, 2002 and references therein), which can occur if CO_2 escaped from the parent body (Alexander et al., 2013).

According to models, nitrogen also becomes fractionated in the presolar molecular cloud (Terzieva and Herbst, 2000; Elsila et al., 2012). HCN, NH_3, and N_2 can become highly enriched in ^{15}N while atomic N will be depleted in ^{15}N (Charnley and Rodgers, 2002; 2008). It seems that

the solar nebula condensates (Figure 4.1) formed from this depleted ^{15}N reservoir. Nitrogen fractionation during phase changes in the solar nebula and on meteorite parent bodies should also be dominated by kinetic fractionation in a similar way to carbon isotopic fractionation.

Other possible fractionations of carbon and nitrogen isotopes can occur in the solar nebula by the self-shielding and photodissociation processes. Self-shielding of CO and N_2 would produce enrichments of the heavy isotopes of C, N, and O in the early solar system (Lyons and Young, 2005; Lyons et al., 2009; Visser et al., 2009; Lyons, 2010a, 2010b). Photodissociation of CO can fractionate the heavy isotopes of oxygen and, by extension, carbon by splitting the molecule and trapping the heavy isotopes in water and organic molecules (Chakraborty et al., 2008; Lyons et al., 2009). Heavy N_2 is also prone to photodissociation, and massive fractionation can occur if the dissociation products can be quickly trapped into ices or organic molecules (Chakraborty et al., 2014). If self-shielding does occur, it must be efficient enough to allow MMC formation or alteration within the lifetime of the disk where we are limited to timescales between 10^5 yr, the lifetime of the protosun (Lyons and Young, 2005), to ~ 3–5 Myr, the formation of the chondrite parent bodies (Baker et al., 2005).

4.3 Methods

Two samples of CR chondrites were chosen for this study based on our previous measurements (Gasda et al., 2014) and their suitability for SIMS work. Antarctic meteorites GRO 95577 and QUE 99177 were provided by the Johnson Space Center Meteorite Curation Laboratory as a chip with one polished side and as a chunk, respectively. Both samples are free of fusion crust. To limit sample exposure to terrestrial carbon contamination, neither sample was impregnated with epoxy nor was the GRO 95577 sample cut with oils or water. GRO 95577 has been polished with diamonds and washed once with 95 % ethanol. The QUE 99177 sample also studied by Gasda et al. (2014) is very friable and it could not be cut or polished.

We mounted the two samples separately. GRO 95577 is in a 1" round indium metal slug (99.999%, Indium Corp.) while dust grains extracted from a large chunk of QUE 99177 are pressed onto gold foil (99.999%, EPSI Metals, annealed) mount. Both samples were simultaneously coated with 25 nm aluminum metal (99.99%, Lesker) using a Torr International

metal coater using a FTM-2000 thickness sensor. The GRO 95577 sample was masked with copper foil to smooth out the indium surface near the edge of the sample and ensure uniform ion extraction in the SIMS. The QUE 99177 mount was added to a 1" round sample holder that also held the standards used in the measurement. The in-house calcite standard (see below) is mounted conventionally in epoxy with carbon coating. The kerogen standard and the QUE 99177 sample are mounted in a similar fashion, but the standard is gold coated. BSE images were collected using the JEOL JXA-8500F field emission gun electron probe microanalysis instrument at the University of Hawaiʻi, Mānoa.

The in situ isotopic work was performed at the University of Hawaiʻi at Mānoa W. M. Keck Cosmochemistry Laboratory using the Cameca SIMS 1280 Secondary Ion Mass Spectrometer (SIMS). A 3 pA or less Cs^+ primary beam was focused to ~ 1–2 μm and rastered over ~ 3 × 3 μm. The secondary ions were measured in monocollection mode using the axial electron multiplier. Each measurement had a 300 s pre-sputtering time at 300 pA, 30 cycles per measurement, measuring masses (time in s): $^{12}C^-$ (2), $^{13}C^-$ (15), $^{12}CH^-$ (1), $^{18}O^-$ (1), $^{12}C^{14}N^-$ (2), $^{12}C^{15}N^-$ (30), $^{28}Si^-$ (1). A mass resolving power of ~ 7150 was used to separate the masses of $^{12}C^{15}N^-$ and $^{12}C^{14}N^-$ from interferences such as BO^- and $^{13}C_2^-$, respectively. A normal incident electron gun was used for charge compensation. All measurements were performed during one week in April 2014 except for later measurements of calcite grains in QUE 99177 which were performed in June 2014. Later measurements have ~ 5 μm spot size due to a slightly higher primary beam current. Nitrogen isotope ratios were determined by dividing $^{12}C^{15}N$ by $^{12}C^{14}N$ values. Standards are measured daily before and after each block of measurements. Data were reduced using time interpolation and electron multiplier dead time correction (31 ns). Ratios of the total counts are reported. Total count ratios are less biased than the mean of the measured ratios (Ogliore et al., 2011).

The carbon and nitrogen isotope compositions (i.e., $\delta^{13}C$ and $\delta^{15}N$) are reported in delta-notation in units of per mil (‰) using Equation 4.1.

$$\delta = \left(\frac{R_m}{R_{std}} - 1\right) \times 1000 \qquad (4.1)$$

R_m is the measured ratio (i.e., $^{13}C/^{12}C$ and $^{12}C^{15}N/^{12}C^{14}N$), and R_{std} is the standard ratio value. Terrestrial carbon (Pee Dee Belemenite or PDB, $^{13}C/^{12}C = 0.0112372$) and nitrogen standard

94

(Earth atmosphere, $^{15}N/^{14}N = 0.003676471$) were used to calculate delta values. SIMS instrumental mass fractionation (IMF) is corrected using measurements of Kerogen III IFP 166286 ($\delta^{13}C = -25.00 \pm 0.11$ ‰, $\delta^{15}N = 3.71 \pm 0.16$ ‰), provided by the French Institute for Petroleum. Carbon isotope composition of calcite was corrected with UWC-1 standard ($\delta^{13}C = -2.03$ ‰, provided by the University of Wisconsin, Madison, Ferry et al., 2010). The IMF for the kerogen standard is $\delta^{13}C = -21 \pm 5$ ‰ and $\delta^{15}N = -8 \pm 7$ ‰, and the IMF for the calcite standard is $\delta^{13}C = -37 \pm 18$ ‰ during the first set of experiments and is $\delta^{13}C = -37 \pm 8$ ‰ during the second set of calcite measurements. The reported 2σ uncertainty includes internal precision of individual measurement and reproducibility of standard measurements.

Type III kerogen is an aromatic kerogen (atomic H/C < 1) that is similar to the structure of the MMC in chondrites (Aléon et al., 2003) and has a similar structure and atomic H/C that we predicted in our earlier paper (Table 1 in Gasda et al., 2014). Gasda et al. (2014) predicts that atomic H/C for the QUE 99177 and GRO 95577 samples are not the same (QUE 99177 atomic H/C < 1 and GRO 95577 atomic H/C > 1), but the systematic IMF correction for differences in atomic H/C of the sample compared with the kerogen standard is ≤ 5 ‰ (Sangély et al., 2005), within the measurement errors. IMF error is 5 ‰ for carbon, the ambiguity of the systematic error due to the atomic H/C difference is about 5 ‰, and the measurement error range is typically ~ 10 ‰. Thus, we cannot discuss differences in averages ≤ 10 ‰ for carbon.

On the other hand, no literature is available that discusses the systematic IMF trends for nitrogen in organics and its relation to atomic H/C. Error in the nitrogen measurements is small (~ 20 ‰), compared with the range $\delta^{15}N$ values (~ 0–250 ‰). The IMF correction is small, and the 2σ error is almost consistent with zero. Thus, changes in nitrogen ≥ 20 ‰ are significant.

4.4 Results and Discussion

4.4.1 Description of the sample areas

The samples have been described in detail in the literature (e.g., Weisberg and Prinz, 2000; Perronnet and Zolensky, 2006; Weisberg and Huber, 2007; Abreu, 2007; Abreu and Brearley, 2010) and our sections of the meteorites were also briefly described by Gasda et al., (2014). Ample evidence (e.g., geochemical trends, the presence of calcite grains) suggest dark

inclusions dominate the matrix in our sample of QUE 99177 (CR3), and it is inferred from geochemical trends that these dark inclusions represent an intermediate stage of aqueous alteration (Gasda et al. 2014). Additionally, GRO 95577 shows vast petrographic and geochemical evidence for complete aqueous alteration; all of the primary phases have been replaced by secondary minerals in place.

In QUE 99177, four HCP, eight matrix, and four calcite spots were successfully measured using the SIMS. Figure 4.2 contains backscatter electron (BSE) images of the different sample spots in QUE 99177. Figure 4.2A–C show the three different large HCPs measured. The first HCP is the largest and had room for two spot measurements. Although the QUE 99177 sample was damaged during the mounting process, some petrographic relationships can still be seen. HCPs are found in the matrix or at the edge of the matrix, as seen in Figure 4.2A. Figures 4.2D–E show the two matrix areas that were sampled. Suitable areas were picked using C Kα X-ray maps of the dust grain that contains both the HCP in Figure 4.2A and the calcite grains (Gasda et al., 2014). Suitability is based on uniformity of the BSE image (no small grains of other materials should be present in the beam spot); matrix areas to be sampled were chosen because they are typical. The sampled calcite grains are shown in Figure 4.2F. The matrix surrounding the calcite grains has a lower carbon abundance than typical matrix.

For GRO 95577, five diffuse HCP and calcite spots were measured along with six matrix areas. Figure 4.3 contains the BSE images that show the SIMS spots locations. The calcite and diffuse HCP spots are all sampled in a relatively large calcite-magnetite assemblage shown in Figure 4.3A. In the BSE image of the calcite-magnetite assemblage, magnetite grains are white, and they are surrounded by dark grey calcite grains rimmed with the darker diffuse HCPs. At this magnification some of the individual grains, and their large size range, of the diffuse HCPs can be seen. Figure 4.3B shows a high resolution BSE image of an area of the matrix between the rim of a chondrule and a small calcite-magnetite assemblage. The C Kα X-ray map (Figure 4.3B2) of this region reveals a gradient of carbon abundance decreasing towards the calcite-magnetite assemblage (Gasda et al., 2014). Four matrix spots were sampled in this image, three in a high C area and one in the low C area. Two other matrix spots are shown in Figure 4.3C in an area that was previously Raman mapped (Gasda et al., 2014).

4.4.2 Isotopic Analyses

Figure 4.4 shows a plot of the data for QUE 99177 and GRO 95577 with 2σ error bars. Table 4.1 lists these values. The data split into two clusters, one with significantly higher $\delta^{15}N$ than the other. Both clusters are depleted in ^{13}C. The ^{15}N enriched cluster is almost entirely composed of MC and the lower cluster is composed of HCP measurements. One GRO 95577 diffuse HCP measurement plots in the upper cluster. Before and after BSE images confirm that the diffuse HCP is very thin and the primary beam sampled matrix beneath the diffuse HCP, which explains this anomalous measurement. The uncertainties in the measurements are small enough that an individual measurement is usually resolved from the rest of the points in the cluster. This indicates that there is considerable heterogeneity in the isotopic values. This is especially true for the upper (MC) cluster. The HCPs are more tightly clustered together, indicating that these phases are more uniform in isotopic composition despite their lack of spatial similarity (Figure 4.2, left).

If there is a change due to alteration from the dark inclusions in QUE 99177 and the completely altered GRO 95577 chondrite, it is very subtle. The GRO 99577 diffuse HCPs have a slightly elevated $\delta^{15}N$ due to MC physically mixing with the HCPs (Figure 4.3). Thus, the elevated $\delta^{15}N$ is likely not due to chemical changes in the HCP and MMC. The range in $\delta^{15}N$ of the GRO 95577 matrix is significantly narrower (136–178 ‰) compared with the QUE 99177 matrix (125–229 ‰). The narrowing of the $\delta^{15}N$ range could be due to aqueous alteration. If the nitrogen-bearing molecular groups on the MMC or stand-alone molecules are labile and soluble in the alteration fluids, alteration might be homogenizing or equilibrating the nitrogen isotopic reservoirs in the parent body, leading to a tighter cluster of values. The $\delta^{13}C$ values are shifted slightly higher, but the shift is not significant compared with the error. A shift in carbon isotopes might merely be due to mixing with calcite in the matrix, although the amount of calcite in the matrix is likely to be $\ll 10\%$ based on its calcium content (Gasda et al., 2014). There is no difference in the $\delta^{15}N$ nor the $\delta^{13}C$ values due to proximity of a measurement to calcite-magnetite assemblages, where lower abundance of carbon is measured in the matrix (Gasda et al., 2014). The lack of a large systematic shift in the MC to a lighter isotopic composition suggests that, if the organic materials in the matrix broke down during aqueous alteration, there is no evidence that this reaction fractionated the carbon or nitrogen isotopes.

Figure 4.5 shows the same data as Figure 4.4 with a weighted least squares fit (with 2σ uncertainty dotted lines). The weighted-fit line is not a fractionation line, which would have a positive slope (Grossman, 2002). If the weighted line is extrapolated down to low $\delta^{15}N$ values, it nearly passes through the solar nebula value, which may or may not be significant. One could draw similar lines through the Alexander et al. (1998; 2007) data that pass through the solar nebula value. The weighted line shows that our results do not agree with published results for IOM in CRs (Alexander et al., 2007). These previous results are for the acid insoluble residue (the IOM) of the meteorites rather than a bulk matrix value which we obtained. We suggest that the higher cluster (the MC cluster) represents a mixed phase.

The MC cluster could be a mix of 70–90 % MMC and 10–30 % SOC. The SOC, which is represented by the CR amino acids box in Figure 4.5, is enriched in ^{13}C. As C# (the number of carbons in the molecule) increases, $\delta^{13}C$ decreases inside this box. Light SOC molecules have high $\delta^{13}C$ (> 0 ‰) values. Additionally, the Elsila et al. (2012) results agree with those of Sephton and Gilmour (2001) (CM, CI individual organics have decreasing $\delta^{13}C$ with increasing C#). If the MMC is the IOM studied by Alexander et al. (2007), then the MC cluster should lie between the IOM and the CR amino acids boxes, or essentially where the Renazzo chondrite plots in Figure 4.5. If the HCPs represent the pure endmember of the MMC, then it should lie on the mixing line between the MC values and the CR amino acids field. However, the HCPs do not lie on a mixing line. Our data for HCPs plot to the left of the CR IOM box (lower $\delta^{13}C$ than the IOM) and to the upper left of the HCP cluster. There is no way to draw mixing lines or curves that would mix either the HCPs or the IOM endmembers with the amino acid endmember to produce the mixed matrix isotopic values.

Therefore, there must be a 'missing' endmember with lower $\delta^{13}C$ values and slightly higher $\delta^{15}N$ values. The missing endmember would mix with the amino acids endmember to produce the MC cluster in Figure 4.5. We predict that the missing phase is MMC because it would likely have a high C# in order to have a low $\delta^{13}C$ value. If it is in low abundance (unlikely since MMC was detected with Raman spectroscopy by Gasda et al., 2014), it would have even lower $\delta^{13}C$ values. It is more likely that the MMC has a fairly high concentration relative to CR amino acids or SOC. Thus, the MMC should have values in the $\delta^{13}C \approx -50$ to -75 ‰ range and $\delta^{15}N \approx 100$ to 300 ‰ range.
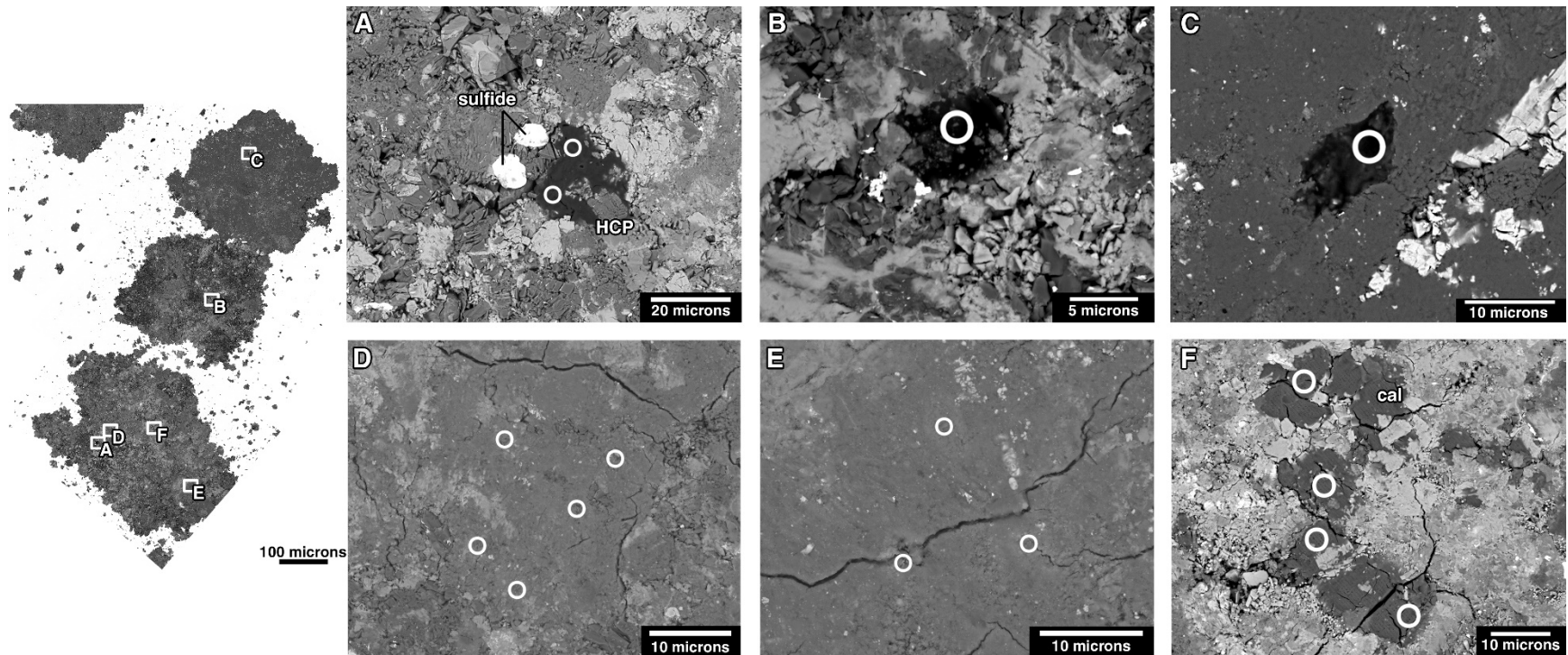
Figure 4.2 (previous page): BSE image of the QUE 99177 dust grain mount (left), with white boxes labeled A–F, showing the locations of SIMS measurements with white circles. White circles are not to scale; all measurements have ~ 3 μm spot size except for F, which has ~ 5 μm spot sizes. Each BSE image has a scale bar in the lower right of the image. (A) A large HCP near the rim of a chondrule with two SIMS spots. (B) A small HCP embedded with silicate grains with one SIMS spot. The HCP itself is embedded in matrix materials. (C) Another small HCP with a single SIMS spot. (D, E) Eight SIMS spots in matrix areas previously X-ray mapped (Gasda et al., 2014). (F) Four SIMS spots on calcite grains in the matrix.

99
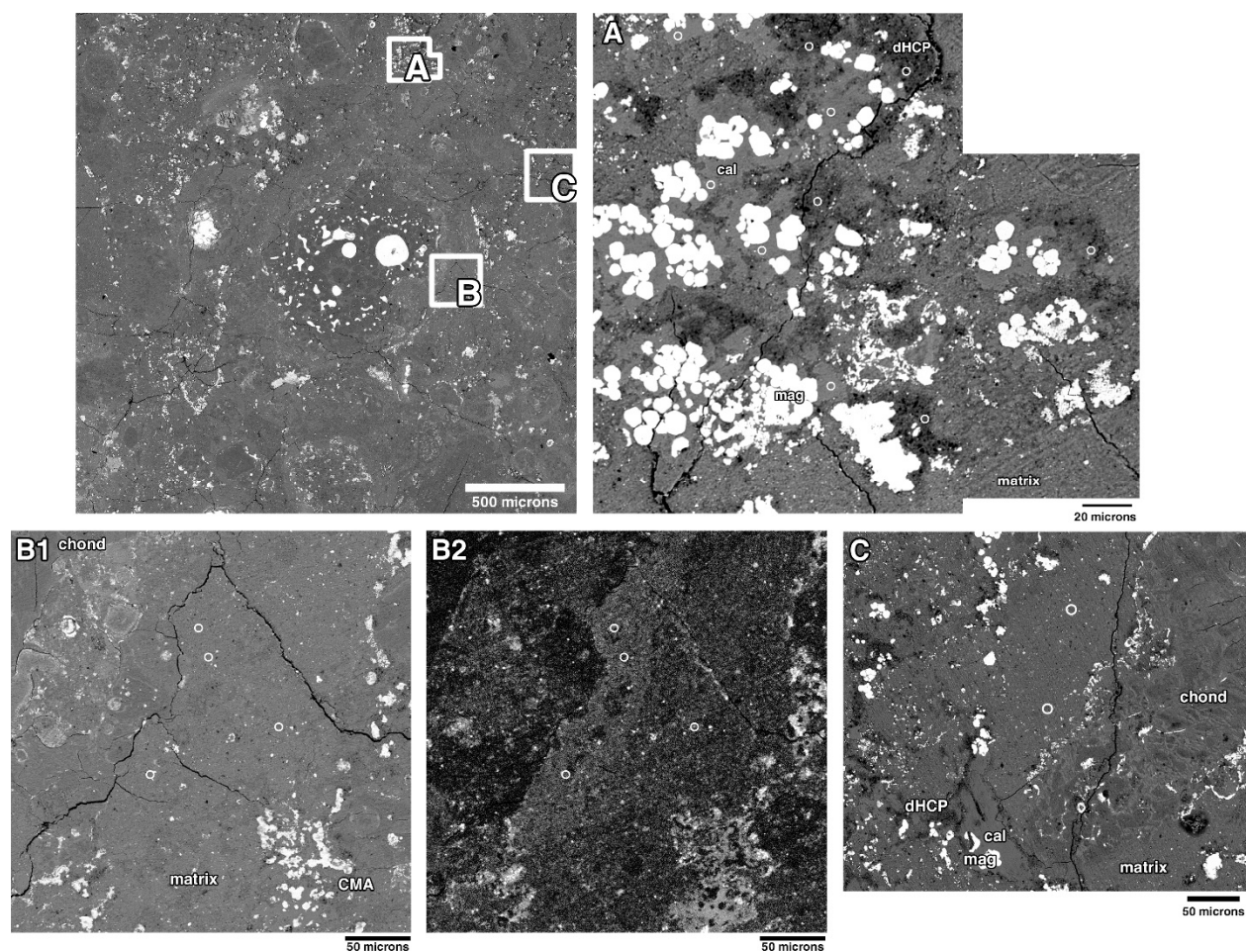
Figure 4.3: BSE image of the GRO 95577 sample (upper left), with white boxes labeled A–C, showing the locations of SIMS measurements with white circles. White circles are not to scale; all measurements have ~ 3 μm spot size. Each BSE image has a scale bar in the lower right of the image. (A) A BSE image of a prominent calcite-magnetite assemblage with large diffuse HCPs (labeled as 'dHCP' in the Figure) with major phases labeled. Five HCP and five calcite spots were sampled with the SIMS. (B1) A BSE image of an area of matrix between an aqueously altered chondrite rim (left) and a small calcite-magnetite assemblage (right) and its corresponding C Kα X-ray map (B2) showing a gradient of C abundance increasing towards the edge of the altered chondrule. Three SIMS spots sampled the area of higher C abundance and one SIMS spot sampled the area of low C abundance. (C) A BSE image of an area of the matrix (that was previously Raman mapped by Gasda et al., 2014) between an altered chondrule (right) and a small calcite-magnetite assemblage (left) with two SIMS sample spots.
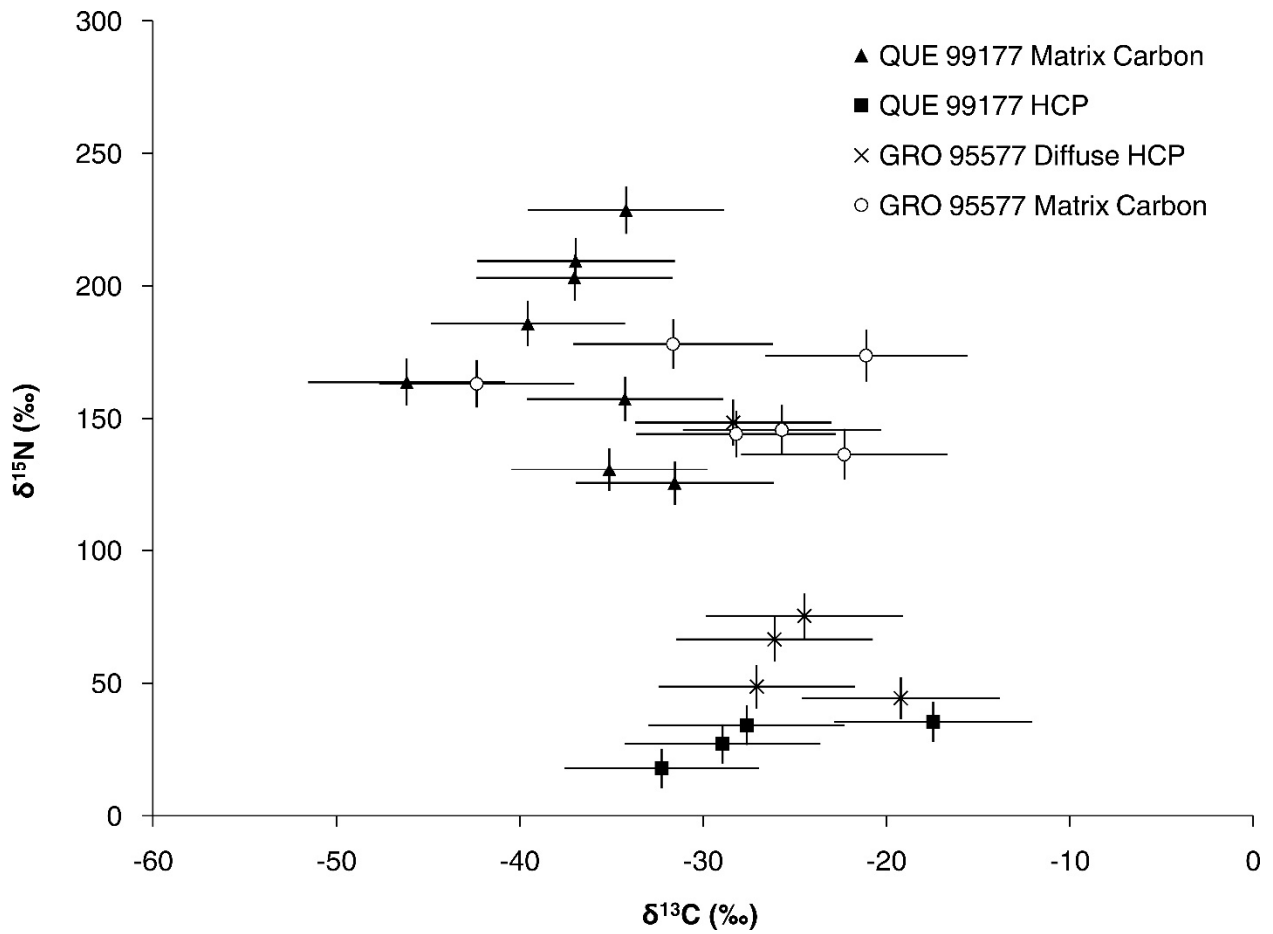
Figure 4.4: A plot of $\delta^{15}N$ and $\delta^{13}C$ SIMS results for QUE 99177 and GRO 95577 CR chondrites for the MC (Matrix Carbon) and HCPs (High Carbon Phases). Error bars are 2σ.

The IOM measured by Alexander et al. (2007) is an acid insoluble residue that likely was altered by the process of demineralization. Gasda et al. (2014) suggested that the atomic H/C of the MMC (measured in situ) are lower than what is reported by Alexander et al. (2007), and also that the demineralization process might have changed the atomic H/C value. In other words, demineralization might have modified the MMC to produce the IOM. During this reaction (which is irreversible, and an open system because the fluids carry away the dissolved minerals and are separated from the residues), carbon becomes kinetically fractionated, moving the IOM field to a heavier composition.

The HCP phase is enigmatic because it does not seem to relate to any other phase in Figure 4.5. HCPs could be related to IDPs, or derived from very heavy organics in the matrix. The presence of HCPs in the CR3 chondrite suggests that the HCPs were incorporated into the CR parent body during its formation. Therefore, HCPs may have a nebular or presolar source. If the HCPs come from the presolar molecular cloud, then the high $\delta^{15}N$ values seem to indicate that its precursor is the ^{15}N enriched (relative to the Sun) reservoir (N-bearing organics, and HCN, NH_3, and N_2). The HCPs are ^{13}C depleted, which may indicate that its percursor is derived from the ^{13}C-depleted organics reservoir in the molecular cloud. Both of these reservoirs are organic-rich, and thus they are consistent with each other, consistent with the hypothesis that the HCPs are pure organic phases (Gasda et al., 2014). Furthermore, our hypothesis is consistent with the hypothesis that the SOC in meteorites is derived from the presolar molecular cloud (Elsila et al., 2012). The HCPs might have formed in the protosolar molecular cloud and then altered in the nebula before being incorporated into the CR parent body. Alternatively, the HCPs might have formed in the solar nebula from isotopic reservoirs altered by self-shielding or other photodissociation processes.

Self-shielding and photodissociation processes in the solar nebula potentially creates large fractionations of O, N, and C isotopes (Lyons and Young, 2005). If fractionation of the isotopes due to self-shielding of N_2 is comparable to oxygen in CO (1000s ‰), then the heavy nitrogen reservoir resulting from self-shielding or photodissociation could have been incorporated into the HCPs and the missing MMC phase (Chakraborty et al., 2014). However, neither the HCPs nor the missing MMC phase have large carbon isotopic excursions from the inferred solar composition.

4.4.3 Calcite Carbon Isotopic Ratios

Figure 4.6 plots the $\delta^{13}C$ data for the sample spots (HCP, MC, and calcite) along with published carbonate data for some meteorite groups (Alexander et al, 2007, 2013). Table 4.1 lists the calcite data in our samples. The y-axis values are assigned arbitrarily to show the individual C-isotope compositions and the 2σ error bars. Figure 4.6 clearly shows that all of the organic carbon species have light $\delta^{13}C$ values while the calcite measurements become progressively heavier with extent of aqueous alteration. The QUE 99177 calcite grains have roughly terrestrial $\delta^{13}C$ values while the GRO 95577 calcite grains have high $\delta^{13}C$ values. It is possible that the calcite in QUE 99177 is due to terrestrial weathering. However, previous geochemical results from Gasda et al. (2014) suggest that calcite in QUE 99177 is related to the presence of dark inclusions, which are geochemically linked to the other CR chondrite samples, including GRO 95577. Those results have shown that the dark inclusions in QUE 99177 likely represent an intermediate stage of aqueous alteration (Gasda et al., 2014).

The high $\delta^{13}C$ values ($\sim$ 50 ‰) of the GRO 95577 calcite grains are consistent with published results for the other meteorite groups. Unlike the range for the CM carbonates and the one point for CR chondrites, the range of measured $\delta^{13}C$ is much wider. The wide range in $\delta^{13}C$ suggests that there is a high degree of kinetic carbon isotope fractionation, which could be due to outgassing of CO_2, or simply fractionation during the dissolution of CO_2 and the formation of calcite. Outgassing of CO_2 might not have occurred if the gas pressures within the parent body were too low to allow fractures to form (Alexander et al., 2013), but large early impacts on the parent body (Yang et al., 2008) may form fractures that allowed gas to escape. High $\delta^{13}C$ values can occur with fractionation of C during gas escape; irreversible reactions, such as photodissociation of gases and gas loss, can yield high $\delta^{13}C$ values. For example, the Mars atmosphere has a $\delta^{13}C$ value of 46 ± 4 ‰ (Webster et al., 2013). In this scenario, GRO 99577 has outgassed more than the intermediate stage of alteration experienced by the QUE 99177 dark inclusions.

Outgassing likely occurred on the CR parent body, and we can infer from our data how this might have occurred.[4] 1) At some point early in the aqueous alteration process (earlier than, or at the onset of, formation of the dark inclusions), CO_2 started to outgas. The CO_2 would become saturated in the fluids very early because the water:rock ratio is low at the onset of alteration. As alteration ramps up, so does CO_2 production to keep pace with higher water:rock ratios. 2) Outgassing continued during alteration, even as calcite started to form. Calcite also tends to be enriched in ^{13}C due to carbon fractionation during calcite formation. Equilibrium conditions must favor the formation of CO_2 gas, which seems counterintuitive for a system in equilibrium. The system is simultaneously producing abundant calcite while forming the CO_2 gas. However, the gas would need to be in equilibrium with the fluid in order for calcite to record the isotopic signature of the outgassing.

Modeling of the phases in the fluids may shed light on the process. Broadly speaking, the model must demonstrate a system in equilibrium that favors calcite formation, with a rate of calcite formation less than the rate of CO_2 formation. If this situation occurs, then CO_2 cannot dissolve because it has reached saturation, and escapes in the gas phase. Because the rate of calcite formation is the limiting factor, as CO_2 in solution becomes depleted to form more calcite, some of the CO_2 in the gas phase will dissolve, thereby recording the carbon isotopic signature at that moment in time. Modeling may give results that show that this scenario can only occur in certain pH or temperature ranges, which would constrain the conditions on the CR parent body.

Assuming that the CO_2 production rate is faster than the calcite formation rate, there is an interesting consequence. CO_2 needs to be produced and then *sustained* for ~ 10 Myr, based on Mn-Cr age dating of the calcite (Jilly et al., 2013). Jilly et al. (2013) also propose multiple alteration events in the CR parent body to account for long alteration history of GRO 95577. Thus, CO_2 production could be stopping and restarting for each alteration event.

---

[4] The fractionation of carbon isotopes during the formation of calcite from CO_2 and water has a negligible temperature and pH dependence, and it tends to fractionate carbon between the gas and the calcite by ~ 10 ‰ at 20°C and ~ 6–7 ‰ at 50 °C (Emrich et al., 1970; Romanek et al, 1992), which is likely the highest temperature during calcite formation (Jilly et al., 2014). Thus, crystallization of calcite does not fractionate the carbon enough to account for the high $\delta^{13}C$ calcite values in the CRs.

Table 4.1: The summary of carbon and nitrogen isotopic data for QUE 99177 and GRO 95577 CR chondrites. The Figure location column refers the reader to the BSE images (Figures 4.2 and 4.3) of the sampling locations.

Sample	Carbon Phase	Figure Location	$\delta^{13}C$	2σ	$\delta^{15}N$	2σ
QUE 99177	HCP	4.2 A	−28	5	34	7
QUE 99177	HCP	4.2 A	−29	5	27	7
QUE 99177	HCP	4.2 B	−32	5	18	7
QUE 99177	HCP	4.2 C	−17	5	35	8
QUE 99177	MC	4.2 D	−34	5	157	8
QUE 99177	MC	4.2 D	−37	5	209	9
QUE 99177	MC	4.2 D	−32	5	125	8
QUE 99177	MC	4.2 D	−46	5	164	9
QUE 99177	MC	4.2 D	−34	5	229	9
QUE 99177	MC	4.2 E	−37	5	203	9
QUE 99177	MC	4.2 E	−35	5	131	8
QUE 99177	MC	4.2 E	−40	5	186	9
GRO 95577	Diffuse HCP	4.3 A	−26	5	66	8
GRO 95577	Diffuse HCP	4.3 A	−27	5	49	8
GRO 95577	Diffuse HCP	4.3 A	−28	5	148	9
GRO 95577	Diffuse HCP	4.3 A	−24	5	75	9
GRO 95577	Diffuse HCP	4.3 A	−19	5	44	8
GRO 95577	MC	4.3 B	−22	6	136	10
GRO 95577	MC	4.3 B	−32	5	178	9
GRO 95577	MC	4.3 B	−26	5	146	9
GRO 95577	MC	4.3 B	−42	5	163	9
GRO 95577	MC	4.3 C	−28	5	144	9
GRO 95577	MC	4.3 C	−21	6	174	10
QUE 99177	calcite	4.2 F	4	9		
QUE 99177	calcite	4.2 F	−17	8		
QUE 99177	calcite	4.2 F	−1	9		
QUE 99177	calcite	4.2 F	7	9		
GRO 95577	calcite	4.3 A	43	19		
GRO 95577	calcite	4.3 A	73	20		
GRO 95577	calcite	4.3 A	23	19		
GRO 95577	calcite	4.3 A	6	19		
GRO 95577	calcite	4.3 A	20	19		
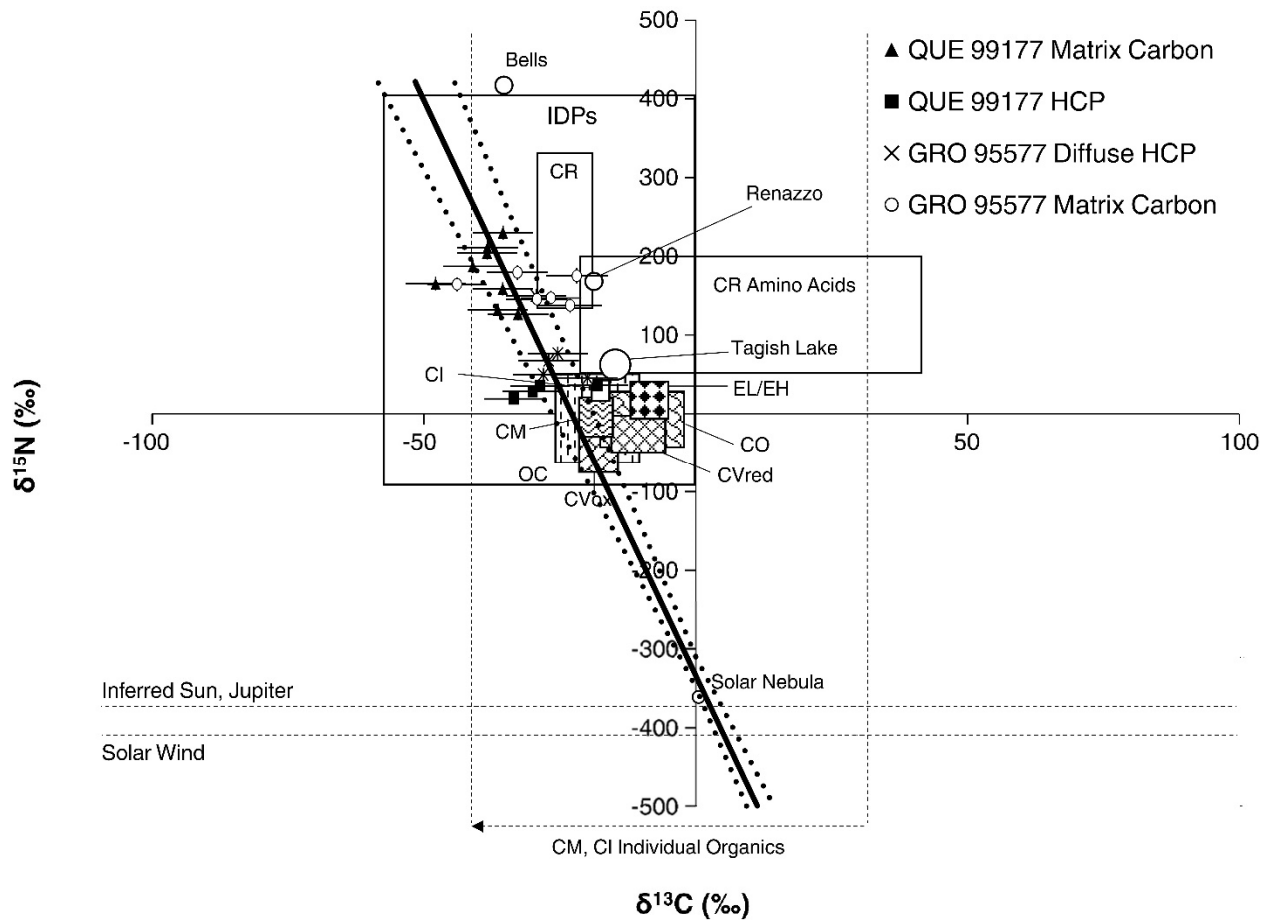
Figure 4.5: Data from Figure 4.4 superimposed on the literature data from Figure 4.1 (see Figure 4.1 and Introduction for details and citations). The bold line with 2σ error lines (dotted lines) is the weight mean fit through the data in Figure 4.4.
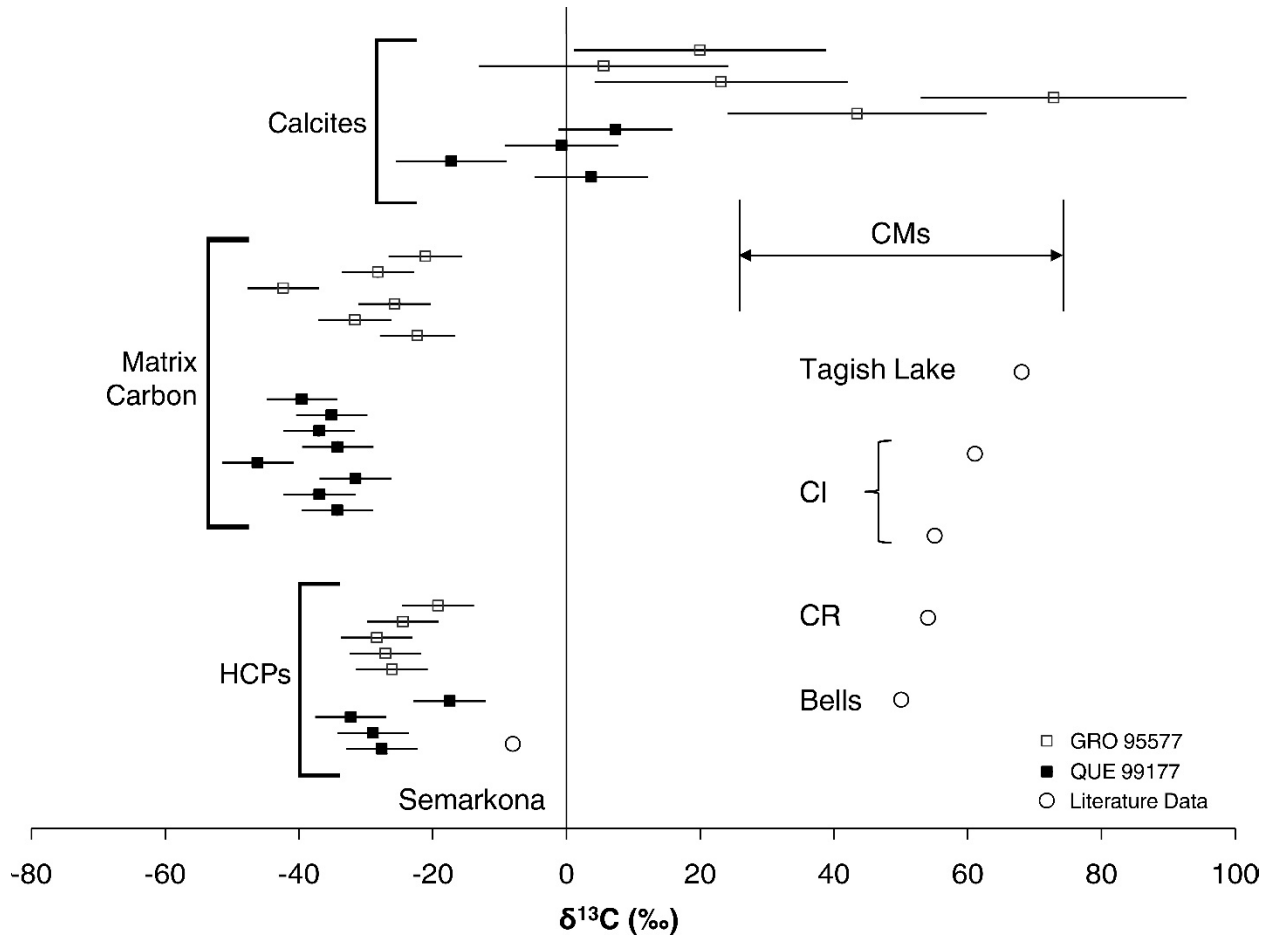
Figure 4.6: The $\delta^{13}C$ data for all of the sample spots with carbonate literature data for some meteorite groups (Alexander et al, 2007; 2013). Y-axis values are assigned arbitrarily to show the individual points with 2σ error bars and group them by HCP, MC (Matrix Carbon), and calcite grain measurements. The open squares are the data for the GRO 95577 measurements and the closed squares are for the QUE 99177 measurements.

There is no direct evidence that calcite is a product of aqueous alteration of the organic materials (e.g., by oxidation reactions), although kinetic fractionation trends seem to suggest that CO_2 formed from the organic phases. Since the QUE 99177 calcite grains fall close to the origin and the inferred solar nebula values, this may indicate that calcite formed directly from CO_2 ices that formed in the solar nebula. As explained in the introduction, the solar nebula value in Figure 4.1 and 4.5 is inferred from measurements of the possible nebular condensate osbornite (Meibom et al., 2007). But without measurements of the $^{13}C/^{12}C$ ratio in CO_2 cometary ice, it is hard to determine if solar nebula CO_2 ice is the source of CO_2 that formed these calcite grains. Theoretical models from Charnley and Rodgers (2008) suggest that the bulk nebula CO_2 ice is far too heavy ($\delta^{13}C \gg 1000$ ‰) to be the source of calcite, and it seems unlikely that CO_2 ice is the source of the CO_2 on the CR parent body. Thus, we hypothesize that the organic materials from either the MC or HCPs, which decrease in abundance during aqueous alteration, perhaps through oxidation by peroxide radicals (Alexander and Cody, 2005; Gasda et al., 2014), provided CO_2 to produce calcite. The heterogeneity of the delta values for MC cluster in Figure 4.5, and the long timescale for calcite formation (Jilly et al., 2013), would produce calcite with heterogeneous $\delta^{13}C$ values, which could account for the large range in values seen in our and the Alexander et al. (2013) results for CM chondrites.

4.4.4 Implications

It is likely that the HCPs and missing MMC phase formed from organics from the protosolar molecular cloud. The fractionation of C and N inherited from molecular cloud can account for all of the difference between the isotopic signatures in the refractory organics and the solar nebula bulk values (Figure 4.7A). Franctionation of N in the solar nebula is theoretically very large. So, only a small fraction of the MMC can be affected by the solar nebula in order for the MMC to retain the modest N isotopic signature we observe. If self-shielding or photodissciation did occur in the early solar nebula, it occurred in a very thin disk (Figure 4.7B). The HCPs may have been buried in an optically thick portion of the disk, which completely protected them from alteration by the nebula, creating the separate isotopic signature. Fractionation of the carbon isotopes would remain negligible in the disk as long as the system remains closed (e.g., organics embedded in ice). Open system fractionation (e.g., organics on

grain surfaces exposed to space) would produce an isotopically heavier residue and a lighter gas product, which does not seem consistent with the isotopic ratios of a refractory organic carbon phase that we measured in our samples.

Thus, we hypothesize that the organics that formed the MMC and the HCPs were not greatly altered in the solar nebula. Alteration in the nebula would be limited by the efficiency of mixing between the optically thick inner portion of the disk and the optically thin outer layer of the disk. If the carbon phases were buried in the optically thick portion of the disk and did not mix well with the outer parts of the disk, very little alteration should occur. Our hypothesis, illustrated in Figure 4.7, is broadly consistent with the Chakraborty et al. (2014) model. The starting point is the molecular cloud (Figure 4.7A), which produces the intial starting composition of the organics. MMC derived from these organics have a low atomic H/C ratio, are delpeted in ^{13}C, and enriched in ^{15}N. In Figure 4.7B, the disk forms and there is further fractionation of the N isotopes, which need to quickly react to form ^{15}N-enriched organics. These organics would also be slightly ^{13}C enriched (one hypothetical product is shown in Figure 4.7C) and would mix with the interior of the disk and come into contact with the MMC. The MMC is very high in C#, but there are only ~ 3 N atoms for every 100 C atoms (Alexander et al., 2007). The addition of a solar nebula product to the MMC (Figure 4.7C) introduces only a slight change to the C isotopic ratio, but greatly changes the N isotopic ratio. Thus, we only expect to see a modest change (if any) carbon isotopic signature as a result of this reaction (i.e., the carbon isotopic ratios would appear heterogeneous), accompanied by a significantly elevated nitrogen isotopic value. Upon further aqueous alteration, CO_2 is produced from the organic molecules. As some of the gas escapes (fractionating the C isotopes further), calcite forms. The leftover MMC and HCPs have a higher atomic H/C ratio after aqueous alteration.

The implications of this hypothesis are threefold. First, the heterogeniety of the measurements may be a clue that alteration in the solar nebula did occur. Second, the difference between the HCP and MMC isotopic signatures would result only from the degree of incorporation of nebular products. Third, the ^{13}C and ^{15}N-enriched portions of the MMC are the labile (outer) chemical groups attached to the aromatic portion of the MMC molecule. The labile groups would be the first groups to be altered at the onset of aqueous alteration (Figure 4.7D). Thus, we should be able to test this hypothesis with our data.

Essentially, the δ^{15}N value for the altered MMC should be lower than the unaltered MMC as the chemical groups holding onto the ^{15}N atoms are carried away by the fluid, but carbon isotopes would only change negligibly. Ironically, this means that the aqueously altered MMC is a closer representation of the MMC from the molecular cloud than the MMC measured in the primitive chondrites. Our measurements of the matrix shows that the GRO 95577 sample has slightly lower δ^{15}N values than the QUE 99177 sample (Figure 4.4), but the lack of a clear statistical separation of the values is less than convincing. Moreover, the QUE 99177 sample matrix is primarily made of dark inclusions, which have been aqueously altered, making it difficult to use QUE 99177 to test this hypothesis. More work has to be done to characterize the drier and more primitive samples in the CR collection, such as EET 92161 (Gasda et al., 2014), to see if our hypothesis holds.

4.5 Summary and Conclusions

Carbon and nitrogen isotopic values have been measured in organic and calcite phases of the CR chondrites QUE 99177 and GRO 95577. The organic phases in QUE 99177 are dark inclusions representing an intermediate phase of aqueous alteration on the CR parent body, while GRO 95577 is a petrologic type 1 exhibiting complete aqueous alteration. The δ^{13}C and δ^{15}N measurements of the organic phases, calculated relative to terrestrial standard values, show that the organic phases cluster into two groups, one for high carbon phases and one for matrix carbon.

Our findings do not agree with previous results by Alexander et al. (2007) because our measurements were performed in situ rather than by bulk analysis of insoluble organic residues. The matrix carbon should be a mixture of soluble organic carbon and macromolecular carbon, and therefore a mixing of their known isotopic signatures. The fact that our results are inconsistent with this hypothesis suggests that there is a missing phase with δ^{13}C ≈ -50 to -75 ‰ and δ^{15}N ≈ 100 to 300 ‰. We predict that the missing phase is macromolecular carbon, which, when mixed with soluble organic carbon, would produce the matrix carbon cluster in Figure 4.4. Hence, we believe we did not measure the macromolecular carbon phase during the course of our measurements; we have only inferred its composition.
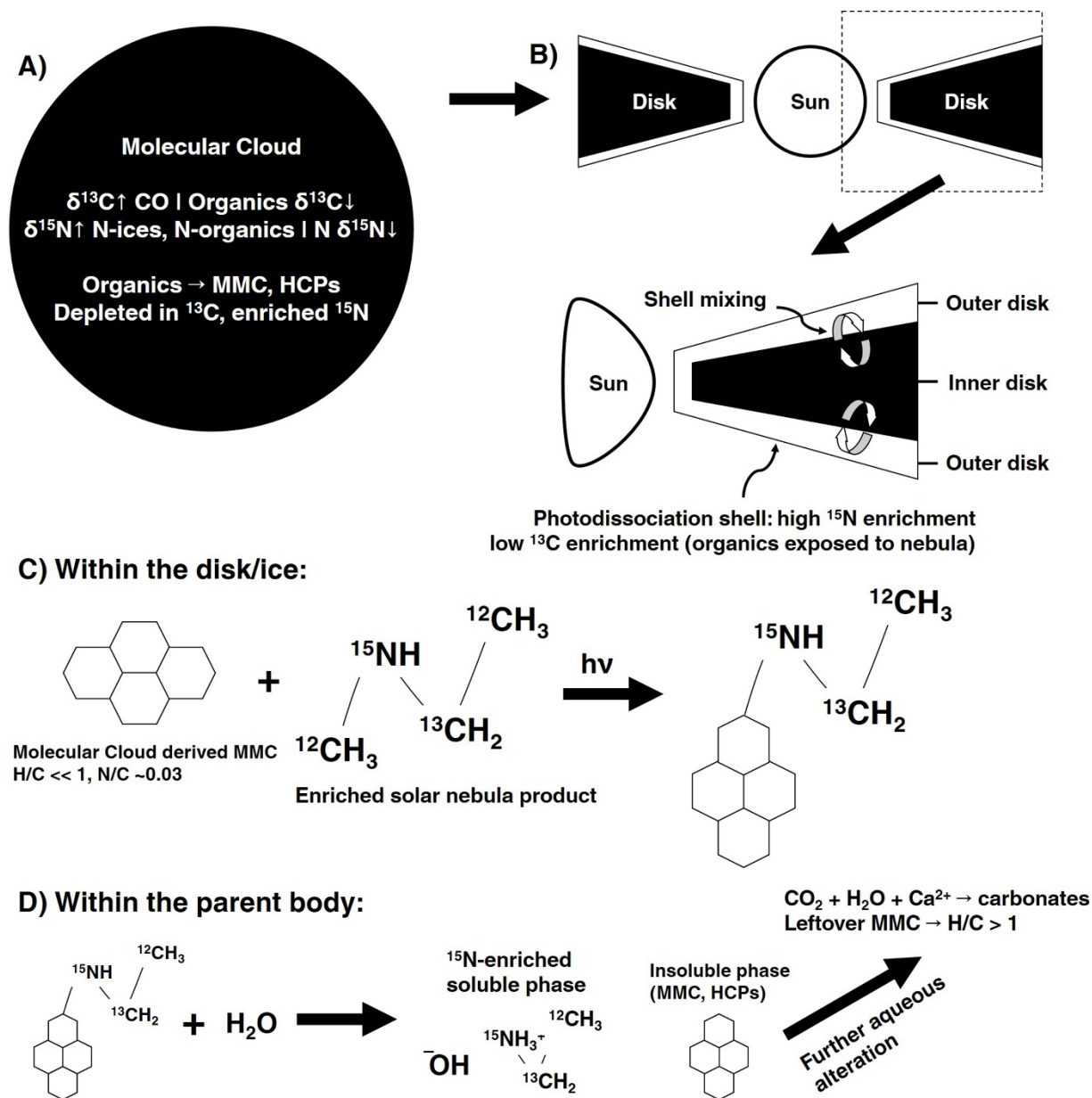
Figure 4.7: An illustration depicting the source of the macromolecular carbon (MMC) and high carbon phases (HCPs), showing the alteration steps in the solar nebula and the meteorite parent body. Parts A–C are based on Chakraborty et al. (2014). (A) Fractionation of C and N in the molecular cloud forms the initial reservoir or organics that produce MMC. The vertical lines indicate separations, and the up and down arrows indicate the direction of fractionation. (B) The molecular cloud collapses to form the Sun and the accretion disk. The disk is composed of an optically thin shell where photodissociation occurs and an optically thick interior. Further N and

C isotope fractionation occurs in the shell layer. The shell layer is small; most of the MMC from the molecular cloud is buried within the disk. (C) Solar nebula products react with the MMC to produce an altered MMC product with elevated $\delta^{15}N$. (D) These products are then altered on the parent body during the initial stage of aqueous alteration and lose most of the nebular products. Further aqueous alteration breaks apart the MMC and produces CO_2 (losing some in the process), and calcite forms.

The high carbon phases and macromolecular carbon might be derived from molecular cloud organic carbon and ^{15}N enriched N_2 gas, HCN, and NH_3 ices. Alternatively, the organics formed the high carbon phases and the macromolecular carbon in the molecular cloud. Some of that material was altered in the solar nebula before being incorporated into the high carbon phases, creating a heterogeneous isotopic signature. The organics altered in the solar nebula were accompanied by nitrogen from the ^{15}N enriched reservoir, which formed during N_2 self-shielding and photodissociation in the solar nebula, producing the elevated $\delta^{15}N$ values for both phases. The only difference between the high carbon phases and macromolecular carbon are the degree to which they experienced mixing of ^{15}N reservoirs from the protosolar molecular cloud or the solar nebula.

There is a broad range in $\delta^{13}C$ values for calcite in the GRO 95577 and QUE 99177 chondrites, which results from kinetic fractionation of carbon isotopes by calcite formation in an open system. Fractionation of carbon up to 100 ‰ could be due to outgassing of CO_2 gas; fractionation during the production of calcite accounts for a small degree of fractionation. It is likely that this gas formed during oxidation, possibly by peroxide radical reactions, of the organic materials during aqueous alteration of the CR parent body. It is unlikely that CO_2 gas can be formed from CO_2 ice from the solar nebula, based on the theoretical isotopic composition of the CO_2 and the Hale-Bopp comet HCN carbon signature.

Chapter 5

Conclusions

5.1 Aqueous Alteration of Macromolecular Organic Compounds in CR Chondrites

We have used a Savitzky-Golay Second-Derivative (SGSD) fitting method and Monte Carlo estimation of Raman uncertainties to study the Raman spectra of carbon-bearing materials in the CR carbonaceous chondrites. The SGSD method can account for various types of backgrounds; it is more robust than background subtraction methods. We have shown that SGSD is generally more accurate than other methods in a variety of other, more general, situations. SGSD varies much less than the float line, third-order polynomial subtraction, and SWiMA methods with changes in background shape. Variations in the Raman parameters determined through Raman simulations will help us estimate the significance of the variations in our real datasets, which are known to have variable background fluorescence. This information gives us the confidence to use the SGSD method to reduce large datasets of Raman spectral data from the CR carbonaceous chondrites.

The Raman point and image spectra of the CR carbonaceous chondrites were analyzed using our new SGSD method. The results reveal a statistically significant difference between the EET 92161 and GRO 95577 polished and unpolished single spot spectra as well as the distributions of their map spectra. Based on our SGSD simulation experiments, there is no scientifically meaningful difference between the two distributions I_D/I_G values. The differences are most likely due to changes in the fluorescence background. Polishing is responsible for differences in band width and band positions.

The distribution of macromolecular carbon (MMC) has been mapped in the QUE 99177 grain mount and the EET 92161 and GRO 95577 meteorite samples. The Raman mapped MMC locations are consistent with the matrix carbon (MC) mapped by electron probe microanalysis (EPMA). EPMA mapping of carbon also reveals HCPs in QUE 99177 and diffuse HCPs in GRO 95577. Raman measurements of diffuse and normal high carbon phases (HCPs) are also consistent with MMC. EPMA analysis also shows that the abundance of organics in the matrix decreases from $\sim$ 25–7 wt% as extent of aqueous alteration increases. Modeling of the EPMA results suggest that aqueous alteration changes the atomic H/C ratio of the MMC from < 1 to > 1. Atomic H/C ratios < 1 mean that there are a large number of internal carbons in the MMC, making the molecule very large. If this very large molecule is broken up into smaller units, then

the atomic H/C ratio increases. The change in morphology of the HCPs, the overall decrease in the abundance of organics, and the decrease in atomic H/C ratios suggests that MMC can be altered by aqueous alteration, either mechanically or chemically.

Breakup of MMC could occur by mechanical or chemical mechanisms, or a combination of both. However, neither chemical nor mechanical changes to the MMC are likely to fractionate the carbon or nitrogen isotopes in a closed system. Modification of the C isotopic signature in CR chondrites only occurs during open system alteration, such as calcite formation or loss of CO_2 by outgassing.

The $\delta^{13}C$ and $\delta^{15}N$ values have been determined for the matrix and the HCPs in the QUE 99177 and GRO 95577 samples. The isotopic study could shed light on the mechanism for MMC aqueous alteration on the CR parent body. The $\delta^{13}C$ and $\delta^{15}N$ measurements of the organic phases, calculated relative to terrestrial standards, show that they cluster into two groups, one for HCPs and one for MC. Relative to terrestrial values, the HCPs have $\delta^{13}C \approx -25$ ‰ and $\delta^{15}N \approx$ 40 ‰, and the MC have $\delta^{13}C \approx -35$ ‰ and $\delta^{15}N \approx 160$ ‰. Our findings do not agree with literature values, likely because our measurements were performed in situ rather than by bulk analysis of IOM residues. A weighted average line between these two clusters does not form a fractionation trend. Mixing along this line produces the elevated diffuse HCP $\delta^{15}N$ values in GRO 95577. The HCPs themselves might be a new phase derived from the molecular cloud organic carbon and mixing of the ^{15}N-depleted atomic N gas and the ^{15}N enriched N_2 gas, HCN, and NH_3 ices.

The matrix should be a mixture of SOC and MMC organic materials. If a mixing line is drawn from the known values for soluble organic materials (SOC) and the MC, it suggests that there is a missing phase with $\delta^{13}C \approx -50$ to -75 ‰ and $\delta^{15}N \approx 100$ to 300 ‰. We predict that the missing phase is the MMC. MMC has not been measured in a pure state either in situ or by demineralization techniques, but it could be studied using transmission electron microscopy.

Calcite grains are abundant in GRO 95577 and are present in QUE 99177 (suggesting that areas which probed by quantitative EPMA are dark inclusions). The abundance of MMC near calcite is lower than in the rest of the matrix. Calcite might be an alteration product of the reaction of soluble organics with oxidizing radicals via a Fenton-like oxidation.

There is a broad range in $\delta^{13}C$ values for calcite in the GRO 95577 and QUE 99177 chondrites. The broad range is due to kinetic fractionation of carbon isotopes by formation of calcite in either a closed or open system. Formation of calcite accounts for a C isotopic fractionation of only ~ 10 ‰. Fractionation of C isotopes due to outgassing of CO_2 is more likely; the gas may have escaped through fractures caused by an asteroid impact. It is likely that this gas is formed during oxidation of organic materials during aqueous alteration of the CR parent body. It is unlikely that the CO_2 gas can be formed from CO_2 ice from the solar nebula, based on the theoretical isotopic composition of nebular CO_2 ice and the Hale-Bopp comet HCN carbon signature.

The combination of Raman, EPMA, and SIMS results allows us to conclude that the macromolecular materials in the CR carbonaceous chondrites were altered by aqueous alteration. First, there is the presence of high carbon phases, which undergo a morphologic change from the less altered to the most altered meteorites. Second, the abundance of organics decreases in the matrix, especially in areas nearest to calcite grains. Third, the atomic H/C ratio of the organics decreases with extent of aqueous alteration. Fourth, calcite, the product of alteration, requires the production of CO_2 derived from organics, which are enriched in ^{12}C compared with calcite. In contrast, CO_2 ice should be heavily enriched in ^{13}C; thus, ice cannot be the source of the CO_2 to form calcite. The abundance of carbon in the matrix and its atomic H/C ratio changes significantly, suggesting that organics are destroyed; the production of CO_2 suggests that the mechanism is chemical oxidation. The CR parent body is not very oxidizing, as no sulfates form from the sulfides, and there is no hematite present. Therefore, an oxidizing organic material must be present, such as an organic peroxide, which is activated during the onset of aqueous alteration, to degrade the MMC.

5.2 Future Directions

If we are willing and able to improve the way that Raman spectra are measured, we can achieve more accurate and precise Raman fit parameter results. We could avoid using the SGSD method entirely in future studies. An improved method will pave the way for more accurate descriptions of the MMC in carbonaceous chondrites, as in this study, and new studies, which

will more accurately model the relationship between the peak metamorphic temperature and pressure on meteorite parent bodies and the Raman parameters in the MMC spectrum, for example.

First, we can avoid fluorescence in a Raman spectrum entirely by employing a time-resolved Raman experimental set up. Time-resolved Raman utilizes a pulsed laser and a gated camera. Since the Raman scattering lifetime is much shorter than the fluorescence lifetime, we can open the camera shutter to record only the Raman spectrum and close it before the fluorescence photons reach the camera.

Second, it is well known that I_D/I_G, D-band and D'-band positions are related to the excitation wavelength (e.g., Lucchese et al., 2010; Cançado et al., 2011; Pimenta et al., 2007). As laser energy decreases (increases in wavelength), I_D/I_G increases, D'-band intensity increases, and D-band and D'-band positions move outward from the G-band (see Figure 8 in Pimenta et al., 2007). This separation of peaks is critical to fit peaks accurately in spectra. It is especially important for the D'-band to move outside of the G-band and grow in intensity because, currently, the G-band and the D'-band are fitted as one peak. The 'true' peak position of the G-band is then calculated from the peak fit parameters (Ferrari and Robertson, 2000; Equation 6 in Chapter 1). The inability to model the D'-band peak in the current experimental set up may be the greatest source of error in the fitting model. At lower laser energies (e.g., a 694 nm pulsed ruby laser or a pulsed infrared laser), the D'-band may be sufficiently large to be modeled accurately. The separation of the D- and G-bands would also improve the accuracy of the fitting procedure.

Other possible improvements could be made for future studies. For example, the samples could be polished with alumina instead of diamonds. Alumina polish would still leave contamination on the sample surface, but it would be easier to distinguish the contaminants from the native carbon during EPMA mapping. Additionally, work should be done to measure the oxygen in the matrix with EPMA quantitative analysis and oxygen isotopes of the HCPs and calcite grains in our samples. Measurement of oxygen in EPMA spots would have made the oxide weight percent calculation more robust. Measurements of the oxygen isotopic ratios in the HCPs and the calcite grains would be a better demonstration of the link between calcite formation and aqueous alteration of organic carbon. Lastly, more work needs to be done to

117

measure the C and N isotopic ratios in the most primitive CR chondrites (i.e., EET 92161), which were not measured by SIMS in this study, to determine how the C and N ratios change due to extent of aqueous alteration.

5.3 Implications for the Origin of Life

In Chapter 1, I established an argument that the aqueously altered carbonaceous chondrites are good analogs for the Early Earth. Carbonaceous chondrites started with primary igneous materials, which became altered by liquid water, which was ~ 50 °C in CR chondrites. This is similar to processes that would have occurred before life began on the Early Earth. There is an incomplete record of rocks from the Early Earth; they are rare, heavily weathered, and contaminated with modern life. The lack of a complete rock record makes it difficult to infer the exact conditions on the Early Earth. Additionally, it is hard to study the stages of evolution of these rocks during this time period. Hence, we studied CR carbonaceous chondrites in this dissertation in order to ascertain the conditions or alteration, and to study its stages.

Soluble organic materials in meteorites have been well characterized. We can only theoretically determine what organic materials were present on the Early Earth based on inorganic chemical reactions in the laboratory and the biochemistry of modern life forms. Based on these studies, the Early Earth and meteorites should have broadly similar chemical inventories. Thus, studying the interactions of these chemicals in meteorites might only provide general information on terrestrial prebiotic chemistry.

Macromolecular carbon is the largest organic carbon component in meteorites, and it is unknown if macromolecules formed or were present on Earth before life began. Meteorites may have deposited macromolecules onto the Early Earth. The literature suggests that macromolecules, especially the polyaromatic parts, are inert. This dissertation has shown that macromolecules can be broken down during aqueous alteration. It is possible that the macromolecule decomposition products have been added to the prebiotic chemical inventory. The decomposition of macromolecules may be an important part of the pathway to the origin of life. Thus, macromolecules need to be considered and studied further as a part of studies concerning the prebiotic chemistry of Earth.

Appendix

Supplementary Materials for Chapter 3

A.1 Aluminum Coating

Samples were coating using a Torr International Metal Coater with a FTM-2000 thickness sensor. The thickness sensor is calibrated with metal density and Z-factor (a sensor calibration constant supplied by the manufacturer). Aluminum and silver coats were tested at various thicknesses on glass microscope slides and pure synthetic graphite. The glass slides were cleaned using the RF plasma cleaning unit at 3.2 torr with argon in the metal coater and coated at 4.6×10^{-6} torr with 28.0 and 56.0 nm Ag and 52 nm Al on one slide. The graphite pieces were not cleaned with plasma and coated at 5×10^{-6} torr with 25.0 and 51.0 nm Al. All samples were mounted in an electron probe mount using copper tape to ensure grounding.

The coated samples were tested in the electron microprobe. All Ag and Al coated samples were conductive. Silver coating in the electron probe looks patchy and uneven, which could indicate uneven coating or oxidation of the surface. The spots on the Ag coated surfaces have lower electron backscatter. For this reason, Ag is deemed unsuitable for coating our samples. On the other hand, the Al coating is looks smooth and even. There were no patches, so this coating was chosen for further testing.

Aluminum coated samples were tested against an uncoated pure synthetic graphite chip. The tests used wavelength dispersive X-ray spectroscopy with a spectrometer (LDE2 crystal) centered on the Kα C peak of graphite and another centered on the Kα Al peak (TAP crystal) from a coated sample, with a 10 KeV accelerating voltage, 20 µm beam size, and a 5 nA beam current. Solid graphite had $\sim 51.6 \times 10^3$ C X-ray counts and 16 Al counts. The 25 nm coating decreased the C counts to $\sim 40.3 \times 10^3$ carbon X-ray counts (~ 22 % decrease in signal) and increased to the Al to 761 counts. The 50 nm coating decreased the C counts to $\sim 25.0 \times 10^3$ carbon X-ray counts (~ 51 % decrease in signal) and increased to the Al to 2155 counts. Based on these tests, a 25 nm thick Al coating was chosen to the rest of the samples.

A.2 Standards

The following information lists the details of the analysis that was performed on the samples. The purpose of the analysis is to determine the carbon and major element composition of the matrix of the CR chondrites samples: QUE99177 (CR3), EET92161 (CR2), and GRO95577 (CR1). We also explain the differences in our procedure and some of the rationale behind our decisions. We hope that anyone using this procedure will be able to replicate it in the future.

Special notes on the standards: The graphite standard is mounted separately, pressed onto gold foil. The mineral standards provided fresh from the Smithsonian were cut, mounted in epoxy, and polished by JoAnne Sinton at the Univ. of Hawaiʻi at Mānoa Geology and Geophysics Lapidary Facility. The two standard mounts and the three samples were simultaneously coated with 25 nm of aluminum using a Torr Inc. evaporative metal coating chamber. Measurement Settings used for standard measurements: beam size is 10 μm, accelerating voltage is 15.0 KeV and beam current is 10 nA.

Table A.1: Element measurement settings.

Elements	Crystals	Spectrometer	Time (s)	Standard #
Si	TAP	3	30	240
Al	TAP	3	30	248
Fe	LIF	4	60	244
Mg	TAP	5	30	247
Ca	PET	2	20	243
Na	TAP	5	30	240
K	PET	2	20	240
S	PET	2	20	143
C	LDE2	1	60	249

Table A.2: Details on the standards.

Probe std#	Holder Position	Mineral	Locality	Smithsonian Designation	Coating
240	A	Anorthoclase	Kakanui	NMNH 133868	25 nm Al
241	B	Augite	Kakanui	NMNH 122142	25 nm Al
242	C	Calcite	unknown	NMNH 136321	25 nm Al
243	D	Dolomite	Oberdorf	NMNH R10057	25 nm Al
244	E	Fayalite	Rockport	NMNH 85276	25 nm Al
245	F	A99 Glass	Makaopuhi Lake	NMNH 113498-1	25 nm Al
246	G	Magnetite	Minas Gerais	NMNH 114887	25 nm Al
247	H	Olivine	San Carlos	NMNH 111312-44	25 nm Al
248	I	Plagioclase	Lake County	NMNH 115900	25 nm Al
249	N/A	Synthetic Graphite	Graphtek LLC		25 nm Al
143	N/A	Troilite	Staunton Meteorite		Carbon

A.3 EPMA Procedure

Elements (Table A.1) were peaked using the standards listed in Table A.2. All elements except carbon were measured with detector Peak Height Analysis (PHA) in integral mode. After initial C peaking on calcite, a PHA scan was acquired and C intensities were measured in differential mode. Carbon was first peaked on dolomite, with a spectrometer peak position of 122.6 mm. The previous spectrometer peak position on graphite, recorded during the initial X-ray mapping phase of the project (Dec 2013), was 123.7 mm. We centered the spectrometer on graphite on 5/6/2014, with a position of 123.7 mm, which is the value we used for the QUE 99177 measurements. Subsequent centering of the spectrometers were performed during the analysis (GRO 95577:123.06; EET 92161: 122.8 mm). Background peak positions were chosen after evaluating high-resolution Wavelength Dispersive X-Ray Spectroscopy (WDS) spectra (see Figures below) in the range between 80 and 160 mm, on several metal and mineral standards. An exponential background fit was chosen to calculate the on-peak background intensity. Spectrometer background was roughly the same for all WDS spectra. An exponential function with a factor of three was used. The high carbon background position was 158.606 mm and the low carbon background position was 90.6052 mm.

After centering the spectrometers on the carbon peak, we acquired standard intensities of all elements on the standards listed in Table A.1. San Carlos olivine, Rockport fayalite, calcite, A99 glass, and Lake County plagioclase were measured as unknowns. This was to test if the standard measurements could reproduce the published values of these standards. We also wanted to determine how the aluminum coat contributes to the total aluminum measured by the probe. When measured on mineral standards that nominally have no Al, such as San Carlos olivine or Rockport fayalite, Al is ~ 2.4 wt%. We used one of these San Carlos olivine measurements as the blank value for the rest of the measurements. The amount of aluminum coating measured by the probe changes depending of the standard (with nominally zero Al) measured. The average for all San Carlos olivine measurements was 2.41 wt%, fayalite was 2.52 wt%, calcite was 2.11 wt%, and graphite was 1.54 wt%. The average for all meteorite samples was ~ 3.1%. We also applied a blank correction to Al by averaging multiple San Carlos olivine measurements.

The next step is to evaluate the carbon background. These are the sources of carbon background:

- Epoxy or oils/restudies on the standards. Carbon-free standards contaminated by the cutting polishing processes, mounting in epoxy, etc. There is little chance for this type of contamination of the samples because they were cut without oil and they were mounted on gold (QUE 99177) or indium metal (EET 92161 and GRO 95577). There could still be 'stray' carbon on the surface of either the samples or the standards because they were not kept in a clean-room environment, though they were kept in a desiccator when not in use. The stray carbon could be introduced before or after being coated with Al.

- Carbon contamination in the electron probe. This can occur if carbon coating flakes off or if other users hit epoxy with the electron beam. This contamination would happen regardless of the history of the sample.

- Higher order peaks from heavy elements (e.g., Ni Lα III). This could be an issue, but the higher order and/or L and M shell peaks for the heavy elements will only appear if the element was at a high concentration. This could be a problem since our element standards for Fe, Ni, and Ti are 'pure,' but the metals and metal oxides in the samples contain many other heavy elements.

- Spectrometer background. Background due to LDE2 crystal and in the detector.

- The left tail (high-energy side) of the nearby oxygen Kα II peak (130 mm).

- Carbon build-up under the electron beam during analysis.

Table A.3: C Kα Intensity (cps) measured in WDS spectra of the different standards (both JEOL standards and ones listed in Table A.2) and unknowns. The WDS spectra were recorded to look for interferences in the carbon peak and the background positions.

Sample	C Kα intensity (cps)	Coating
Ti (JEOL standard)	640	None
Fe (JEOL standard)	200	None
Calcite	2900	25 nm al
Dolomite	2300	25 nm al
A99	200	25 nm al
Plagioclase	120	25 nm al
Troilite	1300	Carbon
Benitoite	1200	Carbon
Anorthoclase	70	25 nm al
Magnetite	140	25 nm al
San Carlos olivine	80	25 nm al
Fayalite	100	25 nm al
GRO 95577 magnetite	55	25 nm al
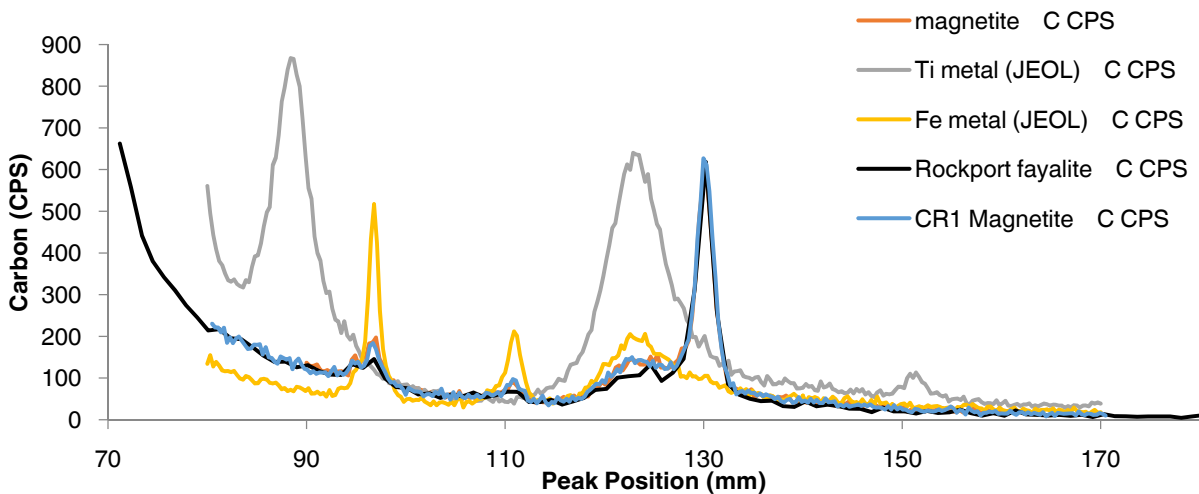
Figure A.1: Heavy metal bearing material WDS spectra. The sharp peak at ~ 130 mm is the Kα X-ray peak for oxygen. The broad peak in the center of the WDS spectrum is the carbon peak. Note that the JEOL metal standards have a lot of carbon contamination, but the unknown (GRO 95577 magnetite, blue trace) and our prepared standards (magnetite, red trace; fayalite, black trace) have a very low (almost background) level of carbon.
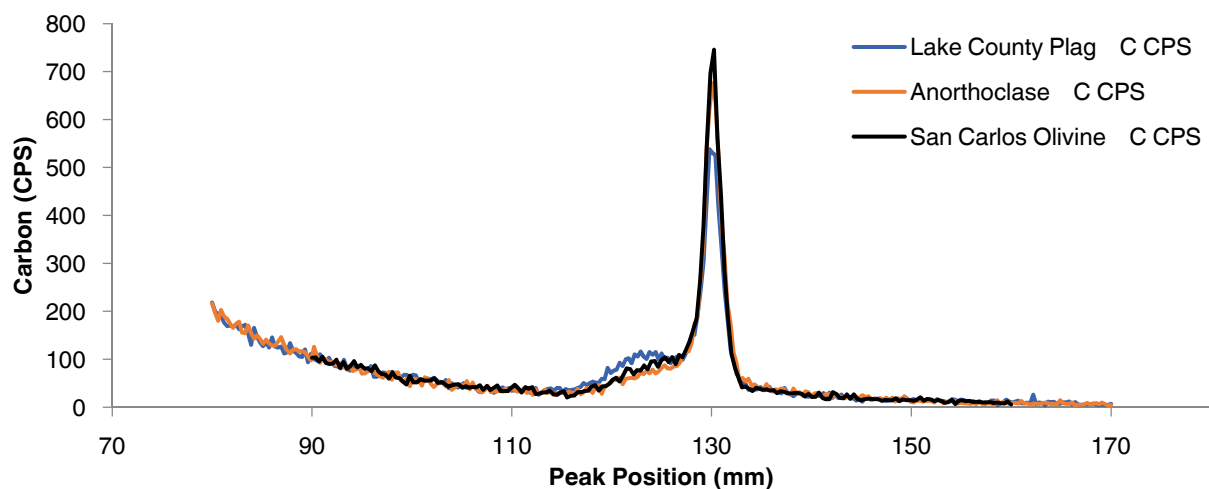
Figure A.2: Carbon-free mineral WDS spectra. These are the three WDS spectra of our prepared standards with the lowest carbon levels.
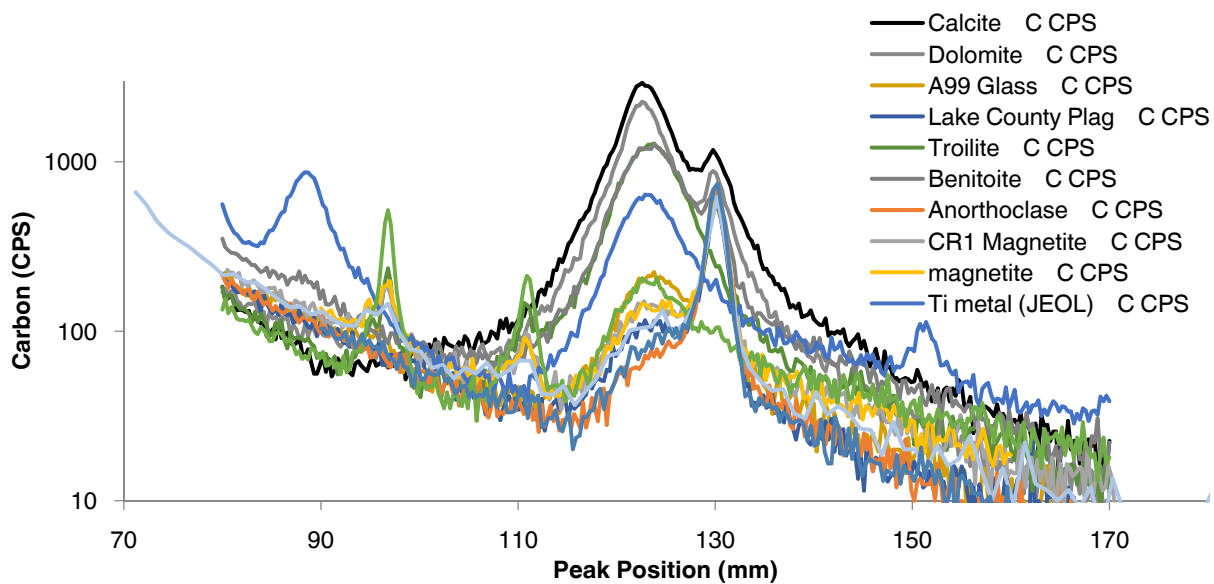
Figure A.3: All of the WDS spectra on a Log scale plot.

126
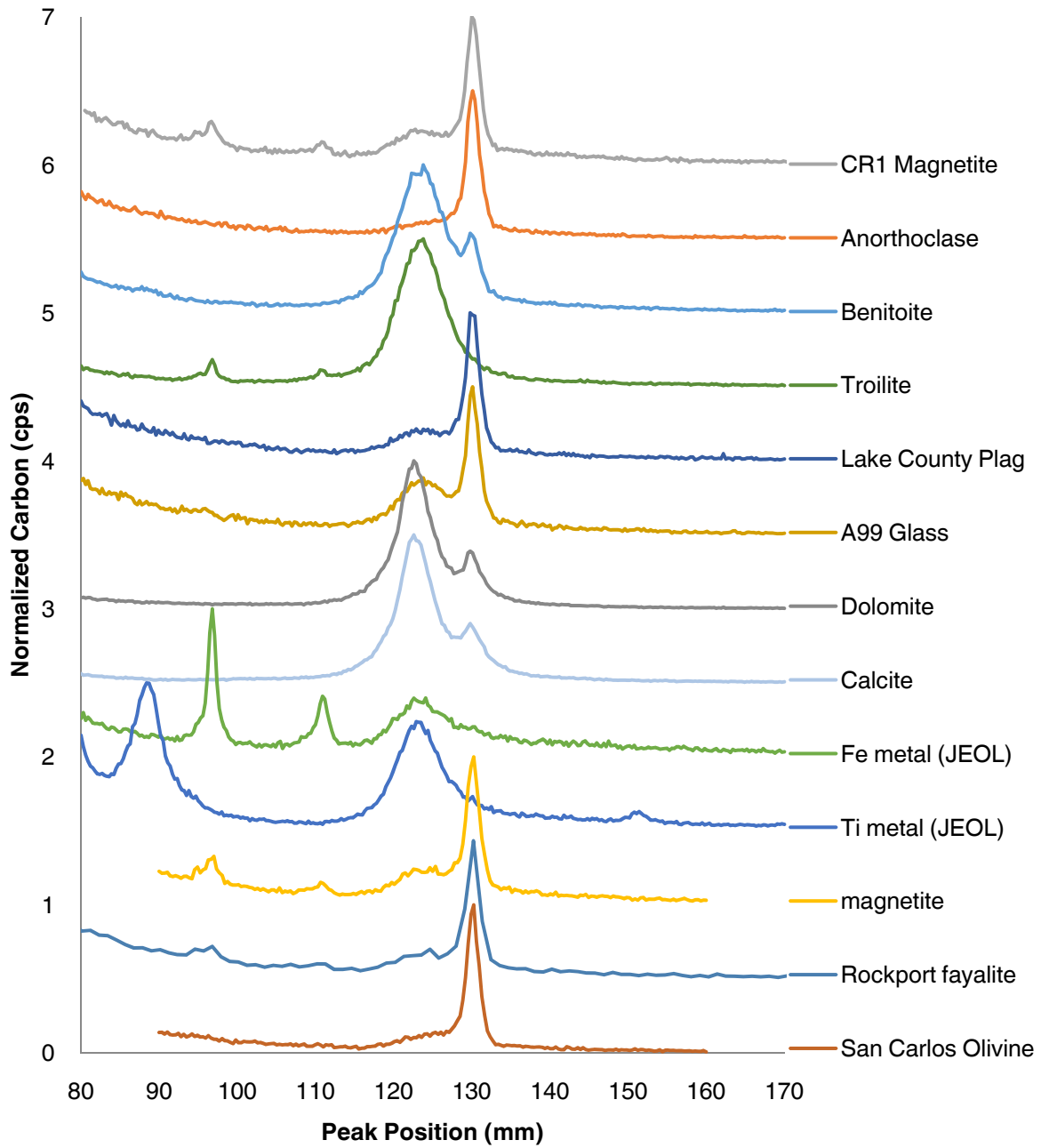
Figure A.4: All of the WDS spectra unity normalized and stacked for clarity.

San Carlos olivine has the least amount of interference in the carbon peak (Figure A.2), so this standard was used for further testing of the behavior of carbon in the probe. JEOL standards are probably contaminated with surface organics (these are not kept inside the probe at all times like the carbon coated standards). Benitoite and troilite standards are carbon coated. The A99 glass may contain some carbon, although it is nominally volatile-free outgassed volcanic glass. Note how the calcite and dolomite carbon peak positions are shifted to the high energy side of the spectrum.

Next, we need to determine if the carbon signal increases over time due to repeated measurements at the same spot. If the electron beam stays on the same spot, carbon signal can increase. This is largely due to surface contamination due to hydrocarbons. The hydrocarbons are broken apart by the electron beam. Other hydrocarbons are drawn to the spot. Certain techniques could compensate for this, including cold fingers or jets of O_2 to produce CO_2 gas, which is drawn away from the sample by the vacuum pump. We do not have these devices on our electron probe. Overall, the background of the probe is considered to be low because of an oil-free pumping system (two scroll pumps, two turbo pumps, two ion pumps).

Since the WDS spectra sit on the same place for a long time before the carbon peak is measured, the peak height inferred from the WDS spectra may be overestimating the carbon peak. Figure A.4 shows the carbon wt% (normalized to Si) for the same spot is measured on San Carlos olivine ten times. A sample change is performed and the sample measured again three more times. Below is a graph that shows that the carbon wt% increases relative to Si wt% (Si wt% should remain contain during the measurement).

Over the course of about 30 minutes, Figure A.4 shows that the carbon concentration increases by 0.29 wt%. WDS spectra (carbon WDS spectra are 5 s per point) take approx. 25 minutes to complete and pass over the carbon peak about halfway through the WDS spectrum. In our same spot measurements, the measurement that started at 9:31 AM had an increase of 0.086 wt% C. So the increase of the carbon peak intensity over the duration of recording the WDS spectrum is very low. Additionally, as long as each sample measurement is far away from previous measurements, we can probably avoid overestimating carbon concentration. The first three measurements of San Carlos olivine (in the black box) are used as a carbon blank correction (0.59 wt%) for all of the sample measurements.
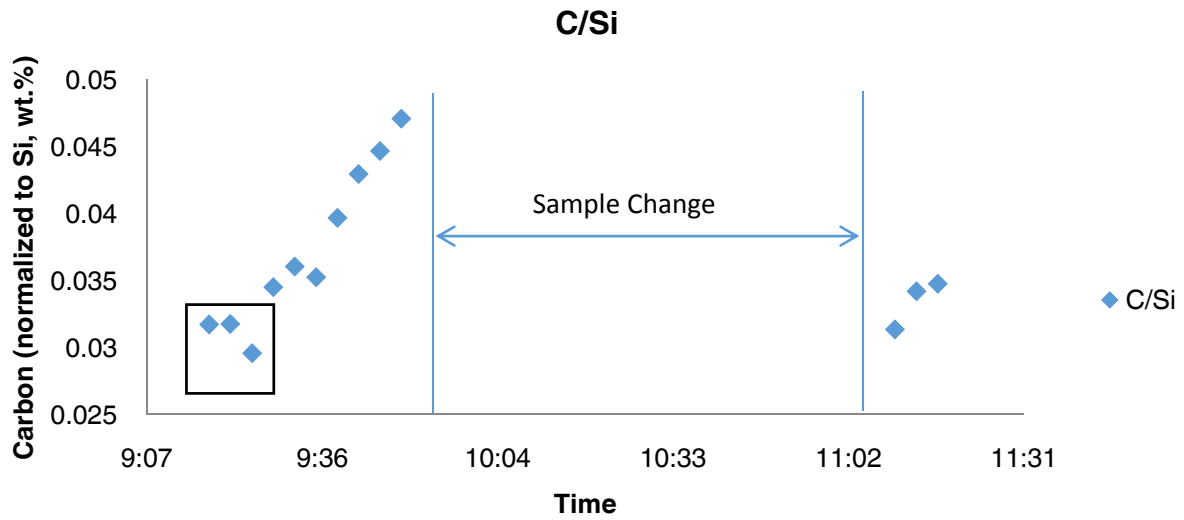
Figure A.5: C/Si wt% ratio of a single spot over time. The electron beam is kept on the same spot for ~ 30 minutes. The gap in time between the 10th and 11th measurement is for a sample change. After almost an hour has elapsed the C/Si wt% values are still elevated for the three new measurements were performed at the same spot. The black box highlights the three measurements that are used to blank the carbon measurement for all unknown measurements.

The last test done was to see the difference in spectrometer peak position with C wt% when different standards are used. Since the peak position of C changes depending on the standard (calcite: 122.6 mm; graphite: 123.7 mm), carbon concentration can decrease slightly if more carbonate is present in a fine-grained sample. There is approx. a 10 % decrease in count rate with the wrong peak position, which amounts to a 0.5–1 at% difference (2–3 C wt% difference). Small differences between sample measurements of a very fine-grained matrix could be due to the different concentration of carbon phases in addition to normal variability between measurements. Repeated measurements on samples that do not have sufficient charge compensation could cause a systematic increase in carbon signal. Figure A.5 shows that charge compensation might affect nearby measurements of carbon concentration in the EET 92161 and QUE 99177 samples.

Perhaps the spatial position of each measurement (groups are sometimes separated by more than 100 μm) negates the problem of change compensation. If charge compensation is an issue, then the plots in Figure A.6 will show that each spatially close group of points within a sample should steadily increase. For example, the middle graph shows two groups of points taken in the QUE 99177 sample. The second QUE 99177 group (red points) steadily increases, so charge compensation may be a problem with this measurement. All of the measurements in this group (middle graph, red points) were taken within ~ 100 μm. For the other measurements in the other meteorites, there are no obvious upwards trend in the group data. The trends may be due to actual variability of the carbon content in the samples. These measurements tend to have much larger spatial separations.
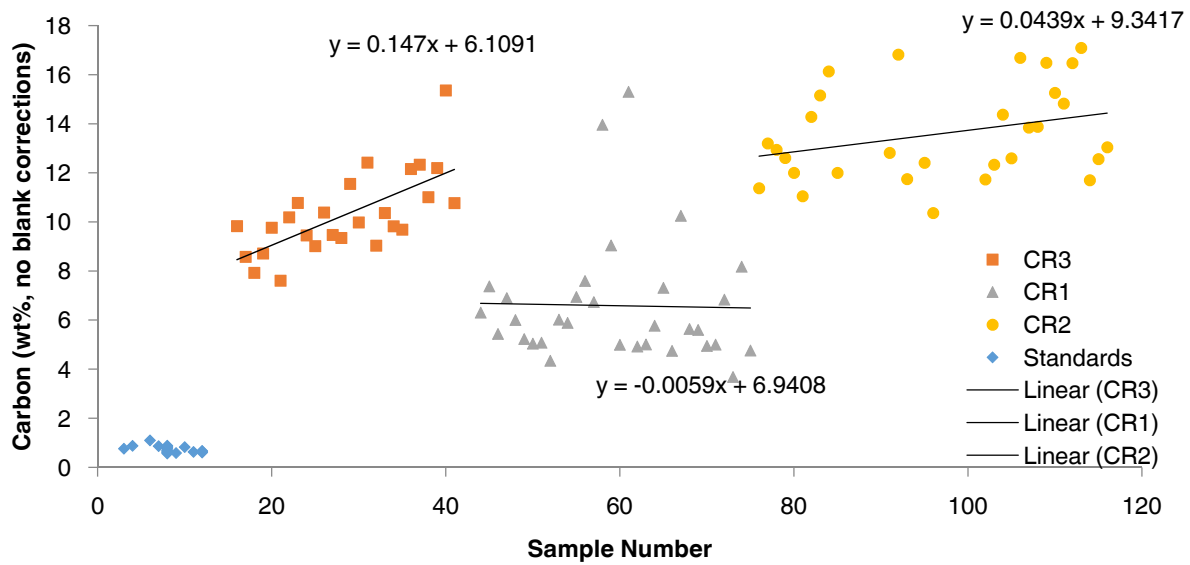
Figure A.6: Raw data for all measurements on the standards and the samples with trend lines for the unknowns.
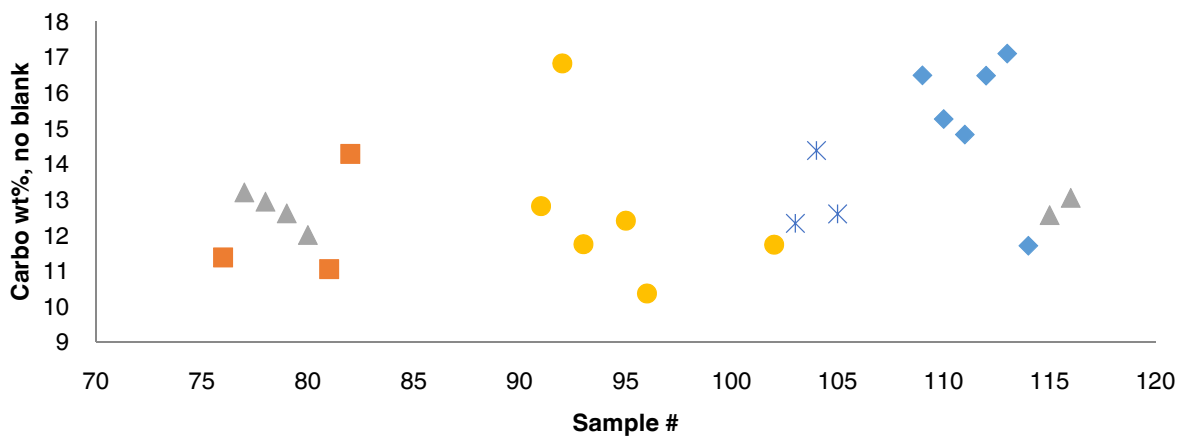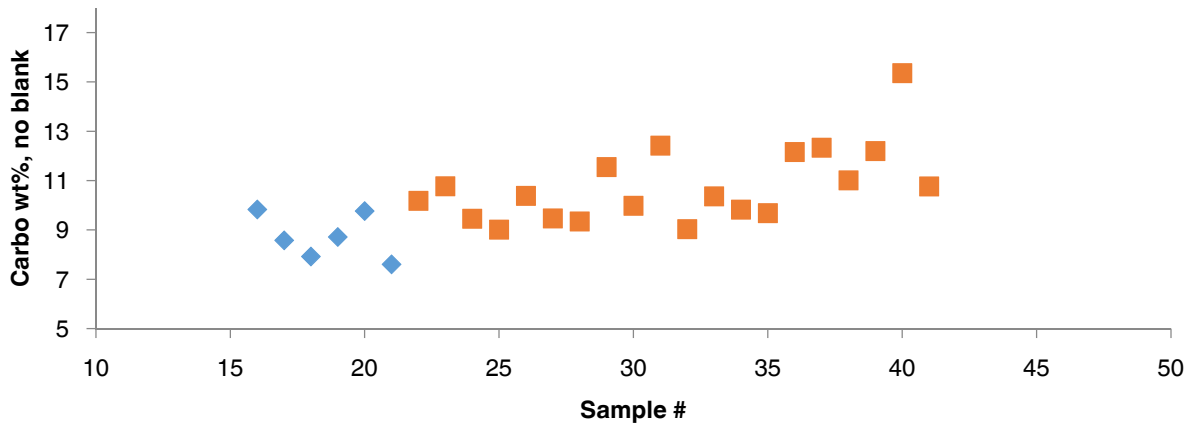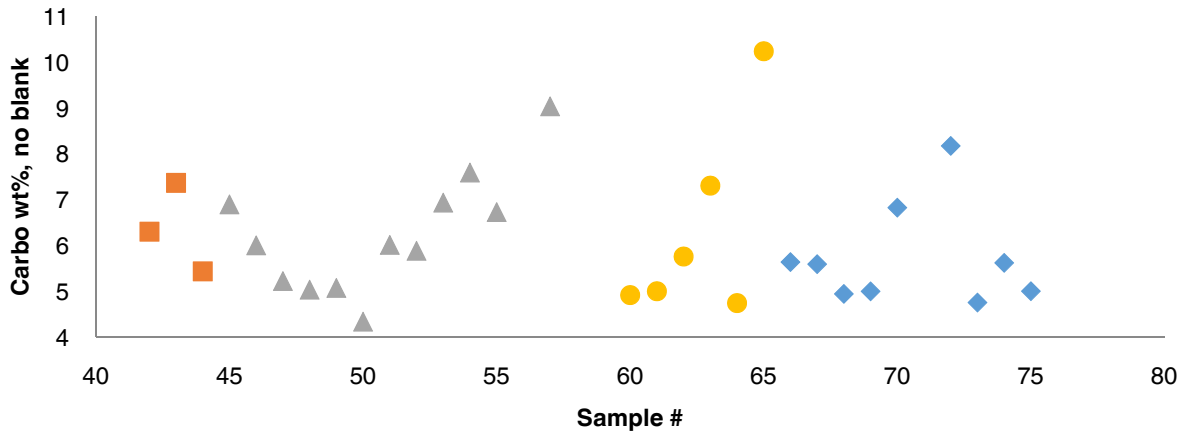
Figure A.7: Raw data vs. sample number for GRO 95577 (top), QUE 99177 (middle), and EET 92161 (bottom) grouped by their spatial similarity.

Silicon has the largest correction for carbon. Aside from Fe, no other elements in this chart are expected to be in the sample in large quantities (> 1 %). Fe and Si are the two elements with the largest measured concentrations (~ 20 wt% and ~ 14 wt%, respectively). The fact that Si does not correlate with the concentration of C in our measurements is comforting (Figure A.7). Fe and Mg do vary with carbon concentration, but they are also well correlated with each other in the expected fashion (i.e., solid solution chemistry) (Figure A.8). Unfortunately, there is a correlation between C and K, and there does not seem to be a correction for K absorptions in Table A.4. Additionally, we used the default Armstrong/Love-Scott Phi-Rho-Z correction factors in this test calculation (Figure A.5). Changing the correction factors to the Full Pouchou & Pichoir correction factors only changes the carbon by ~ 0.1 wt%.

There is also the matter of choosing the correct MACs. The default MACs may not be suitable. Updated MACs are provided by the NIST FFAST database (Chantler et al., 2005). These MACs are supposed to improve the accuracy of the low energy X-Ray lines, especially in the sub 10 KeV range. The light element Kα lines and the transition metal L and M shell lines are in this energy regime. The combined Full Pouchou & Pichoir correction and the FFAST MACs systematically decrease the measured carbon. The change depends on the sample, but the change is approx. 0.5–1.5 wt% in the samples and negligible in the standard measurements (carbon background). Figure A.8 shows the decrease in the C wt% from the Probe for Windows default (Armstrong/Love-Scott Phi-Rho-Z correction factors with the LINEMU MACs) to our settings (Full Pouchou & Pichoir correction with the FFAST MACs).

Table A.4: Appendix C from the Probe for Windows Manual showing the variation between MAC values for carbon.

Emitter		Absorber	Henke & Ebisu	Ruste	Henke et al	Bastin & Heijligers	Heinrich	Pouchou & Pichoir
C	Kα	B	37020	37020	37000	41000		39000
C	Kα	C	2373	2373	2350	2373	2147	2170
C	Kα	Si	36980	36980	36800	37000		35000
C	Kα	Ti	8094	8094	8090	9400	8290	8097
C	Kα	V	8840	9236	8840	10100		8850
C	Kα	Cr	10590	10482	10600	10950		10700
C	Kα	Fe	13300	13300	13900	13500	14103	13150
C	Kα	Zr	31130	31130	21600	24000	31304	25000
C	Kα	Nb	33990	24203	19400	23200	29760	24000
C	Kα	Mo	32420	15500	16400	19200		20500
C	Kα	Hf						18000
C	Kα	Ta	18390	20000	18400	16000		17000
C	Kα	W	18750	21580	18800	17000		18000
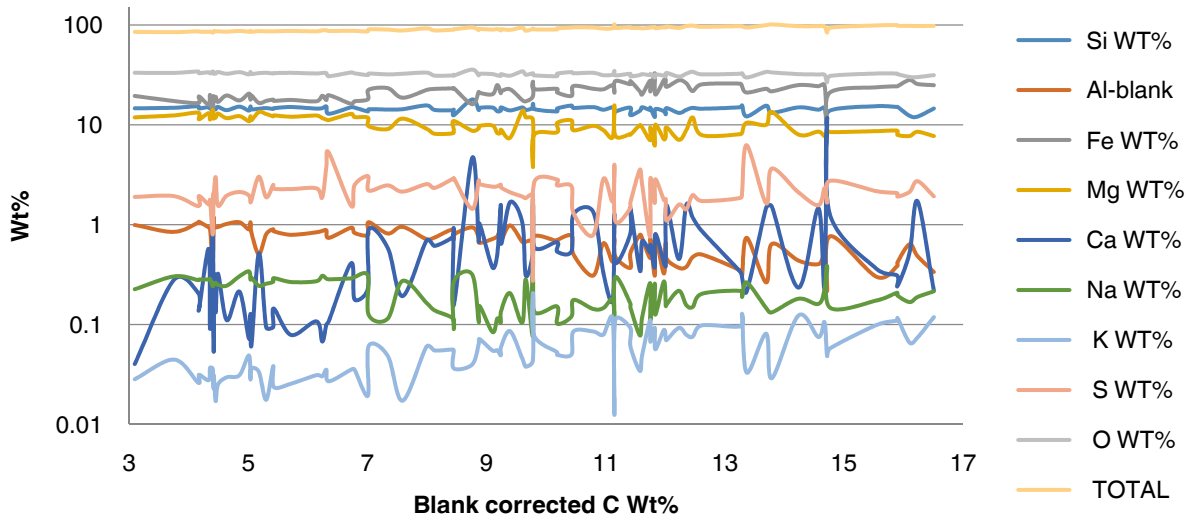
Figure A.8: Carbon blank corrected data for all samples and all elements on a Log plot.
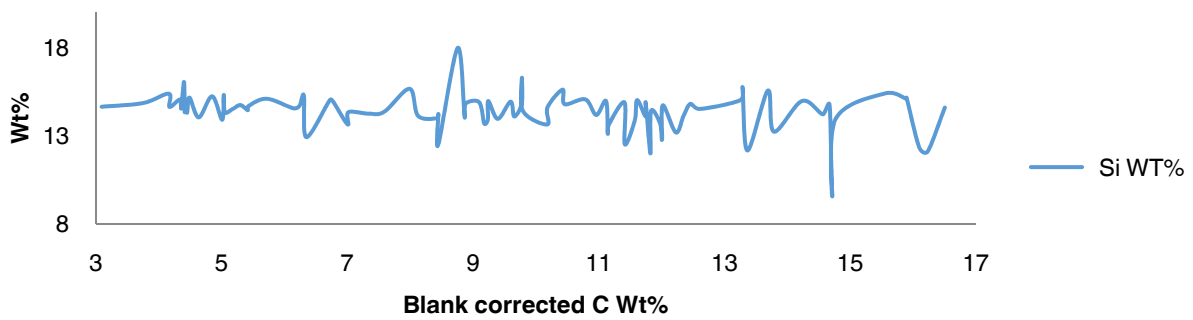
Figure A.9: Carbon blank corrected data for all samples highlighting only the silicon plot from Figure A.8.
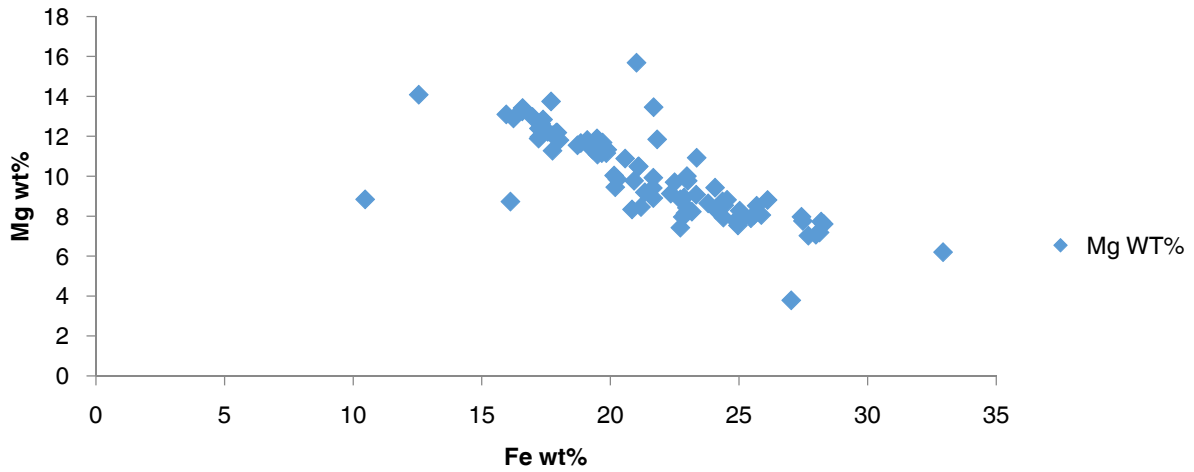
Figure A.10: Carbon blank corrected data for all samples highlighting the strong correlation between Fe and Mg abundance.
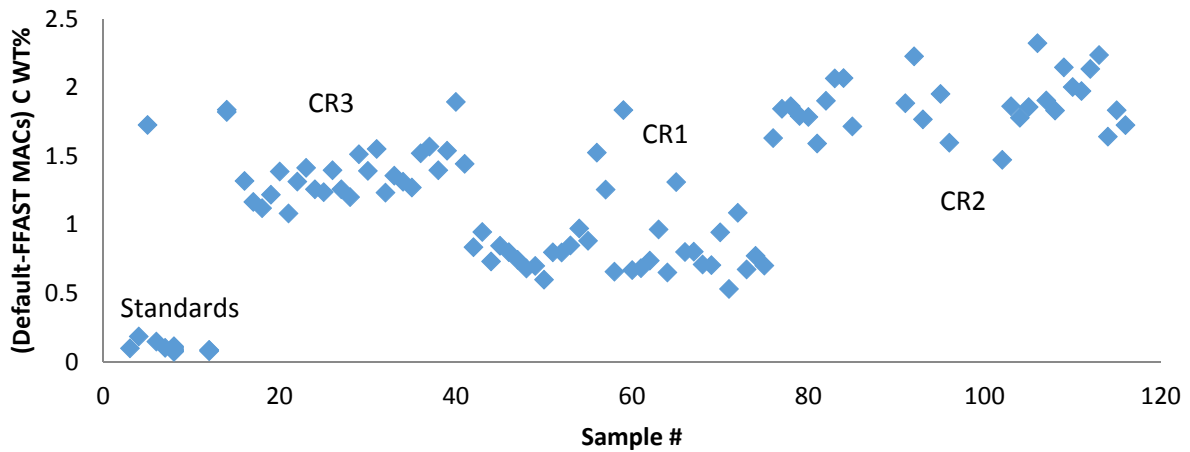
Figure A.11: Wt% difference in the carbon values between the Armstrong/Love-Scott Phi-Rho-Z correction factors with the LINEMU MACs and our settings, the Full Pouchou & Pichoir correction with the FFAST MACs.

A.5 Oxide Weight Percent Calculation

The goal of the quantitative analysis of the matrix of these samples is to reduce the dataset in a logical way. We want to determine the contribution of organics and water make to abundance of the other materials in the matrix. Most of the details of the rationale can be found in the main paper text. Here, we give the procedure we follow, and then we will show an example of an oxide calculation from GRO 95577 and EET 92161.

1) Convert from wt% to at%. We do not normalize to 100 % as the probe software automatically does, but normalize to the wt% totals.

2) Multiply at% by 1000 to get the number of atoms. Subtract the total number of atoms from 100,000 atoms to get the 'leftover atoms.'

3) Assign all the sulfur to Fe as sulfides and the rest of the Fe as FeO in the unaltered meteorites and Fe_3O_4 (magnetite) in the GRO 95577 chondrite (see below for the explanation).

4) Calculate leftover oxygen atoms.

5) Assign oxygen atoms to major elements as usual (SiO_2, Al_2O_3, MgO, CaO, Na_2O, K_2O).

6) Calculate leftover oxygen atoms.

7) Determine the number of H, N, and O atoms that should assigned to the carbon atoms based on previous literature and/or a simple model (Table 3.1 in paper). Calculate the number of leftover atoms by subtracting out the number of H and N atoms added to the carbon. Calculate the number of leftover oxygen atoms by subtracting the number of oxygen atoms added to the carbon.

8) Use the leftover oxygen atoms to make water. Subtract the proper number hydrogen atoms from the leftover atoms.

9) Convert the oxides to oxide at% by dividing through by 1000.

10) Convert atomic percent oxides to weight percent oxides.

A.5.1 Iron partitioning

Typically, iron is partitioned as FeO_T (T = total) because of the different speciation/oxidation of iron in the different phases of silicates, oxides, etc. However, we have some information about how iron behaves in these meteorites. First, we know that sulfides are abundant and that, despite extensive aqueous alteration of these meteorites seen in GRO 95577, the style of alteration is such that the sulfides remain unaltered. So for all meteorites, we assign all of the sulfur as sulfides as FeS, and remove the equivalent amount of iron from the total iron pool.

Second, we know that iron becomes magnetite during serpentinization. GRO 95577 is completely serpentinized and magnetite is abundant. Although there may be Fe^{2+} and Fe^{3+} in phyllosilicates in the matrix and other uncommon iron bearing species (Fe-bearing olivine and pyroxene), assigning the iron to magnetite in GRO 95577 is the simplest way to account for Fe^{2+} and Fe^{3+} abundance in the model. EET 92161 and QUE 99177 have experienced some alteration, mostly in the matrix, so there might be magnetite in their matrices. There also might be native iron and iron in silicates. To split the difference, it might be the best to assign the rest of the iron in EET 92161 and QUE 99177 as FeO_T.

A.5.2 Organic Carbon Modeling

The details of the modeling are in Chapter 3, but here we go through the steps that we take to settle on the 'Revised model' (Table 3.1). First, we use the most recent and complete atomic H/C, N/C, O/C dataset (Alexander et al., 2007) of demineralized IOM residues, which we are calling 'Endmember 1.' See Table below. We ignore the atomic S/C column because the value is very low. For the Alexander et al. (2007) dataset, GRO 95577, QUE 99177, and EET 92042 were measured. Since EET92161 and EET 92042 are paired samples, we use the values from this meteorite for our calculations.

Table A.5: Endmember 1 atomic H/C, O/C, and N/C ratios (Alexander et al., 2007).

	H/C	N/C	O/C	S/C
QUE 99177	0.803	0.0365	0.146	0
EET 92161	0.757	0.0383	0.166	0
GRO 95577	0.756	0.0316	0.114	0.007

In the first pass through the data using Endmember 1, the atomic H/C ratio is ~ 1 for all the samples. For the samples with high C content in the matrix, this endmember produces too many hydrogen atoms. So the totals all go over 100 wt% after the amount of water is calculated. Calculating water as OH or H_2O does not make much difference because the number of H atoms in water are an order of magnitude less than the number of H atoms in the organics. The totals for GRO 95577 are slightly less than 100 % using Endmember 1. We considered two other endmembers: completely saturated carbon (C_nH_{2n+2}) and very low hydrogen (atomic H/C = 0.05). The saturated endmember (2) created about twice as many hydrogen atoms as Endmember 1, which is too many hydrogen atoms for GRO 95577. The third endmember created too little hydrogen for all three samples, but the totals for EET 92161 and QUE 99177 were much closer to 100 % than with any of the previous attempts.

Using the information from the endmembers, we made the first simple model (Table A.6) where we minimize the number of leftover atoms after the water is calculated by adjusting atomic H/C. We left atomic N/C and O/C alone. EET 92161 and QUE 99177 tend to have high carbon abundances, so these two samples work better with low atomic H/C ratios. GRO 95577 has low carbon but also higher original totals, so this sample tends to work well with an atomic H/C ratio close to 1. For QUE 99177 and EET 92161, the average totals calculated using this model are within 0.1 % of 100 %, but there is significant spread. The standard deviation of QUE 99177 is ~ 1.8% while the standard deviation of EET 92161 is ~ 2.9%. This spread likely reflects some heterogeneity of the matrix organic composition and/or some influence from calcite in the matrix.

Table A.6: Model atomic H/C, O/C, and N/C ratios.

	H/C	N/C	O/C
QUE 99177	0.275	0.0365	0.146
EET 92161	0.11	0.0383	0.166
GRO 95577	1.2	0.0316	0.114

GRO 95577 has a very different value, and also a lot of spread in the data calculated using this model. In this second pass through the data with the model atomic H/C ratios, there is a population of high carbon wt% and high final totals that seems to be different from most of the other GRO 95577 measurements (above the line in Figure A.9). These measurements seem more EET 92161- or QUE 99177-like. To make the model simpler, we discarded these measurements and calculated a revised GRO 95577 atomic H/C value of 1.45 which results in totals close to 100% and a standard deviation of 2.4 % of the totals. There are two outliers in EET 92161 with significantly higher totals; with these two values discarded, the new atomic H/C value is 0.135 and the totals have a standard deviation of ~ 2.1 %.
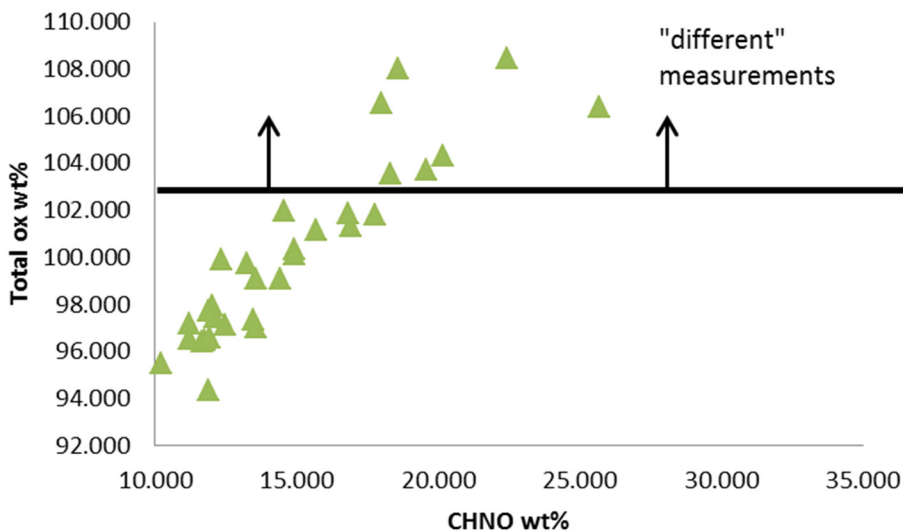
Figure A.12: GRO 95577 model atomic H/C before revision of the model. Some results with high CHNO wt% give high (> 105 %) totals. These high totals are anomalous and were discarded.

Table A.7: Revised model atomic H/C, O/C, and N/C ratios.

	H/C	N/C	O/C
QUE 99177	0.275	0.0365	0.146
EET 92161	0.135	0.0383	0.166
GRO 95577	1.45	0.0316	0.114
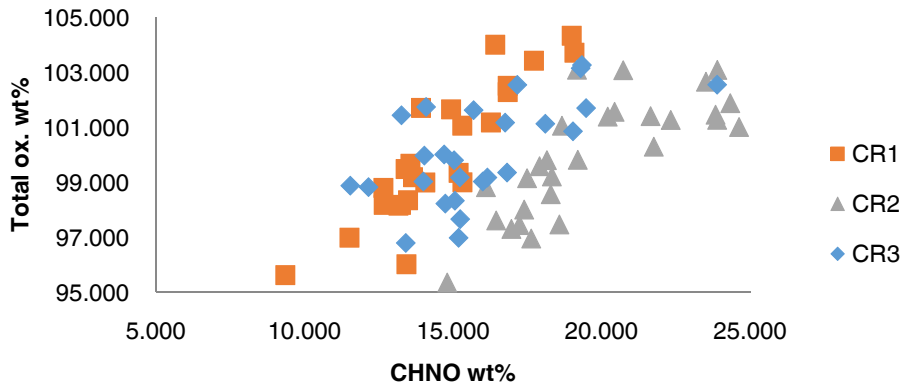
Figure A.13: After the discarding the anomalous results, a revised model was determined. The plot above shows the distribution of the totals with the revised atomic H/C model.
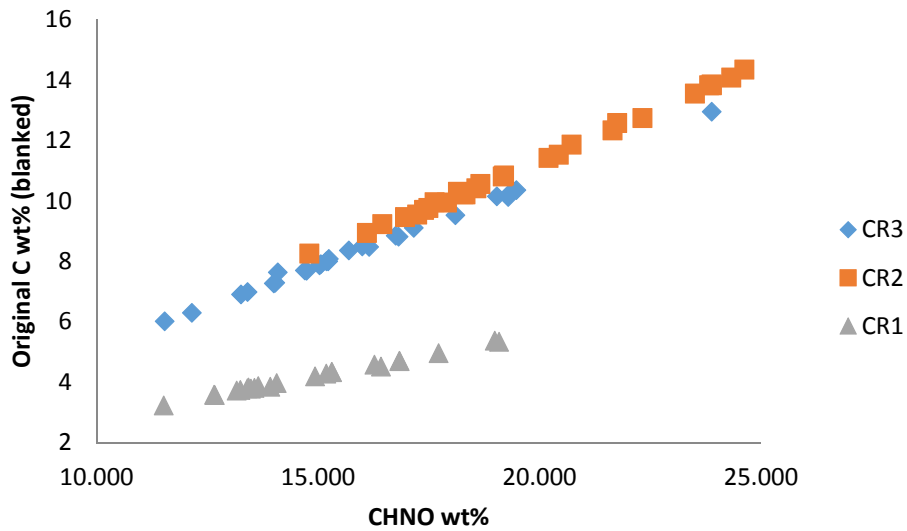
Figure A.14: The plot shows the relationship between the Revised Model CHNO vs the original C wt% values (after blanking). EET 92161 and QUE 99177 are very similar because they both

have high C values and similar atomic H/C ratios. GRO 95577 follows a different trend and had a much lower amount of C originally.

Table A.8 shows two sample calculations using the oxide weight percent calculation procedure with the revised model for determining atomic H/C, O/C, and N/C. Table A.8 shows the example of a measurement taken in EET 92161 that uses FeO_T for iron partitioning. The second example in Table A.8 is a measurement from GRO 95577 that uses Fe_3O_4 for iron partitioning. The data in Table A.9 are used to make the geochemical plots and the ternary diagrams used in Chapter 3. To read Table A.8, use the procedure from Section A.5 to read Table A.8, starting with number 1 in the first data column to convert wt% to at%. Atomic % is converted to atoms in the third column. Atoms are assigned in the Oxide Calc column (procedure steps 3–6) using the oxygen atom pool (O row in the atoms column). After the major element oxides are determined, the organic atoms are determined using the oxygen atoms calculated in step 6 and the leftover atoms subtracted from the total number of atoms. The remaining atoms are used to calculate water in procedure step 8 (if there are no leftover atoms, then water is set to zero). The oxides are converted from atoms (# Oxides column) to Ox% in procedure step 9 and then converted to wt% in procedure step 10 (Ox wt% column). Table A.9 then shows all of the resulting data for every measurement except those that were discarded.

A.6 Significance of the Atomic H/C Ratios

Here we give a little more detail about the significance of the atomic H/C ratios that are already given in the main paper. We provide some helpful figures that show molecules with different atomic H/C ratios. The typical chemical formula for an organic molecule follows the equation C_nH_{2n+2} for completely saturated molecules and the atomic H/C ratio decreases as the molecule becomes more saturated. A very saturated molecule like benzene has an atomic H/C ratio of 1 (C_6H_6). The only way to decrease the atomic H/C ratio below 1 is to make polyaromatic hydrocarbons (PAHs) by linking multiple benzene rings together. In PAHs, only the outside corner carbons (explicitly labeled in blue in Figure) have hydrogen atoms bonded to them, and the rest of the interior carbons have no hydrogen atoms bonded to them.

Table A.8: Two examples of the wt% oxide calculation using the revised model ratios in Table A.7.

Elements	Wt%	At%	# Atoms	Oxide Calc	# Oxides	Oxides	Ox at%	Ox Wt%
Sample # 76 / Sample Name: CR2_Matrix1
C (Blanked)	9.744	17.6008	17601	FeS	553	FeS	0.553	2.20
Si	14.848	11.47032	11470	FeO	8477	FeO	8.477	27.70
Al (Blanked)	0.289	0.232344	232	Fe_3O_4	0	Fe_3O_4	0.000	0.00
Fe	23.242	9.029518	9030	Leftover O	36302	SiO_2	11.47	31.350
Mg	9.738	8.692405	8692	SiO_2	11470	Al_2O_3	0.116	0.792
Ca	1.337	0.723509	724	Al_2O_3	116	MgO	8.692	15.94
Na	0.142	0.133975	134	MgO	8692	CaO	0.724	2.37
K	0.084	0.046805	47	CaO	724	Na_2O	0.067	0.19
S	0.817	0.552641	553	Na_2O	67	K_2O	0.023	0.10
O	33.022	44.77896	44779	K_2O	23	CHNO	23.57	16.448
Total	93.261	93.26129	93261	Leftover O	3552	H_2O	0.630	0.516
				Leftover Atoms	6739	Total	--	97.62
				C	17601			
				H	2376			
				N	674			
				O	2922			
				Leftover O	630			
				Leftover Atoms	3688			
				H_2O	630			
				H	1260			
				Leftover Atoms	2428			

Table A.8 (Continued): Two examples of the wt% oxide calculation using the revised model ratios in Table A.7.

| Sample # 42 | | | | | | | |
| Sample Name: CR1_Matrix1 | | | | | | | |

Elements	Wt%	At%	# Atoms	Oxide Calc	# Oxides	Oxides	Ox at%	Ox Wt%
C (Blanked)	4.956	9.045285	9045	FeS	1615	FeS	1.615	6.808
Si	14.883	11.61606	11616	FeO	0	FeO	0.000	0.00
Al (Blanked)	0.775	0.62977	630	Fe$_3$O$_4$	1811	Fe$_3$O$_4$	1.811	20.11
Fe	17.955	7.047776	7048	Leftover O	37975	SiO$_2$	11.61	33.467
Mg	12.012	10.83397	10834	SiO$_2$	11616	Al$_2$O$_3$	0.315	2.26
Ca	0.078	0.042548	43	Al$_2$O$_3$	315	MgO	10.83	20.938
Na	0.264	0.251701	252	MgO	10834	CaO	0.043	0.15
K	0.025	0.0142	14	CaO	43	Na$_2$O	0.126	0.374
S	2.362	1.614964	1615	Na$_2$O	126	K$_2$O	0.007	0.03
O	33.004	45.21879	45219	K$_2$O	7	CHNO	23.47	17.719
Total	86.315	86.31506	86315	Leftover O	2855	H$_2$O	1.824	1.576
				Leftover Atoms	13685	Total	--	103.43
				C	9045			
				H	13116			
				N	286			
				O	1031			
				Leftover O	1824			
				Leftover Atoms	283			
				H$_2$O	1824			
				H	3648			
				Leftover Atoms	−3365			

Table A.9: The summary of results of the wt% oxide calculation using the revised model (Table A.7).

#	Sample Name	SiO$_2$	Al$_2$O$_3$	FeS	FeO	Fe$_3$O$_4$	MgO	CaO	Na$_2$O	K$_2$O	CHNO	H$_2$O	TOTAL
16	CR3_b1_matrix	32.690	1.951	6.941	23.505	0.000	15.237	1.188	0.189	0.074	15.225	2.184	99.184
17	CR3_b1_matrix	34.500	1.999	7.586	24.171	0.000	15.751	1.287	0.230	0.075	13.258	2.581	101.438
18	CR3_b1_matrix2	31.498	2.289	7.393	25.799	0.000	15.705	1.097	0.160	0.061	12.149	2.674	98.826
19	CR3_b1_matrix4	31.078	2.071	6.940	25.442	0.000	14.036	1.140	0.193	0.068	13.407	2.423	96.796
20	CR3_b1_matrix3	29.962	2.115	7.161	27.942	0.000	14.177	0.936	0.159	0.068	15.029	2.257	99.805
21	CR3_b1_matrix5	31.513	2.983	6.514	25.180	0.000	16.690	1.659	0.174	0.076	11.535	2.554	98.877
22	CR3_b1_matrix6	32.268	1.894	5.586	18.979	0.000	23.266	1.933	0.143	0.056	15.691	1.808	101.624
23	CR3_b1_matrix7	31.777	1.960	7.269	22.323	0.000	17.857	0.985	0.140	0.061	16.749	2.048	101.171
24	CR3_b1_matrix8	31.034	2.102	8.215	22.247	0.000	15.845	1.298	0.150	0.079	14.738	2.518	98.226
25	CR3_b1_matrix9	30.876	2.500	8.569	24.545	0.000	14.213	1.406	0.162	0.070	13.999	2.690	99.028
26	CR3_b1_matrix10	31.455	2.136	7.763	24.408	0.000	13.626	1.109	0.188	0.096	16.150	2.247	99.178
27	CR3_b1_matrix11	32.472	1.833	7.557	22.095	0.000	16.773	1.897	0.213	0.089	14.699	2.386	100.012
28	CR3_b1_matrix12	38.206	2.582	4.135	17.709	0.000	14.520	8.327	0.428	0.048	14.088	1.700	101.743
29	CR3_b1_matrix13	30.939	1.807	8.473	23.644	0.000	15.110	0.605	0.202	0.098	18.099	2.156	101.132
30	CR3_b1_matrix14	30.202	2.719	6.172	25.269	0.000	12.581	3.073	0.282	0.105	15.239	2.019	97.661
31	CR3_b1_matrix15	31.127	2.093	8.318	20.047	0.000	17.005	1.471	0.172	0.069	19.473	1.926	101.702
32	CR3_b1_matrix16	31.344	1.973	8.444	24.213	0.000	15.425	1.696	0.129	0.068	14.030	2.654	99.975
33	CR3_b1_matrix17	32.150	1.911	5.726	21.100	0.000	19.212	0.976	0.105	0.053	15.996	1.802	99.030
34	CR3_b1_matrix18	30.346	2.511	7.401	21.946	0.000	14.214	2.901	0.144	0.061	15.185	2.268	96.978
35	CR3_b1_matrix19	32.614	2.018	7.109	21.543	0.000	16.881	0.689	0.117	0.068	15.060	2.230	98.329
36	CR3_b1_matrix20	30.295	2.216	10.492	20.654	0.000	17.000	0.641	0.108	0.042	19.290	2.414	103.152
37	CR3_b1_matrix21	32.158	1.992	8.464	21.995	0.000	15.974	1.143	0.150	0.083	19.335	1.977	103.270
38	CR3_b1_matrix22	33.860	2.180	7.110	20.230	0.000	18.828	0.993	0.166	0.061	17.158	1.959	102.545
39	CR3_b1_matrix23	32.411	2.034	7.335	20.842	0.000	15.970	1.245	0.161	0.060	19.034	1.768	100.859
40	CR3_b1_matrix24	29.615	2.097	7.900	21.251	0.000	14.061	2.206	0.198	0.069	23.885	1.270	102.552
41	CR3_b1_matrix25	29.848	1.901	8.400	24.147	0.000	14.432	1.236	0.210	0.065	16.816	2.302	99.357

Table A.9 (Continued): The summary of results of the wt% oxide calculation using the revised model ratios (Table A.7).

#	Sample Name	SiO$_2$	Al$_2$O$_3$	FeS	FeO	Fe$_3$O$_4$	MgO	CaO	Na$_2$O	K$_2$O	CHNO	H$_2$O	TOTAL
						OXIDE WEIGHT %							
76	CR2_matrix1	31.350	0.792	2.210	27.703	0.000	15.936	2.372	0.189	0.100	16.448	0.516	97.617
77	CR2_matrix2	30.250	1.312	4.858	28.733	0.000	12.890	1.525	0.268	0.116	19.197	0.676	99.823
78	CR2_matrix3	29.340	0.966	4.006	30.139	0.000	14.333	2.754	0.206	0.093	18.663	0.560	101.060
79	CR2_matrix4	30.477	1.186	3.068	28.191	0.000	15.283	2.730	0.208	0.082	18.156	0.431	99.813
80	CR2_matrix5	26.179	1.358	4.763	31.519	0.000	13.062	2.553	0.194	0.071	17.389	0.920	98.009
81	CR2_matrix6	31.017	1.323	3.713	28.696	0.000	14.489	2.250	0.234	0.101	16.101	0.903	98.828
82	CR2_matrix7	32.164	0.677	4.576	25.523	0.000	16.201	2.571	0.192	0.095	20.722	0.359	103.081
83	CR2_matrix8	29.157	1.035	4.340	27.314	0.000	13.736	2.525	0.209	0.087	21.751	0.145	100.299
84	CR2_matrix9	31.785	0.774	6.040	25.338	0.000	13.989	0.629	0.228	0.116	23.508	0.257	102.663
85	CR2_matrix10	31.184	0.945	4.108	29.680	0.000	13.221	1.423	0.217	0.110	17.487	0.777	99.155
91	CR2_matrix11	27.564	0.936	4.479	32.432	0.000	11.583	0.799	0.289	0.109	18.573	0.704	97.467
92	CR2_matrix12	24.899	1.254	7.569	26.364	0.000	13.723	2.975	0.246	0.086	24.326	0.444	101.885
93	CR2_matrix13	28.471	1.235	3.080	32.923	0.000	12.710	0.730	0.395	0.131	16.962	0.669	97.307
95	CR2_matrix14	25.188	0.742	4.683	38.890	0.000	10.196	0.661	0.342	0.110	17.908	0.869	99.589
96	CR2_matrix15	33.787	1.243	0.769	33.971	0.000	6.154	3.313	0.549	0.241	14.800	0.526	95.353
103	CR2_matrix17	29.222	1.184	2.121	33.664	0.000	11.403	0.917	0.341	0.129	17.630	0.345	96.957
105	CR2_matrix19	26.770	1.722	5.091	32.389	0.000	12.484	0.681	0.204	0.086	18.283	0.861	98.570
106	CR2_matrix20	25.273	1.654	5.904	30.787	0.000	12.416	0.910	0.218	0.076	23.883	0.157	101.278
107	CR2_matrix21	31.325	0.894	5.219	28.988	0.000	13.164	0.594	0.287	0.113	20.199	0.608	101.392
108	CR2_matrix22	32.835	0.797	6.012	26.180	0.000	13.651	0.519	0.251	0.148	20.434	0.741	101.568
109	CR2_matrix23	31.114	1.094	5.305	26.507	0.000	12.754	0.424	0.253	0.134	23.828	0.051	101.466
110	CR2_matrix24	30.648	1.254	6.522	26.561	0.000	12.569	0.421	0.297	0.124	22.321	0.557	101.274
111	CR2_matrix25	31.116	1.139	5.921	27.243	0.000	13.026	0.411	0.239	0.145	21.645	0.527	101.412
112	CR2_matrix26	31.104	0.993	5.759	26.172	0.000	14.098	0.540	0.271	0.128	23.888	0.143	103.096
113	CR2_matrix27	29.881	0.860	5.323	27.154	0.000	12.379	0.380	0.279	0.137	24.622	0.000	101.016
114	CR2_matrix28	31.586	1.111	4.874	28.494	0.000	12.457	0.313	0.241	0.138	17.237	0.995	97.444
115	CR2_matrix29	28.806	0.814	5.023	32.351	0.000	11.820	0.741	0.359	0.105	18.324	0.873	99.217
116	CR2_matrix30	30.951	1.267	5.579	23.538	0.000	19.407	2.086	0.199	0.089	19.166	0.819	103.101

Table A.9 (continued): the summary of results of the wt% oxide calculation using the revised model ratios (Table A.7).

|		OXIDE WEIGHT %											
#	Sample Name	SiO_2	Al_2O_3	FeS	FeO	Fe_3O_4	MgO	CaO	Na_2O	K_2O	CHNO	H_2O	TOTAL
42	CR1_matrix1	33.467	2.264	6.808	0.000	20.106	20.938	0.147	0.374	0.032	17.719	1.576	103.431
44	CR1_matrix3	33.638	3.025	6.341	0.000	20.114	21.133	0.398	0.425	0.039	14.930	1.618	101.661
46	CR1_matrix5	32.142	2.584	7.498	0.000	19.841	21.221	0.177	0.377	0.048	16.837	1.794	102.519
47	CR1_matrix6	30.804	2.874	5.793	0.000	23.551	20.078	0.205	0.340	0.037	14.065	1.257	99.003
48	CR1_matrix7	32.034	2.712	9.044	0.000	20.414	20.719	0.250	0.371	0.022	13.917	2.232	101.714
49	CR1_matrix8	33.200	2.690	4.609	0.000	20.566	22.248	0.597	0.346	0.031	13.649	1.258	99.195
50	CR1_matrix9	32.810	2.410	5.767	0.000	20.301	21.523	0.524	0.425	0.056	11.511	1.663	96.989
51	CR1_matrix10	32.580	2.462	6.870	0.000	19.516	21.633	0.271	0.410	0.030	16.834	1.687	102.292
52	CR1_matrix11	32.488	2.283	5.604	0.000	20.449	22.179	0.175	0.358	0.022	16.269	1.357	101.183
55	CR1_matrix14	32.309	2.408	6.940	0.000	19.212	21.541	0.201	0.381	0.039	19.084	1.607	103.721
58	CR1_matrix17	35.082	1.212	2.352	0.000	16.075	24.118	2.236	0.335	0.044	13.428	1.145	96.027
60	CR1_matrix19	33.055	2.675	4.736	0.000	19.032	22.525	1.059	0.393	0.034	13.242	1.438	98.187
61	CR1_matrix20	32.996	2.752	5.887	0.000	20.112	21.810	0.594	0.349	0.038	13.561	1.580	99.680
62	CR1_matrix21	32.725	1.462	9.212	0.000	16.682	23.698	0.984	0.349	0.043	16.418	2.443	104.015
64	CR1_matrix23	33.701	2.992	4.546	0.000	20.044	22.728	0.382	0.386	0.032	12.651	1.342	98.804
66	CR1_matrix25	31.408	2.324	5.227	0.000	23.964	19.151	0.116	0.407	0.045	15.313	1.053	99.008
67	CR1_matrix26	30.507	2.518	5.821	0.000	24.814	18.705	0.134	0.473	0.061	15.183	1.131	99.348
68	CR1_matrix27	31.868	2.518	5.201	0.000	24.256	19.412	0.168	0.397	0.046	13.161	1.129	98.155
69	CR1_matrix28	31.658	2.194	6.129	0.000	22.938	19.943	0.198	0.365	0.029	13.482	1.420	98.357
70	CR1_matrix29	32.209	2.442	5.562	0.000	23.527	20.053	0.125	0.426	0.038	18.988	0.970	104.340
71	CR1_matrix30	32.125	2.797	5.624	0.000	23.400	20.441	0.075	0.313	0.035	9.352	1.470	95.631
73	CR1_matrix32	32.117	3.026	5.743	0.000	22.998	19.571	0.265	0.393	0.039	12.665	1.369	98.185
74	CR1_matrix33	33.502	2.999	4.938	0.000	21.597	20.895	0.235	0.391	0.035	15.306	1.168	101.067
75	CR1_matrix34	32.965	3.350	5.405	0.000	22.597	20.001	0.100	0.360	0.028	13.402	1.280	99.488
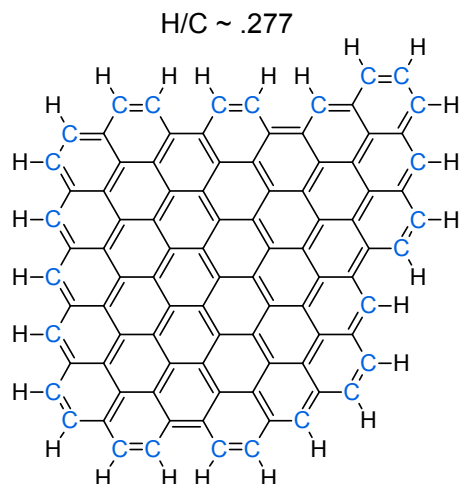
Figure A.15: An example of a defect-free PAH an atomic H/C ratio of ~ 0.277. The exterior carbons with bonded hydrogen atoms are highlighted in blue.

For QUE 99177 and EET 92161, the atomic H/C ratio is 0.275 and 0.135, respectively. In order to achieve these atomic H/C ratios in a molecule, there needs to be about 35 fused benzene rings for QUE 99177 and about twice as many for EET 92161. Let us assume for a moment that the GRO 95577 molecules are derived from EET 92161 and QUE 99177. We only need to break apart our large QUE 99177 molecule into smaller units of unsaturated hydrocarbons that are still large enough to produce an MMC signal in the Raman spectrum. Following that logic, if the EET 92161 MMC is the most primitive molecule, then QUE 99177 is derived from it by splitting the EET 92161 molecule in half.

We know from previous literature that the macromolecular materials in meteorites have other chemical groups, which is how the N and O atoms are incorporated into the structure (e.g., Peeters et al, 2012a). In order to incorporate these other groups into our hypothetical macromolecule, but preserve its atomic H/C ratio, we need to increase the number of internal carbons in the PAH group. Any group attached to the main PAH group will be less saturated than the PAH (any other organic group that is not another PAH will have an atomic H/C ratio ≥ 1), so interior carbons need to increase to compensate. Any carbon that gets replaced by an N or an O in a ring structure must also be replaced somewhere else. Similarly, if one adds defects to the PAH structure, which is expected since the Raman spectra detect strong D-bands, then the

148

number of interior carbon atoms decrease. To compensate, even more benzene rings must be added to the outside of the structure to keep the atomic H/C ratio below one. The resulting hypothetical molecule is shown in Figure 3.12 in the main text.

Bibliography

Abreu, N. M. (2007), Fine-scale mineralogical study of the matrices of CR carbonaceous chondrites: Insights on early solar system processes, Ph. D. Thesis, Univ. of New Mexico.

Abreu, N. M. and Brearley, A. J. (2004), Characterization of matrix in the EET 92042 and EET 92161 carbonaceous chondrite: insights into textural and mineralogical heterogeneity, 67th Annual Meeting of Meteoritical Society, abstract #5178.

Abreu, N. M., and A. J. Brearley (2010), Early solar system processes recorded in the matrices of two highly pristine CR3 carbonaceous chondrites, MET 00426 and QUE 99177, Geochimica et Cosmochimica Acta, 74(3), 1146–1171.

Abreu, N. M., Stanek, A. L., Bullock, E. S. (2012) Exotic Materials Found in Opaque Nodules in CR GRA 06100, 75th Annual Meeting of the Meteoritical Society, Abstract# 5266.

Aléon, J., F. Robert, M. Chaussidon, and B. Marty (2003), Nitrogen isotopic composition of macromolecular organic matter in interplanetary dust particles, Geochimica et Cosmochimica Acta, 67(19), 3773–3783.

Alexander, C. M. O.'D., S. S. Russell, J. W. Arden, R. D. Ash, M. Grady, and C. T. Pillinger (1998), The origin of chondritic macromolecular organic matter: A carbon and nitrogen isotope study, Meteoritics & Planetary Science, 33(4), 603–622.

Alexander, C. M. O.'D, M. Fogel, H. Yabuta, and G. D. Cody (2007), The origin and evolution of chondrites recorded in the elemental and isotopic compositions of their macromolecular organic matter, Geochimica et Cosmochimica Acta, 71(17), 4380–4403.

Alexander, C. M. O.'D., S. D. Newsome, M. L. Fogel, L. R. Nittler, H. Busemann, and G. D. Cody (2010), Deuterium enrichments in chondritic macromolecular material—Implications for the origin and evolution of organics, water and asteroids, Geochimica et Cosmochimica Acta, 74, 4417–4437.

Alexander, C. M. O.'D., R. Bowden, M. L. Fogel, and K. T. Howard (2013), Carbonate Abundances and Isotopic Compositions in Chondrites, 44th Lunar and Planetary Science Conference, Abstract# 2788.

Alexander, C. M. O.'D, K. T. Howard, R. Bowden, and M. L. Fogel (2013), The classification of CM and CR chondrites using bulk H, C and N abundances and isotopic compositions, Geochimica et Cosmochimica Acta, 123, 244–260.

Alexander, C. M. O.'D., G. D. Cody, Y. Kebukawa, R. Bowden, M. L. Fogel, A. L. D. Kilcoyne, L. R. Nittler, and C. D. K. Herd (2014), Elemental, isotopic, and structural changes in Tagish Lake insoluble organic matter produced by parent body processes, Meteoritics & Planetary Science, 49(4), 503–525.

Andrae, R. (2010), Error estimation in astronomy: A guide, eprint arXiv: 1009.2755.

Andrae, R., T. Schulze-Hartung, and P. Melchior (2010), Dos and Don'ts of reduced chi-squared, eprint arXiv: 1012.3754.

Aslan, B., and G. Zech (2005), New test for the multivariate two-sample problem based on the concept of minimum energy, Journal of Statistical Computation and Simulation, 75, 109–119.

Baker, J., M. Bizzarro, N. Wittig, J. Connelly, and H. Haack (2005), Early planetesimal melting from an age of 4.5662 Gyr for differentiated meteorites, Nature, 436(7054), 1127–1131.

Balsiger, H. and 49 coauthors (2007), Rosina – Rosetta Orbiter Spectrometer for Ion and Neutral Analysis, Space Science Reviews, 128(1–4), 745–801.

Beck, P., E. Quirico, G. Montes-Hernandez, L. Bonal, J. Bollard, F. R. Orthous-Daunay, K. T. Howard, B. Schmitt, O. Brissaud, F. Deschamps, B. Wunder, and S. Guillot (2010), Hydrous mineralogy of CM and CI chondrites from infrared spectroscopy and their relationship with low albedo asteroids, Geochimica et Cosmochimica Acta, 74, 4881–4892.

Bevington, P. R. and Robinson, D. K. Least-Squares Fit to an Arbitrary Function. In Data Reduction and Error Analysis for the Physical Sciences, Boston: WCB McGraw-Hill, 1992. 2nd ed. Chap. 8.

Beyssac, O., J.-N. Rouzaud, B. Goffé, F. Brunet, and C. Chopin (2002), Graphitization in a high-pressure, low-temperature metamorphic gradient: a Raman microspectroscopy and HRTEM study, Contributions to Mineralogy and Petrology, 143, 19–31.

Beyssac, O., L. Bollinger, J.-P. Avouac, and B. Goffé (2004), Thermal metamorphism in the lesser Himalaya of Nepal determined from Raman spectroscopy of carbonaceous material, Earth and Planetary Science Letters, 225, 233–241.

Biró, L. P., and P. Lambin (2013), Grain boundaries in graphene grown by chemical vapor deposition, New Journal of Physics, 15, 035024.

Bonal, L., E. Quirico, M. Bourot-Denise, and G. Montagnac (2006), Determination of the petrologic type of CV3 chondrites by Raman spectroscopy of included organic matter, Geochimica et Cosmochimica Acta, 70, 1849–1863.

Bonal, L., M. Bourot-Denise, E. Quirico, G. Montagnac, and E. Lewin (2007), Organic matter and metamorphic history of CO chondrites, Geochimica et Cosmochimica Acta, 71, 1605–1623.

Bonal, L., C. M. O. Alexander, G. R. Huss, K. Nagashima, E. Quirico, and P. Beck (2013), Hydrogen isotopic composition of the water in CR chondrites, Geochimica et Cosmochimica Acta, 106, 111–133.

Brearley, A. J. (2006), The Action of Water, in Meteorites and the Early Solar System II, edited by D. S. Lauretta and H. Y. McSween, pp. 584–624, University of Arizona Press, Tucson.

Busemann, H. (2006), Interstellar Chemistry Recorded in Organic Matter from Primitive Meteorites, Science, 312(5774), 727–730.

Busemann, H., C. M. O. Alexander, and L. R. Nittler (2007), Characterization of insoluble organic matter in primitive meteorites by microRaman spectroscopy, Meteoritics & Planetary Science, 42, 1387–1416.

Callahan, M. P., K. E. Smith, H. J. Cleaves, J. Ruzicka, J. C. Stern, D. P. Glavin, C. H. House, and J. P. Dworkin (2011), Carbonaceous meteorites contain a wide range of extraterrestrial nucleobases, Proceedings of the National Academy of Sciences, 108(34), 13995–13998.

Cançado, L., M. Pimenta, R. Saito, A. Jorio, L. Ladeira, A. Grueneis, A. Souza-Filho, G. Dresselhaus, and M. Dresselhaus (2002), Stokes and anti-Stokes double resonance Raman scattering in two-dimensional graphite, Physical Review B, 66(3).

Cançado, L. G., A. Jorio, E. H. M. Ferreira, F. Stavale, C. A. Achete, R. B. Capaz, M. V. O. Moutinho, A. Lombardo, T. S. Kulmala, and A. C. Ferrari (2011), Quantifying Defects in Graphene via Raman Spectroscopy at Different Excitation Energies, Nano Letters, 11, 3190–3196.

Casiraghi, C., S. Pisana, K. S. Novoselov, A. K. Geim, and A. C. Ferrari (2007), Raman fingerprint of charged impurities in graphene, Applied Physics Letters, 91, 233108.

Castiglioni, C., C. Mapelli, F. Negri, and G. Zerbi (2001), Origin of the D line in the Raman spectrum of graphite: A study based on Raman frequencies and intensities of polycyclic aromatic hydrocarbon molecules, The Journal of Chemical Physics, 114, 963.

Chakraborty, S., M. Ahmed, T. L. Jackson, and M. H. Thiemens (2008), Experimental Test of Self-Shielding in Vacuum Ultraviolet Photodissociation of CO, Science, 321(5894), 1328–1331.

Chakraborty, S., B. H. Muskatel, T. L. Jackson, M. Ahmed, R. D. Levine, and M. H. Thiemens (2014), Massive isotopic effect in vacuum UV photodissociation of N2 and implications for meteorite data, Proceedings of the National Academy of Sciences, 111(41), 14704–14709.

Chantler, C. T. (1995), Theoretical Form Factor, Attenuation and Scattering Tabulation for Z = 1–92 from E= 1–10 eV to E= 0.4–1.0 MeV, Journal of Physical and Chemical Reference Data, 24, 71–643.

Chantler, C. T., K. Olsen, J. Dragoset, A. R. Chang, S. A. Kilshore, S. A. Kotochigova, and D. S. Zucker (2005), X-ray form factor, attenuation and scattering tables (version 2.1), National Institute of Standards and Technology, Gaithersburg, MD (2005).

Charnley, S. B., and S. D. Rodgers (2002), The End of Interstellar Chemistry as the Origin of Nitrogen in Comets and Meteorites, The Astrophysical Journal, 569(2), L133–L137.

Charnley, S. B., and S. D. Rodgers (2008), Interstellar Reservoirs of Cometary Matter, Space Science Reviews, 138(1–4), 59–73.

Chernik, M. R. Bootstrap Methods: A Practitioner's Guide, Wiley Series in Probability and Statistics New York: Wiley, 1999.

Ciesla, F. J., and S. A. Sandford (2012), Organic Synthesis via Irradiation and Warming of Ice Grains in the solar nebula, Science, 336(6080), 452–454.

Cody, G. D., and C. M. O'D. Alexander (2005), NMR studies of chemical structural variation of insoluble organic matter from different carbonaceous chondrite groups, Geochimica et Cosmochimica Acta, 69(4), 1085–1097.

Cody, G. D., C. M. O.'D. Alexander, H. Yabuta, A. L. D. Kilcoyne, T. Araki, H. Ade, P. Dera, M. Fogel, B. Militzer, and B. O. Mysen (2008), Organic thermometry for chondritic parent bodies, Earth and Planetary Science Letters, 272, 446–455.

Cody, G. D., E. Heying, C. M. O.'D. Alexander, L. R. Nittler, A. L. D. Kilcoyne, S. A. Sandford, and R. M. Stroud (2011), Cosmochemistry Special Feature: Establishing a molecular relationship between chondritic and cometary organic solids, Proceedings of the National Academy of Sciences, 108, 19171–19176.

Connelly, J. N., M. Bizzarro, A. N. Krot, A. Nordlund, D. Wielandt, and M. A. Ivanova (2012), The Absolute Chronology and Thermal Processing of Solids in the Solar Protoplanetary Disk, Science, 338(6107), 651–655.

De Gregorio, B. T., R. M. Stroud, L. R. Nittler, C. M. O.'D. Alexander, N. D. Bassim, G. D. Cody, A. L. D. Kilcoyne, S. A. Sandford, S. N. Milam, M. Nuevo, and T. J. Zega, (2013), Isotopic and chemical variation of organic nanoglobules in primitive meteorites, Meteoritics & Planetary Science, 48(5), 904–928.

De Leuw, S., A. E. Rubin, and J. T. Wasson (2010), Carbonates in CM chondrites: Complex formational histories and comparison to carbonates in CI chondrites: Carbonates in CM chondrites, Meteoritics & Planetary Science, 45, 513–530.

Desch, S. J. (2007), Mass Distribution and Planet Formation in the solar nebula, The Astrophysical Journal, 671(1), 878–893.

Dietz, F., N. Tyutyulkov, G. Madjarova, and K. Müllen (2000), Is 2D Graphite an Ultimate Large Hydrocarbon? II. Structure and Energy Spectra of Polycyclic Aromatic Hydrocarbons with Defects, The Journal of Physical Chemistry B, 104, 1746–1761.

Downs, R.T. (2006) The RRUFF Project: an Integrated Study of the Chemistry, Crystallography, Raman and Infrared Spectroscopy of Minerals. 19th Meeting of the International Mineralogical Association.

Dresselhaus, M. S., G. Dresselhaus, R. Saito, and A. Jorio (2005), Raman spectroscopy of carbon nanotubes, Physics Reports, 409, 47–99.

Ehrenfreund, P., and S. B. Charnley (2000), Organic Molecules in the Interstellar Medium. Comets and Meteorites: A Voyage from Dark Clouds to the Early Earth, Annual Review of Astronomy and Astrophysics, 38, 427–483.

Eilers, P. H. C., and J. J. Goeman (2004), Enhancing scatterplots with smoothed densities, Bioinformatics, 20, 623–628.

El-Barbary, A., R. Telling, C. Ewels, M. Heggie, and P. Briddon (2003), Structure and energetics of the vacancy in graphite, Physical Review B, 68.

Elsila, J. E., S. B. Charnley, A. S. Burton, D. P. Glavin, and J. P. Dworkin (2012), Compound-specific carbon, nitrogen, and hydrogen isotopic ratios for amino acids in CM and CR chondrites and their use in evaluating potential formation pathways: Amino acid stable isotopes and formation pathways, Meteoritics & Planetary Science, 47(9), 1517–1536.

Emrich, K., D. H. Ehhalt, and J. C. Vogel (1970), Carbon isotope fractionation during the precipitation of calcium carbonate, Earth and Planetary Science Letters, 8(5), 363–371.

Ferrari, A., and J. Robertson (2000), Interpretation of Raman spectra of disordered and amorphous carbon, Physical Review B, 61, 14095–14107.

Ferry, J. M., T. Ushikubo, N. T. Kita, and J. W. Valley (2010), Assessment of grain-scale homogeneity and equilibration of carbon and oxygen isotope compositions of minerals in carbonate-bearing metamorphic rocks by ion microprobe, Geochimica et Cosmochimica Acta, 74(22), 6517–6540.

Floss, C., and F. Stadermann (2009), Auger Nanoprobe analysis of presolar ferromagnesian silicate grains from primitive CR chondrites QUE 99177 and MET 00426, Geochimica et Cosmochimica Acta, 73(8), 2415–2440.

Flynn, G., L. Keller, M. Feser, S. Wirick, and C. Jacobsen (2003), The origin of organic matter in the solar system: evidence from the interplanetary dust particles, Geochimica et Cosmochimica Acta, 67, 4791–4806.

Fries, M., M. Burchell, A. Kearsley, and A. Steele (2010), Capture effects in carbonaceous material: A Stardust analogue study, Meteoritics & Planetary Science, 44, 1465–1474.

Garvie, L. A. J., and P. R. Buseck (2007), Prebiotic carbon in clays from Orgueil and Ivuna (CI), and Tagish Lake (C2 ungrouped) meteorites, Meteoritics & Planetary Science, 42, 2111–2117.

Gasda, P.J., Misra, A.K, Sharma, S.K., and Taylor, G.J. (2011) Raman Microscopy: A Technique for Monitoring Pre-Biotic Reactions on Mineral Surfaces, Abstracts for the Origins 2011 International Conference, P6-35.

Gasda, P.J., Ogliore, R.C., and Taylor G.J. (2013), Addressing Background Fluorescence and Uncertainty Estimation in Raman Spectra of Insoluble Organic Carbon, 44th Lunar and Planetary Science Conference, Abstract# 1742.

Gasda, P.J. and Taylor, G.J. (2013), Effect of Aqueous Alteration on Insoluble Organic Carbon in CR Chondrites, 44th Lunar and Planetary Science Conference, Abstract# 1029.

Gasda, P. J. and Ogliore, R. S. (2014), Modeling the Raman Spectrum of Graphitic Material in Rock Samples with Fluorescence Backgrounds: Accuracy of Fitting and Uncertainty Estimation, Applied Spectroscopy, 68(12), 1393–1406.

Gasda, P. J., Hellebrand, E. and Taylor, G. J. (2014), Chemical properties of carbon materials in CR carbonaceous chondrites: the effects of aqueous alteration, Meteoritics and Planetary Science, submitted.

Glavin, D. P., M. P. Callahan, J. P. Dworkin, and J. E. Elsila (2011), The effects of parent body processes on amino acids in carbonaceous chondrites, Meteoritics & Planetary Science, 45(12), 1948–1972.

Goodyear, M. D., Gilmour, I., and Pearson, V. K. (2012), Chemical Modification of Organics in Meteorites as an aid to Easier Detection: Preliminary Results. 75th Meeting of the Meteoritical Society, Abstract# 5221.

Grossman, J. N. and R. Score (1996), The Meteoritical Bulletin, No. 79, 1996 July: Recently classified specimens in the United States Antarctic Meteorite Collection (1994–1996)*, Meteoritics & Planetary Science, 31, A161–A174.

Grossman, E. L. (2002), Stable carbon isotopes as indicators of microbial activity in aquifers, in Manual of Environmental Microbiology, edited by C. J. Hurst, pp. 728–742, American Society for Microbiology Press, Washington, D.C.

Harrison, T. M. (2009), The Hadean Crust: Evidence from >4 Ga Zircons, Annual Review of Earth and Planetary Sciences, 37(1), 479–505.

Hashimoto, A., K. Suenaga, A. Gloter, K. Urita, and S. Iijima (2004), Direct evidence for atomic defects in graphene layers, Nature, 430, 870–873.

Hazen, R. M., and D. A. Sverjensky (2010), Mineral Surfaces, Geochemical Complexities, and the Origins of Life, Cold Spring Harbor Perspectives in Biology, 2(5), a002162–a002162.

Holler, F., D. H. Burns, and J. B. Callis (1989), Direct Use of Second Derivatives in Curve-Fitting Procedures, Applied Spectroscopy, 43(5), 877–882.

Huss, G. R., B. S. Meyer, G. Srinivasan, J. N. Goswami, and S. Sahijpal (2009), Stellar sources of the short-lived radionuclides in the early solar system, Geochimica et Cosmochimica Acta, 73(17), 4922–4945.

Jewitt, D. C., H. E. Matthews, T. Owen, and R. Meier (1997), Measurements of 12C/13C, 14N/15N, and 32S/34S Ratios in Comet Hale-Bopp (C/1995 O1), Science, 278(5335), 90–93.

Jilly, C. E., G. R. Huss, and K. Nagashima (2013), Mn-Cr Dating of Secondary Carbonates in CR Chondrites, 44th Lunar and Planetary Science Conference, Abstract# 2474.

Jilly, C. E., G. R. Huss, K. Nagashima, and D. L. Schrader (2014), Oxygen Isotopes and Geothermometry of Secondary minerals in CR Chondrites, 77th Annual Meeting of the Meteoritical Society, Abstract# 5395.

Kawahara, F. K., B. Davila, S. R. Al-Abed, S. J. Vesper, J. C. Ireland, and S. Rock (1995), Polynuclear aromatic hydrocarbon (PAH) release from soil during treatment with Fenton's reagent, Chemosphere, 31, 4131–4142.

Kebukawa, Y., A. L. David Kilcoyne, and G. D. Cody (2013), Exploring the Potential Formation of Organic Solids in Chondrites and Comets through Polymerization of Interstellar Formaldehyde, The Astrophysical Journal, 771(1), 19.

Kerridge, J. F. (1999), Formation and Processing of Organics in the Early Solar System, Space Science Reviews, 90, 275–288.

Kotakoski, J., A. V. Krasheninnikov, U. Kaiser, and J. C. Meyer (2011), From Point Defects in Graphene to Two-Dimensional Amorphous Carbon, Physical Review Letters, 106.

Krot, A. N., H. Yurimoto, I. D. Hutcheon, and G. J. MacPherson (2005), Chronology of the early Solar System from chondrule-bearing calcium-aluminum-rich inclusions, Nature, 434(7036), 998–1001.

Krot, A. N., K. Keil, E. R. D. Scott, C. A. Goodrich, and M. K. Weisberg (2007), Classification of Meteorites, in Treatise on Geochemistry, pp. 1–52, Pergamon, Oxford.

Krot, A. N., Y. Amelin, P. Bland, F. J. Ciesla, J. Connelly, A. M. Davis, G. R. Huss, I. D. Hutcheon, K. Makide, K. Nagashima, L. E. Nyquist, S. S. Russell, E. R. D. Scott, K.

Thrane, H. Yurimoto, and Q.-Z. Yin. (2009), Origin and chronology of chondritic components: A review, Geochimica et Cosmochimica Acta, 73(17), 4963–4997.

Kudin, K. N., B. Ozbas, H. C. Schniepp, R. K. Prud'homme, I. A. Aksay, and R. Car (2008), Raman Spectra of Graphite Oxide and Functionalized Graphene Sheets, Nano Letters, 8, 36–41.

Kwok, S. (2004), The synthesis of organic and inorganic compounds in evolved stars, Nature, 430(7003), 985–991.

Kwok, S. (2009), Organic matter in space: from star dust to the Solar System, Astrophysics and Space Science, 319(1), 5–21.

Leitner, J., C. Vollmer, P. Hoppe, and J. Zipfel (2012), Characterization of presolar material in the CR chondrite Northwest Africa 852, The Astrophysical Journal, 745, 38.

Lesniak, P. M., and H. Sakai (1989), Carbon isotope fractionation between dissolved carbonate (CO_3^{2-}) and $CO_{2(g)}$ at 25° and 40°C, Earth and Planetary Science Letters, 95(3–4), 297–301.

Lucchese, M. M., F. Stavale, E. H. M. Ferreira, C. Vilani, M. V. O. Moutinho, R. B. Capaz, C. A. Achete, and A. Jorio (2010), Quantifying ion-induced defects and Raman relaxation length in graphene, Carbon, 48(5), 1592–1597.

Lundstedt, S., Y. Persson, and L. Öberg (2006), Transformation of PAHs during ethanol-Fenton treatment of an aged gasworks' soil, Chemosphere, 65, 1288–1294.

Lyons, J. R., and E. D. Young (2005), CO self-shielding as the origin of oxygen isotope anomalies in the early solar nebula, Nature, 435(7040), 317–320.

Lyons, J. R., E. A. Bergin, F. J. Ciesla, A. M. Davis, S. J. Desch, K. Hashizume, and J.-E. Lee (2009), Timescales for the evolution of oxygen isotope compositions in the solar nebula, Geochimica et Cosmochimica Acta, 73(17), 4998–5017.

Lyons, T. W., and C. T. Reinhard (2009), Early Earth: Oxygen for heavy-metal fans, Nature, 461(7261), 179–181.

Lyons, J. R., R. S. Lewis, and R. N. Clayton (2009), Comment on "Experimental Test of Self-Shielding in Vacuum Ultraviolet Photodissociation of CO," Science, 324(5934), 1516–1516.

Lyons, J. R. (2010), N_2 Self-Shielding in the Solar Nebula: an Update, 73rd Annual Meeting of the Meteoritical Society, Abstract# 5424.

Lyons, J. R., G. Stark, and A. Heays (2010), Assesment of CO Photodissociation Experiments by Model Simulations and Spectroscopic Measurements, 41st Lunar and Planetary Science Conference, Abstract# 2651.

Marty, B., L. Zimmermann, P. G. Burnard, R. Wieler, V. S. Heber, D. L. Burnett, R. C. Wiens, and P. Bochsler (2010), Nitrogen isotopes in the recent solar wind from the analysis of Genesis targets: Evidence for large scale isotope heterogeneity in the early solar system, Geochimica et Cosmochimica Acta, 74(1), 340–355.

McSween, H. Y., and S. M. Richardson (1977), The composition of carbonaceous chondrite matrix, Geochimica et Cosmochimica Acta, 41, 1145–1161.

Meibom, A., A. N. Krot, F. Robert, S. Mostefaoui, S. S. Russell, M. I. Petaev, and M. Gounelle (2007), Nitrogen and Carbon Isotopic Composition of the Sun Inferred from a High-Temperature solar nebular Condensate, The Astrophysical Journal, 656(1), L33–L36.

Messenger, S. (2000), Identification of molecular-cloud material in interplanetary dust particles, Nature, 404, 968–971.

Mojzsis, S. J., T. M. Harrison, and R. T. Pidgeon (2001), Oxygen-isotope evidence from ancient zircons for liquid water at the Earth's surface 4,300 Myr ago, Nature, 409, 178–181.

Mook, W. G., J. C. Bommerson, and W. H. Staverman (1974), Carbon isotope fractionation between dissolved bicarbonate and gaseous carbon dioxide, Earth and Planetary Science Letters, 22(2), 169–176.

Mumma, M. J., M. A. DiSanti, N. Dello Russo, K. Magee-Sauer, E. Gibb, and R. Novak (2003), Remote infrared observations of parent volatiles in comets: A window on the early solar system, Advances in Space Research, 31(12), 2563–2575.

Nakamura-Messenger, K., S. Messenger, L. P. Keller, S. J. Clemett, and M. E. Zolensky (2006), Organic Globules in the Tagish Lake Meteorite: Remnants of the Protosolar Disk, Science, 314, 1439–1442.

Neff, D., Bellot-Gurlet, L. Dillmann, P. Reguer, S. Legrand, L. (2006) Raman imaging of ancient rust scales on archaeological iron artefacts for long-term atmospheric corrosion mechanisms study, Journal of Raman Spectroscopy, 37, 1228–1237.

Nesbitt, H. W., and R. E. Wilson (1992), Recent chemical weathering of basalts, American Journal of Science, 292, 740–777.

Nguyen, A. N., L. R. Nittler, F. J. Stadermann, R. M. Stroud, and C. M. O. 'D. Alexander (2010), coordinated analyses of presolar grains in the Allan hills 77307 and Queen Elizabeth Range 99177 meteorites, The Astrophysical Journal, 719, 166–189.

Ogliore, R. C., G. R. Huss, and K. Nagashima (2011), Ratio estimation in SIMS analysis, Nuclear Instruments and Methods in Physics Research Section B: Beam Interactions with Materials and Atoms, 269(17), 1910–1918.

Owen, T., P. R. Mahaffy, H. B. Niemann, S. Atreya, and M. Wong (2001), Protosolar Nitrogen, The Astrophysical Journal, 553(1), L77–L79.

Pan, L., S. J. Desch, E. Scannapieco, and F. X. Timmes (2012), Mixing of Clumpy Supernova Ejecta into Molecular Clouds, The Astrophysical Journal, 756(1), 102.

Pearson, V. K., M. A. Sephton, A. T. Kearsley, P. A. Bland, I. A. Franchi, and I. Gilmour (2002), Clay mineral-organic matter relationships in the early solar system, Meteoritics and Planetary Science, 37, 1829–1833.

Pearson, V. K., A. T. Kearsley, M. A. Sephton, and I. Gilmour (2007), The labelling of meteoric organic material using osmium tetroxide vapor impregnation, Planetary and Space Science, 55, 1310–1318.

Peeters, Z., C. M. O. Alexander, H. Changela, L. R. Nittler, S. Price, and R. M. Stroud (2011), In situ Synchrotron X-Ray Transmission Microscopy of CR Chondrites QUE 99177 and GRA 95229, 74th Annual Meeting of the Meteoritical Society, Abstract# 5476.

Peeters, Z., Changela, H., Stroud, R. M., Alexander, C. M. O 'D., Nittler, L. R. (2012a) Coordinated analysis of in situ organic material in the CR chondrite QUE 99177, 43rd LPSC, Abstract# 2612.

Peeters, Z., H. Changela, R. M. Stroud, C. M. O'D. Alexander, and L. R. Nittler (2012b), Organic Carbon Inclusions in CR2 Chondrite Graves Nunataks 95229, 75th Annual Meeting of the Meteoritical Society, Abstract# 5283.

Pendleton, Y. J., and L. J. Allamandola (2002), The Organic Refractory Material in the Diffuse Interstellar Medium: Mid-Infrared Spectroscopic Constraints, The Astrophysical Journal Supplement Series, 138, 75–98.

Perronnet, M. and Zolensky, M. E. (2006) Characterization and quantification of metallic and mineral phases in the highly hydrated Grosvenor Mountains 95577 GRO 95577 chondrite, 37th Lunar and Planetary Science Conference, Abstract #2402.

Pimenta, M. A., G. Dresselhaus, M. S. Dresselhaus, L. G. Cançado, A. Jorio, and R. Saito (2007), Studying disorder in graphite-based systems by Raman spectroscopy, Physical Chemistry Chemical Physics, 9(11), 1276.

Quirico, E., P.-I. Raynal, and M. Bourot-Denise (2003), Metamorphic grade of organic matter in six unequilibrated ordinary chondrites, Meteoritics & Planetary Science, 38, 795–811.

Quirico, E., G. Montagnac, J.-N. Rouzaud, L. Bonal, M. Bourot-Denise, S. Duber, and B. Reynard (2009), Precursor and metamorphic condition effects on Raman spectra of poorly ordered carbonaceous matter in chondrites and coals, Earth and Planetary Science Letters, 287, 185–193.

Quirico, E., F.-R. Orthous-Daunay, P. Beck, L. Bonal, R. Brunetto, E. Dartois, T. Pino, G. Montagnac, J.-N. Rouzaud, C. Engrand, J. Duprat, (2014), Origin of insoluble organic matter in type 1 and 2 chondrites: New clues, new questions, Geochimica et Cosmochimica Acta, 136, 80–99.

Rampelotto, P. (2013), Extremophiles and Extreme Environments, Life, 3(3), 482–485.

Remusat, L., S. Derenne, and F. Robert (2005), New insight on aliphatic linkages in the macromolecular organic fraction of Orgueil and Murchison meteorites through ruthenium tetroxide oxidation, Geochimica et Cosmochimica Acta, 69(17), 4377–4386.

Romanek, C. S., E. L. Grossman, and J. W. Morse (1992), Carbon isotope fractionation in synthetic aragonite and calcite: effects of temperature and precipitation rate, Geochimica et Cosmochimica Acta, 56, 419–430.

Rothschild, L. J., and R. L. Mancinelli (2001), Life in extreme environments, Nature, 409(6823), 1092–1101.

Rotundi, A. and 19 coauthors (2008), Combined micro-Raman, micro-infrared, and field emission scanning electron microscope analyses of comet 81P/Wild 2 particles collected by Stardust, Meteoritics & Planetary Science, 43, 367–397.

Sandford, S. A., M. P. Bernstein, and J. P. Dworkin (2001), Assessment of the interstellar processes leading to deuterium enrichment in meteoritic organics, Meteoritics & Planetary Science, 36, 1117–1133.

Schmitt-Kopplin, P., Z. Gabelica, R. D. Gougeon, A. Fekete, B. Kanawati, M. Harir, I. Gebefuegi, G. Eckel, and N. Hertkorn (2010), High molecular diversity of extraterrestrial organic matter in Murchison meteorite revealed 40 years after its fall, Proceedings of the National Academy of Sciences, 107(7), 2763–2768.

Schulze, G., A. Jirasek, M. M. L. Yu, A. Lim, R. F. B. Turner, and M. W. Blades (2005), Investigation of Selected Baseline Removal Techniques as Candidates for Automated Implementation, Applied Spectroscopy, 59, 545–574.

Schulze, H. G., R. B. Foist, K. Okuda, A. Ivanov, and R. F. B. Turner (2012), A Small-Window Moving Average-Based Fully Automated Baseline Estimation Method for Raman Spectra, Applied Spectroscopy, 66(7), 757–764.

Sephton, M. A., and I. Gilmour (2001), Compound-specific isotope analysis of the organic constituents in carbonaceous chondrites, Mass Spectrometry Reviews, 20, 111–120,

Sephton, M. A. (2002), Organic compounds in carbonaceous meteorites, Natural Product Reports, 19(3), 292–311.

Sforna, M. C., M. A. van Zuilen, and P. Philippot (2014), Structural characterization by Raman hyperspectral mapping of organic carbon in the 3.46 billion-year-old Apex chert, Western Australia, Geochimica et Cosmochimica Acta, 124, 18–33.

Shah, S., B. E. Clark, T. Hiroi, and M. Zolensky (2004) Deconvolving terrestrial alteration mineral spectral signatures from meteorite reflectance measurements, 35th Lunar and Planetary Science Conference, Abstract #1012.

Shinohara, H., Y. Yamakita, and K. Ohno (1998), Raman spectra of polycyclic aromatic hydrocarbons. Comparison of calculated Raman intensity distributions with observed spectra for naphthalene, anthracene, pyrene, and perylene, Journal of Molecular Structure, 442, 221–234.

Si, Y. and E. T. Samulski (2008), Synthesis of Water Soluble Graphene, Nano Letters, 8, 1679–1682.

Starkey, N. A., I. A. Franchi, and C. M. O.'D Alexander (2013), A Raman spectroscopic study of organic matter in interplanetary dust particles and meteorites using multiple wavelength laser excitation, Meteoritics & Planetary Science, 48, 1800–1822.

Terrones, M., A. R. Botello-Méndez, J. Campos-Delgado, F. López-Urías, Y. I. Vega-Cantú, F. J. Rodríguez-Macías, A. L. Elías, E. Muñoz-Sandoval, A. G. Cano-Márquez, and J.-C. Charlier (2010), Graphene and graphite nanoribbons: Morphology, properties, synthesis, defects and applications, Nano Today, 5, 351–372.

Terzieva, R., and E. Herbst (2000), The possibility of nitrogen isotopic fractionation in interstellar clouds, Monthly Notices of the Royal Astronomical Society, 317(3), 563–568.

Tielens, A. G. G. M. (2005), The physics and chemistry of the interstellar medium, Cambridge University Press, Cambridge.

Tuinstra, F., and J. Koenig (1970), Raman Spectrum of Graphite, Journal of Chemical Physics, 53, 1126.

Visser, R., E. F. van Dishoeck, and J. H. Black (2009), The photodissociation and chemistry of CO isotopologues: applications to interstellar clouds and circumstellar disks, Astronomy and Astrophysics, 503(2), 323–343.

Vogel, J. C., P. M. Grootes, and W. G. Mook (1970), Isotopic fractionation between gaseous and dissolved carbon dioxide, Zeitschrift für Physik, 230(3), 225–238.

Wacey, D., M. R. Kilburn, M. Saunders, J. Cliff, and M. D. Brasier (2011), Microfossils of sulphur-metabolizing cells in 3.4-billion-year-old rocks of Western Australia, Nature Geoscience, 4(10), 698–702.

Walling, C. (1975), Fenton's reagent revisited, Accounts of Chemical Research, 8, 125–131.

Webster, C. R., P. R. Mahaffy, G. J. Flesch, P. B. Niles, J. H. Jones, L. A. Leshin, S. K. Atreya, J. C. Stern, L. E. Christensen, T. Owen, H. Franz, R. O. Pepin, A. Steele, and the MSL Science Team (2013), Isotope Ratios of H, C, and O in CO_2 and H_2O of the Martian Atmosphere, Science, 341(6143), 260–263.

Weisberg, M. K., M. Prinz, R. N. Clayton, and T. K. Mayeda (1993), The CR (Renazzo-type) carbonaceous chondrite group and its implications, Geochimica et Cosmochimica Acta, 57(7), 1567–1586.

Weisberg, M. K., M. Prinz, R. N. Clayton, T. K. Mayeda, M. M. Grady, and C. T. Pillinger (1995), The CR Chondrite Clan, Proceedings of the NIPR Symposium on Antarctic Meteorites, 8, 11–32.

Weisberg, K. K. and Prinz, M. (2000) The Grosvenor Mountains 95577 GRO 95577 chondrite and hydration of the CR chondrites, Meteoritics & Planetary Science, 35, Supplement, p.A168

Weisberg, M. K., and H. Huber (2007), The GRO 95577 CR1 chondrite and hydration of the CR parent body, Meteoritics & Planetary Science, 42(9), 1495–1503.

Wilde, S. A., J. W. Valley, W. H. Peck, and C. M. Graham (2001), Evidence from detrital zircons for the existence of continental crust and oceans on the Earth 4.4 Gyr ago, Nature, 409, 175–178.

Wilson, T. L., and R. T. Rood (1994), Abundances in the Interstellar Medium, Annual Review of Astronomy and Astrophysics, 32(1), 191–226.

Wopenka, B., and J. D. Pasteris (1993), Structural characterization of kerogens to granulite-facies graphite: Applicability of Raman microprobe spectroscopy, American Mineralogist, 78, 533–557.

Yang, J., J. I. Goldstein, and E. R. D. Scott (2008), Metallographic cooling rates and origin of IVA iron meteorites, Geochimica et Cosmochimica Acta, 72(12), 3043–3061.

Zhang, D., and D. Ben-Amotz (2000), Enhanced Chemical Classification of Raman Images in the Presence of Strong Fluorescence Interference, Applied Spectroscopy, 54(9), 1379–1383.

Zhang, J., P. D. Quay, and D. O. Wilbur (1995), Carbon isotope fractionation during gas-water exchange and dissolution of CO_2, Geochimica et Cosmochimica Acta, 59(1), 107–114.